UNIVERSIDADE FEDERAL DO CEARÁ
CENTRO DE TECNOLOGIA
DEPARTAMENTO DE ENGENHARIA METALÚRGICA E DE MATERIAIS
PROGRAMA DE PÓS-GRADUAÇÃO EM ENGENHARIA E CIÊNCIA DE MATERIAIS

DIMITRY BARBOSA PESSOA

NUMERICAL INVESTIGATION OF TEMPERATURE DISTRIBUTION OF AUTOGENOUS TIG WELDING PROCESS

FORTALEZA
2025

DIMITRY BARBOSA PESSOA

NUMERICAL INVESTIGATION OF TEMPERATURE DISTRIBUTION OF AUTOGENOUS TIG WELDING PROCESS

Tese apresentada ao Programa de Pós-Graduação em Ciência e Engenharia de Materiais da Universidade Federal do Ceará, como parte dos requisitos para obtenção do título de Doutor em Ciência e Engenharia de Materiais. Área de concentração: Processos de Transformação e Degradação de Materiais.

Orientador: Francisco Marcondes.

FORTALEZA
2025

Dados Internacionais de Catalogação na Publicação
Universidade Federal do Ceará
Sistema de Bibliotecas
Gerada automaticamente pelo módulo Catalog, mediante os dados fornecidos pelo(a) autor(a)

P567n Pessoa, Dimitry Barbosa.
Numerical investigation of temperature distribution of autogenous tig welding process / Dimitry Barbosa Pessoa. – 2025.
142 f. : il. color.

Tese (doutorado) – Universidade Federal do Ceará, Centro de Tecnologia, Programa de Pós-Graduação em Engenharia e Ciência de Materiais, Fortaleza, 2025.
Orientação: Prof. Dr. Francisco Marcondes.
Coorientação: Prof. Dr. Marcelo Ferreira Motta.

1. EbFVM. 2. 3D simulation. 3. Welding process. 4. Autogenous TIG. I. Título.

CDD 627

DIMITRY BARBOSA PESSOA

NUMERICAL INVESTIGATION OF TEMPERATURE DISTRIBUTION OF AUTOGENOUS TIG WELDING PROCESS

Thesis submitted to the Postgraduate Program in Materials Science and Engineering at the Federal University of Ceará as a partial requirement for obtaining the title of Doctor in Materials Science and Engineering. Concentration Area: Processes of Transformation and Degradation of Materials.

Approved in: March 17th,2025.

COMITEE MEMBERS

_____

Prof. Dr. Francisco Marcondes (supervisor)
Universidade Federal do Ceará (UFC)

_____

Prof. Dr. Marcelo Ferreira Motta (co-supervisor)
Universidade Federal do Ceará (UFC)

_____

Prof. Dr. Cleiton Carvalho Silva
Universidade Federal do Ceará (UFC)

_____

Prof. Dr. José Adilson de Castro
Universidade Federal Fluminense (UFF)

_____

Prof. Dr. Louriel Oliveira Vilarinho
Universidade Federal de Uberlândia (UFU)

To my mother, my father (in memory), my brothers,
my wife, Camylla Pessoa, and my children, Dimitry Filho, Esdras and Cecília.

ACKNOWLEDGEMENTS

Especially to God for his infinite kindness and mercy towards me. To my parents Antônio José Farias Pessoa (in memory) and Maria Margarida Barbosa Pessoa, for their love, education and encouragement.

To my supervisor Dr. Francisco Marcondes, for his patience, determination at all times and for his teachings, which were of great importance for the development of this work and for my academic life.

To my Co-supervisor Marcelo Ferreira Motta, for all his advice and precious moments of debate. To Professor Hélio de Miranda for the moments dedicated to discussing the practical part and valuable tips for carrying out the experiment.

To my wife Camylla Pessoa, thank you for the conversations that reassured me, for your attention, for your infallible advice, for the compliments that only come from those you love and, above all, for always caring about me.

I would like to thank my friends Izaac Andrade and Anderson Matos for their support and friendship when I needed it most, you helped me without sparing efforts. To my colleagues at LDFC, especially Ivens Lima who spared no effort to help me. To the Technology and Welding Research Laboratory (LPTS-UFC), for the support in carrying out the experiments.

I thank CAPES for the financial support for this research.

ABSTRACT

It is common to find welded steel structures in the industry, either in producing of parts or in cases that involve repairing them. There is several welding processes used to join metal parts and the study of these techniques is essential, both for choosing welding parameters, as well as for choosing the most appropriate method for each industrial application and the type of structure that will need repair by the welding process. This work focuses on studying the autogenous TIG welding process. The large thermal input in a welding process produces microstructural alterations and residual stresses that can harm the welded region. For this reason, the tireless search for the improvement of welding processes and the main effects caused to the material after the execution of the weld is justified. Understanding the temperature variation throughout the welded material can prevent failures from occurring. Experimental research processes are quite time consuming and costly. The use of numerical simulation steps is recurrent to assist in experimental welding processes for acquiring thermal cycles. Closed software such as ANSYS®, ABAQUS®, SYSWELD®, among others, are commonly used for numerical simulation stages of thermal cycle surveys. Numerical methods like; *difference finite (FDM), finite element (FEM), finite volume (FVM) and meshless Element-Free Galerkin (EFG*) are widely used to survey the welding thermal cycle. Although they are quite robust methods, they need to be complemented. Aiming to develop a simulator in the Fortran language aimed at numerical analysis of temperature distribution due to a welding process. This work uses the element-based finite volume method (EbFVM) as a mathematical pillar, together with structured and unstructured meshes. Four different heat sources; circular, semi-ellipse, semi-ellipsoid and double ellipsoid were used in this work as a numerical investigation target that best suited the autogenous TIG welding process. Parameters such as: electric current, voltage, welding speed, specific heat, thermal conductivity, welding efficiency and plate temperature are fundamental variables for the results to be compared with real experiments. A first test with data collected from the literature was performed to validate the numerical steps. After validating the results and checking the robustness of the code written in FORTRAN®, an experimental stage controlled in the laboratory was necessary. In the experimental stage, the steel used was AISI 409 with dimensions of 160mm x 50mm x 6.3mm. K-type thermocouples were used to acquire local thermal cycles. The thermocouples were fixed at points close to the fused region. Four weld

passes were performed on the steel piece with inter-pass temperature after the first weld pass. Still in the experimental stage, metallographic tests were carried out to measure the dimensions of the weld bead accurately and to be used in the heat sources of the numerical model. The results of the thermal cycles acquired in the experimental process for thermocouples fixed close to or within the thermally affected zone showed results in agreement with the numerical results when comparing the values of peak temperature, heating and cooling time and heating and cooling rate for the four welding passes. For thermal cycles acquired in regions farther from the thermally affected zone, the experimental and numerical results were concordant in the heating and cooling rates and in the heating and cooling time for the two values of electric current used.

Keywords: EbFVM; 3D simulation; welding process; autogenous TIG.

RESUMO

É comum encontrar estruturas de aço soldadas na indústria, seja na produção de peças ou em casos que envolvam reparos. Existem diversos processos de soldagem utilizados para unir peças metálicas e o estudo dessas técnicas é essencial, tanto para a escolha dos parâmetros de soldagem, quanto para a escolha do método mais adequado para cada aplicação industrial e o tipo de estrutura que necessitará de reparo pelo processo de soldagem. Este trabalho se concentra no estudo do processo de soldagem TIG autógena. O grande aporte térmico em um processo de soldagem produz alterações microestruturais e tensões residuais que podem prejudicar a região soldada. Por esse motivo, justifica-se a busca incansável pelo aprimoramento dos processos de soldagem e dos principais efeitos causados ao material após a execução da solda. Entender a variação de temperatura ao longo do material soldado pode prevenir a ocorrência de falhas. Processos de pesquisa experimental são bastante demorados e onerosos. O uso de etapas de simulação numérica é recorrente para auxiliar em processos de soldagem experimental para aquisição de ciclos térmicos. Softwares fechados como ANSYS®, ABAQUS®, SYSWELD®, entre outros, são comumente usados para estágios de simulação numérica de levantamentos de ciclo térmico. Métodos numéricos como; diferença finita (FDM), elemento finito (FEM), volume finito (FVM) e Galerkin sem malha (EFG) são amplamente usados para levantamento do ciclo térmico de soldagem. Embora sejam métodos bastante robustos, eles precisam ser complementados. Visando desenvolver um simulador na linguagem Fortran voltado para análise numérica da distribuição de temperatura devido a um processo de soldagem. Este trabalho usa o método de volume finito baseado em elementos (EbFVM) como um pilar matemático, juntamente com malhas estruturadas e não estruturadas. Quatro fontes de calor diferentes; circular, semi-elipse, semi-elipsoide e duplo elipsoide foram usadas neste trabalho como um alvo de investigação numérica que melhor se adequava ao processo de soldagem TIG autógena. Parâmetros como: corrente elétrica, tensão, velocidade de soldagem, calor específico, condutividade térmica, eficiência de soldagem e temperatura da chapa são variáveis fundamentais para que os resultados sejam comparados com experimentos reais. Um primeiro teste com dados coletados da literatura foi realizado para validar os passos numéricos. Após a validação dos resultados e verificação da robustez do código escrito em FORTRAN®, foi necessária uma etapa experimental controlada em laboratório. Na etapa experimental, o aço utilizado foi o AISI 409 com dimensões de 160mm x 50mm x 6,3mm. Termopares tipo K foram utilizados para aquisição de ciclos térmicos

locais. Os termopares foram fixados em pontos próximos à região fundida. Quatro passes de solda foram realizados na peça de aço com temperatura entre passes após o primeiro passe de solda. Ainda na etapa experimental, foram realizados ensaios metalográficos para mensurar com precisão as dimensões do cordão de solda e para serem utilizados nas fontes de calor do modelo numérico. Os resultados dos ciclos térmicos adquiridos no processo experimental para termopares fixados próximos ou dentro da zona termicamente afetada apresentaram resultados concordantes com os resultados numéricos ao comparar os valores de temperatura de pico, tempo de aquecimento e resfriamento e taxa de aquecimento e resfriamento para os quatro passes de soldagem. Para os ciclos térmicos adquiridos em regiões mais distantes da zona termicamente afetada, os resultados experimentais e numéricos foram concordantes nas taxas de aquecimento e resfriamento e no tempo de aquecimento e resfriamento para os dois valores de corrente elétrica utilizados.

Palavras-chave: EbFVM; simulação 3D; processo de soldagem; TIG autógeno.

LIST OF FIGURES

LIST OF TABLES

CONTENTS

1 INTRODUCTION

Fusion welding processes are characterized by the application of sufficient energy to generate heat and fuse the materials. The welding process is an economical and efficient method for joining metal parts, particularly in the construction, automotive, naval, energy, aerospace, mining, railway, oil and gas industries (1, 2, 3). Microstructural changes such as grain growth, phase transformations, distortion and residual stresses resulting from the welding thermal cycle, may occur, affecting the integrity of the weld and the properties of the material (4, 5). In recent times, welding processes have been developed through trial-and-error experiments, incorporating the knowledge and experience of engineers based on previous projects (2).

For this reason, we seek to improve welding processes and the main effects caused to the material after welding is carried out. In this understanding, numerical modeling has become an increasingly important ally in welding processes. Abrupt fluctuations in temperature and continuous phase change, which occur during welding, making it difficult to instrument and experimentally measure properties in a weld pool. This justifies the importance of the increasing use of computational models (3).

In this way, simulation algorithms generally based on the finite element method have become robustly useful and reliable for analyzing distortions and residual stresses produced by high temperature gradients in welding processes when the process is still in the early design stage (7). Commercial software is increasingly gaining strength in the use of simulations.

A more recent numerical modeling method is the EbFVM (Element based Finite Volume Method) which essentially is a finite volume method (FVM) that employs the concept of elements and shape functions FEM. Initially used to solve the Navier-Stokes equations with unstructured meshes, and later used in robust commercial software, the method is based on conservation at the level of discrete volumes created around the mesh nodes (8 - 12).

In this study, the welding process under investigation is Gas Tungsten Arc Welding (GTAW), commonly referred to as Tungsten Inert Gas (TIG) welding. This process is characterized by the use of a non-consumable tungsten electrode and an inert shielding gas, which protects the electrode, the electric arc, and the weld pool from atmospheric contamination. The welding condition adopted is autogenous, without the addition of filler material, a configuration frequently employed in applications demanding high precision and

superior metallurgical quality. GTAW stands out for producing welds with excellent surface finish, low defect rates, and minimal thermal distortion, making it particularly suitable for joining materials of high technological relevance, such as stainless steels, aluminum alloys, magnesium, copper, and nickel-based alloys. However, the process involves highly localized and transient heat input, steep thermal gradients, and complex thermo-mechanical interactions, which pose considerable challenges for computational modeling. These characteristics motivate the application of advanced numerical approaches such as the Element-based Finite Volume Method (EbFVM), which offers robust capabilities for accurately capturing the coupled thermo-mechanical behavior during welding (13-16). The use of EbFVM allows detailed prediction of temperature fields, which are of great importance for more detailed studies of residual stresses and distortions, providing a powerful tool for process optimization, distortion control and structural integrity assessment in welded components.

Microstructural changes associated with grain growth, phase changes, distortion and residual stresses produced by thermal cycling induced by the TIG process can affect the integrity of the welded region and the material properties (5). For this reason, the field of welding simulation research has grown year after year to control processing parameters in order to mitigate welding defects and their surrounding regions (18, 19, 1).

The use of thin sheets in the industries mentioned at the beginning of this work is recurrent. The reduced thickness sheet is the main variable for reducing mass in the structures of each industry. During the assembly of thin sheet metal structures, welding is one of the most commonly used joining methods in the assembly of thin sheet structures due to its design flexibility, high productivity and low cost (20). The welding process causes an intense temperature gradient and a non-uniform expansion and contraction, resulting in undesirable distortions and residual stresses.

This work aims to develop computational routines, written in FORTRAN, specifically designed to simulate the transient thermal behavior of thin metal sheets subjected to Gas Tungsten Arc Welding (GTAW) processes. The numerical formulation is based on the Element-Based Finite Volume Method (EbFVM), which combines the local conservation properties of finite volume methods with the geometric flexibility traditionally associated with finite element methods. The implemented routines incorporate different heat source models to represent the heat input with high fidelity, allowing a detailed analysis of the heat transfer phenomena inherent to welding processes. Compared to commercial finite element

packages, the EbFVM-based code offers significant advantages in terms of computational efficiency, local conservation of fluxes and greater adaptability to highly localized phenomena, such as steep thermal gradients typical of welding. Unlike conventional finite element methods (FEM), which are inherently variational, EbFVM imposes the integral form of the conservation laws on the volumes control systems constructed from the elements, improving the accuracy of heat flux predictions without sacrificing mesh flexibility. In contrast to traditional finite element methods (Cell-Centered Finite Volume Methods), predominantly used in fluid dynamics and often limited to structured or block meshes, EbFVM operates effectively on unstructured meshes, providing greater geometric adaptability for complex domains. The development of this routine provides a flexible and open framework for the implementation and testing of different physical models and boundary conditions, aspects often limited or inaccessible in commercial software. Prior to experimental validation, the code was rigorously tested and verified against reference cases and benchmark results available in the literature, ensuring its reliability and accuracy for thermal simulations in welding applications.

To strengthen the written code, an experimental step of autogenous TIG welding on thin sheets of AISI 409 stainless steel was carried out using two values of current. After the welding stage, a microstructural analysis of the weld bead region was carried out to identify the width, size of the fused zone and the heat-affected zone. Thermocouples were fixed in different regions of the plate and the peak temperature values; heating and cooling rates were in agreement when comparing the experimental results to the numerical results of thermocouples closer to the molten zone.

2 OBJECTIVES

2.1 General objectives

Develop numerical routines written in FORTRAN 90 that can simulate the thermal behavior of the autogenous TIG welding process on metal sheets from the EbFVM perspective, using various welding sources.

2.2 Specific objectives

- Experimentally to measure the welding thermal cycles, using k-type thermocouples at various positions on the AISI 409 ferritic stainless-steel sample to provide valuable data for calibrating the model.
- Validate the numerical simulator employing the EbFVM methodology by comparing the numerical results with those found in the literature, alongside a comparison with the experimental results.
- Exame the impact of the heat source model during the numerical simulation stage comparing it to experimental results.

2.3 Research motivation

Numerical simulations based on finite difference methods (22), finite elements (23), finite volumes (24) and free Galerkin elements (25) are vital tools for optimizing well-established welding processes. However, we acknowledge that these are not the only models capable of yielding reliable results when compared to experimental processes. We recognize that the element-based finite volume method (EbFVM), which is used to discretize the thermal energy equation to analyze a temperature distribution problem in steel plates capturing thermal cycles in various positions can bring relevant contributions to industry and research. From bibliographic research we are unaware that this method has been used for the autogenous TIG welding process on ferritic stainless-steel sheets. In this way, we hope that, based on robust and reliable results, this work can contribute to the welding field.

3 WELDING PROCESS

Arc welding processes are widely used to join metal parts. The electric arc in a welding process is an electrical discharge between two poles after the dielectric strength of the air has broken down. This discharge is maintained by gases released at the site of the discharge. The movement of this discharge results in a high temperature, which can melt the material.

Arc welding provides a union between parts after the solidification of the molten region (26). During this process, a certain region of the piece is subjected to very high temperatures. Heat distribution occurs very quickly due to the large temperature variation in a material with good thermal conductivity (1, 2, 3).

It is well known that residual stresses and metallurgical transformations due to thermal nonlinearities during welding processes can cause harmful effects (27). The most interesting regions in the analysis of heat transfer in the welding process are the fusion zone and the heat-affected zone, where high temperatures and high rates are reached (28).

3.1 Autogenous TIG Welding Process

The autogenous TIG welding process is based on creating and maintaining an electric arc between the non-consumable tungsten electrode and the workpiece. Some variables such as distance from the electrode to the workpiece, welding speed, electric current, torch inclination and gas flow, influence the GTAW process. Weld bead penetration is directly proportional to the electric current and inversely proportional to the welding speed. The greater the distance from the electrode to the workpiece, the greater the area of the base metal is heated, resulting in a wider bead, but with less penetration, due to a reduction in current density. When welding is carried out with a positive inclination in relation to the welding direction, see Fig. 1, the electric arc acts directly on the base metal, in front of the molten pool, increasing penetration.

Figure 1 – Welding Angles.

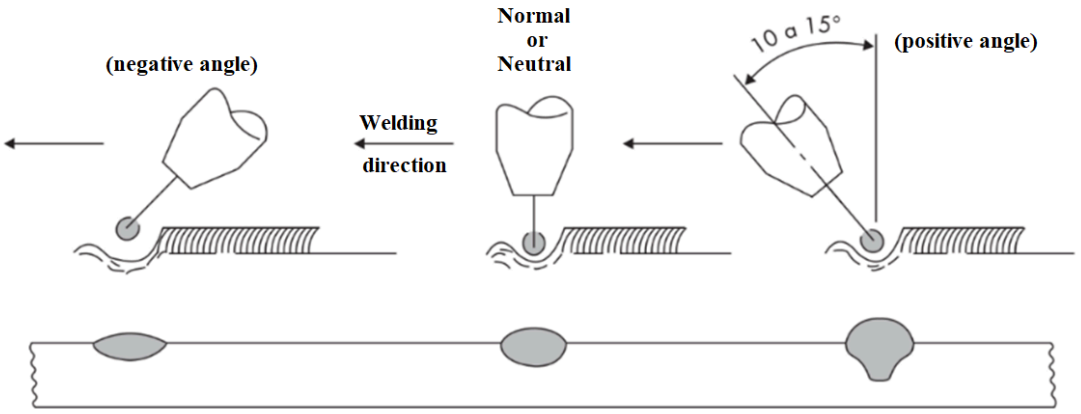

Source: (29) adapted.

3.1.2 Shielding gases

Inert gases, such as argon, helium or even a combination of these, are used as gases that shield the molten pool from contamination from the welding environment. These gases also have the function of stabilizing the electric arc. This process is generally used for all steels, stainless steels, cast iron, copper, brass, silver and titanium, nickel and aluminum alloys (30).

Table 1 lists some shielding gases used in the TIG welding process. Argon gas has some advantages over helium gas, such as: lower voltage drops, easier welding initiation and, as it is heavier, it offers more effective protection and greater resistance to cross current. These advantages, combined with the lower cost of argon, make it more attractive for TIG than helium (31).

Table 1 – Properties of shielding gases used in welding processes.

Gas	Chemical Symbol	Molecular weight (g/mol)	Density (g/L)	Ionization potential (eV)
Argon	Ar	39.95	1.784	15.7
Carbon dioxide	CO2	44.01	1.978	14.4
Helium	He	4.00	178	24.5
Hydrogen	H2	2.016	90	13.5
Nitrogen	N2	28.01	1.25	14.5
Oxigen	O2	32.00	1.43	13.2

Source: (29) aptaded.

3.1.3 Polarity

Fig. 2 shows three different polarities in GTAW indicating the movement of electrons at the time of welding (31).

Figure 2 – Three different polarities in the GTAW process.

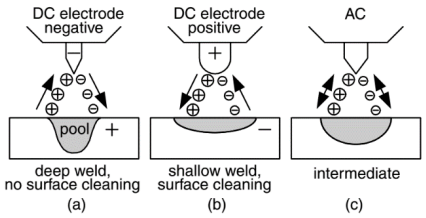

Source: (29, p. 14).

Direct Current Electrode Negative (DCEN): The tungsten electrode is connected to the negative terminal of the power source. Fig. 2(a) shows the movement of negative charges that are accelerated towards the base metal which during this process has positive polarity. The weld bead is narrower and has greater penetration power into the base metal.

Direct Current Positive Electrode (DCEP): The tungsten electrode is connected to the positive terminal of the power source. Fig. 2(b) shows the movement of positive charges that are accelerated towards the base metal which during this process has negative polarity. As the electrons move towards the electrode, there will be greater wear on the tip of the electrode, as it will heat up more. See in Fig. 2(b) that the tip of the electrode is more rounded (greater wear).

Alternating current (AC): The tungsten electrode is connected to the source terminal which has polarity oscillation during the welding process alternating between positive and negative, as shown in Fig. 2(c). In this condition there is less wear on the electrode tip and greater penetration of the molten region when compared to DCEP.

For the experimental autogenous TIG welding process of this work, the polarity of the source used was negative.

3.1.4 Electrode

Tungsten electrodes with 2% cerium or thorium have better electron emissivity current carrying capacity and contamination resistance than pure tungsten electrodes (33). The ability of the electrode to emit electrons is called electronic emissivity, which, if low, implies a higher temperature at the electrode tip required to emit electrons and, therefore, a greater risk of melting the tip (31).

4 ANALYTICAL SOLUTION OR GENERAL SOLUTION OF ROSENTHAL

According to the law of conservation of energy, the partial differential equation of heat flow for the moving heat source can be written as (40):

$$\frac{\partial}{\partial t}\left(\rho(T)c_p(T)T\right) = \nabla \bullet (k\nabla T) + \dot{q} \tag{1}$$

where T temperature, k the isotropic thermal conductivity constant, $\rho(T)$ and $c(T)$ represent the density and specific heat of the material, respectively, both dependent on temperature and $\dot{q}$ represent the rate of heat transfer from a welding arc. The Eq. 1 determines the temporal variation of enthalpy, where $\nabla \bullet (k\nabla T)$ the rate at which heat is lost by conduction.

For a heat source moving along the y-axis according to Eq. 2, and the physical properties and temperature distribution around the source assumed to be constant, Eq. 1 can be rewritten in a quasi-steady state as Eq. 3 (34).

$$\xi = y - vt \tag{2}$$

$$\frac{\rho c}{k}\left(\frac{\partial T}{\partial \xi}\right) = (\nabla^2 T) + \frac{\dot{q}}{k} \tag{3}$$

Fig. 3 shows the direction and sense of torch movement in a rectangular geometry that exemplifies a steel sample of thickness d, with a weld bead being made in the center. The direction of movement of the torch is the y-axis.

Figure 3 – Defining the Coordinate System of a Point Source in a 3D Geometry.

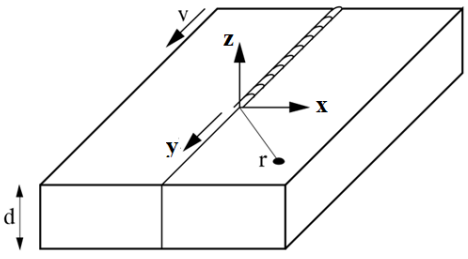

Source: (31, p. 210).

Fig. 4 shows the schematic direction of heat flow in a welding process. The arrows in Fig. 4a indicate a semicircular flow direction and Fig. 4b a longitudinal flow direction.

Figure 4 – Schematic heat flow in the welding process of “thick” (a) and “thin” (b) materials

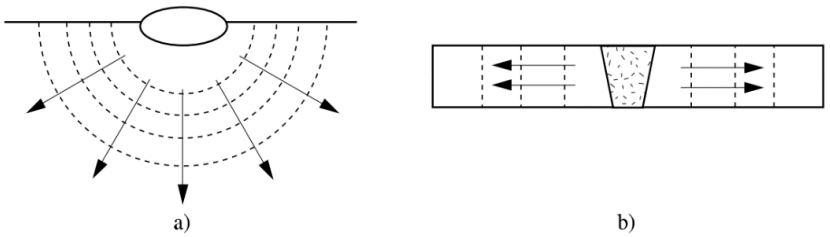

Source: (35, p. 91).

According to Rosenthal's assumptions (34) and the solution of the Helmholtz equation, the general solution based on a series of simplifications considering constant material properties, finite orthogonal domain, quasi-steady state regime (temperature redistribution around the source adopts a stable form with respect to time), neglecting thermal losses due to phase change, convection and radiation will be (34, 35):

$$T = T_0 + \frac{P}{2\pi kR} e^{\left[-\frac{v}{2\alpha}(y+R)\right]} \quad (4)$$

where T_0 initial temperature, P= ηVI the net power provided by welding, V is the arc voltage, I welding current, η process efficiency, k thermal conductivity of the material, $R = \sqrt{x^2 + \xi^2 + z^2}$ distance from the center of the source to neighboring points, v welding velocity and $\alpha = \frac{k}{\rho c}$ is the thermal diffusion term.

Fig. 5 shows the temperature distribution based on the model in Eq. 4. In Fig. 5a isothermal lines are formed parallel to the xy plane indicating that the further away from the plane, the higher the temperature value and consequently the smaller the region enclosed by the isotherm with the vertical thinning in Fig. 5a and the thinning around the dotted line in Fig. 5b. Fig. (5c) shows the isothermal distribution for steady-state regime.

Figure 5 – Temperature distribution based on the equation 4 model.

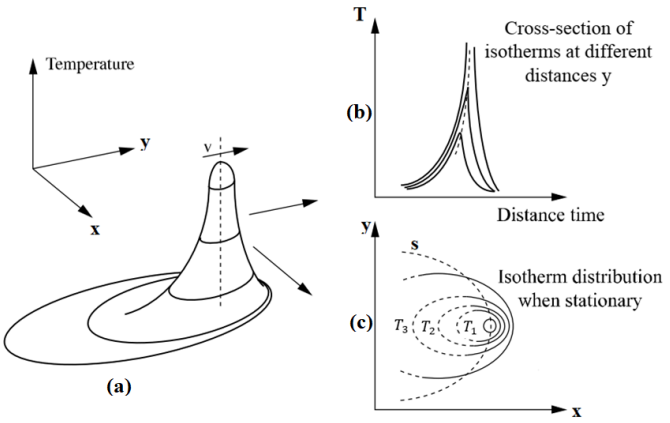

Source: (31, p. 93).

The first work on the exact solution of heat transfer and temperature distribution induced by a moving heat source can probably be attributed to Rosenthal and Cameron in 1938 (36), which was expanded by Rosenthal eight years later (1946) (34).

5 WELDING THERMAL CYCLE

The welding thermal cycle describes the variation in temperature at a point located on a steel sample that undergoes a welding process. The location of the thermal cycle evaluation point is fundamental to describe the temperature variation as a function of time. In practical terms, the acquisition of thermal cycles can be carried out using thermocouples (type K – Chromel and Alumel) fixed to the base metal by means of a capacitive discharge. The main parameters that describe the thermal cycle are:

Peak temperature: It is the local maximum temperature. It indicates the possibility of local transformations in the microstructure occurring. The maximum local temperature point of a welding process depends on the initial temperature of the part, the thermophysical properties of the material, the heat input of the welding source and the geometry of the part. The peak temperature as a function of distance from the weld axis is given by:

$$T_p = T_0 + \frac{E}{2\pi kt} e^{\frac{-R^2}{4\alpha t}} \quad (5)$$

The peak temperature was one of the variables used in this work as a comparison between the experimental and numerical process.

Their local distribution as a function of time is shown in Fig. 6.

Figure 6 – Local thermal cycle.

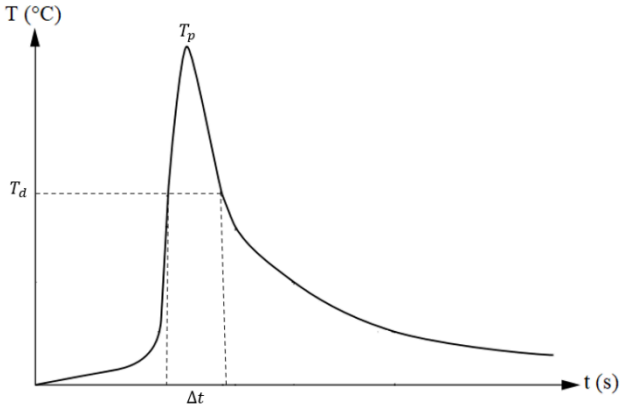

Source: (35), adapted.

The peak temperature may vary if the local temperature acquisition point is distant from the weld bead, as shown in Fig. 7. Thermocouples closer to the molten zone have higher peak temperature values than thermocouples further from the molten zone.

Figure 7 – Thermal cycle of distant points perpendicular to the weld bead.

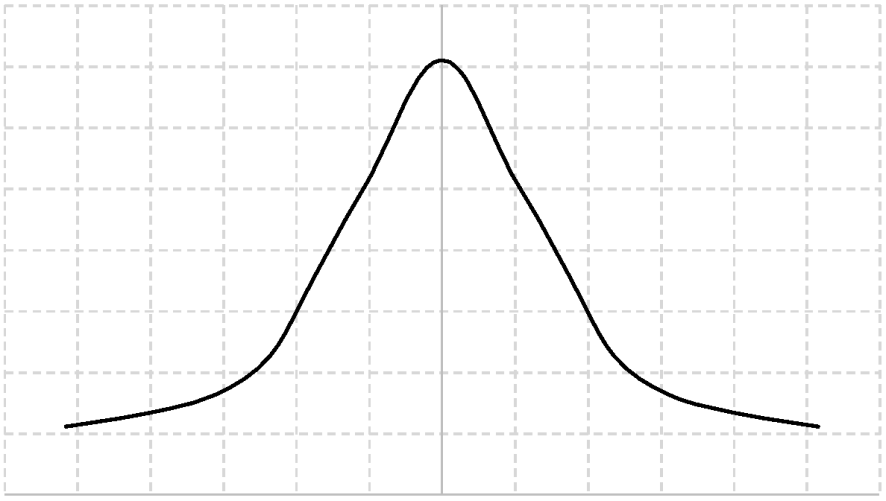

Source: The author (2025).

Deriving Eq. 5 with respect to time we have that

$$\frac{dT}{dt} = \frac{\Delta T}{t}\left(\frac{R^2}{4\alpha t} - 1\right) \tag{2}$$

From Eq. 6, the possibility for the maximum temperature to occur is for dT/dt=0, thus we have

$$t = \frac{R^2}{4\alpha} \tag{5}$$

where t is the time source passed through the temperature measurement location on the part.

Substituting Eq. 7 into Eq. 5, we have

$$T_p = \frac{2E}{\pi e \rho c r_p^{\ 2}} \tag{8}$$

Eq. 8 is not mathematically exact and presents temperatures that are excessively high in relation to those empirically obtained (37). Therefore, for a point of known maximum temperature, we obtain

$$\Delta T_p = \frac{2E\left(T_c - T_0\right)}{\pi\rho ec\left(T_c - T_0\right)\left(r_p^2 - r_c^2\right) + 2E} \quad (9)$$

where r_c the distance from the center of the weld bead to the location of the maximum known temperature T_c.

Dwell temperature $\left(T_d\right)$**:** The time interval that the temperature acquisition point remains above a temperature. The dwell temperature is considered to be that which indicates a change in the microstructure of the base metal, that is, the heat-affected zone. At this temperature, significant changes in properties of the base metal can occur. For this work, the dwell temperature value used as a comparative analysis between the experimental and simulated results was 500°C.

Cooling rate: An important variable, some common structural steels can undergo phase transformations during cooling. The cooling rate for a temperature is obtained by the derivative of the function that describes the cooling with respect to time, being a negative scalar quantity. In this work, the cooling rate between the experimental and numerical processes was compared and used as a parameter to affirm that the code developed in FORTRAN under the EbFVM methodology reproduces results similar to the experimental one.

Deriving Eq. 4 with respect to time, we obtain

$$-\frac{dT}{dt} = \left(\frac{vy}{R^2} + \frac{yv^2}{2\alpha R} + \frac{v^2}{2\alpha}\right)\Delta T \quad (10)$$

where $\Delta T = \left(T_c - T_0\right)$ and T_c is the critical temperature, or the one for which you want to calculate the cooling rate.

In a welding process where the weld bead is deposited on the surface of the solid, heat loss will occur in all directions as shown in Figs. 4 and 5. The construction of the weld bead is given by an energy source with point and mobile geometry that was designed by Rosenthal (34), as shown in Fig. 3.

For energies deposited on the surface of a plate, we have Eq. 4. For points located on the weld metal immediately behind the heat source, and taking into account the moving torch, according to Eq. 2 with |y|=R we have;

$$\Delta T = \frac{P}{2k\pi|y|} \quad (11)$$

The maximum cooling rate occurs in the weld metal for |y|=R. Deriving Eq. 11 as a function of y, we have

$$\frac{dT}{dy} = -\frac{P}{2k\pi y^2} \quad (12)$$

Substituting Eq. 11 into Eq. 12, we have that

$$\frac{dT}{dy} = \frac{-(T_c - T_0)}{y} \quad (13)$$

The cooling rate can be written as $\frac{dT}{dt} = \frac{dT}{dy}\frac{dy}{dt}$. Therefore,

$$\frac{dT}{dy} = \frac{-2\pi k}{E}(T_c - T_0)^2 \quad (14)$$

Eq. 14 is valid when the critical temperature is close to the melting point of the metal. Eq. 14 can be used for the heat-affected zone immediately adjacent to the weld bead when the critical temperature is up to about half the melting temperature of the metal (38).

The cooling rate calculated in each thermocouple of this work was calculated by taking the derivative of the temperature as a function of time. The results obtained by the experimental and numerical process were compared and showed good agreement.

5.1 Points of maximum heating and cooling rate

Deriving Eq. 5 as a function of time, we have

$$\frac{dT}{dt} = \frac{E}{2\pi k}\left(\frac{R^2}{4\alpha t^3} - \frac{1}{t^2}\right)e^{-\frac{R^2}{4\alpha t}} \quad (15)$$

Fig. 8 illustrates the rate of temperature variation with respect to time. To construct the graph it was assumed that, $\frac{E}{2\pi k} = 1$ and $\frac{R^2}{4\alpha} = 1$, in Eq. 5 and Eq. 15.

Figure 8 – Thermal cycle and cooling rate.

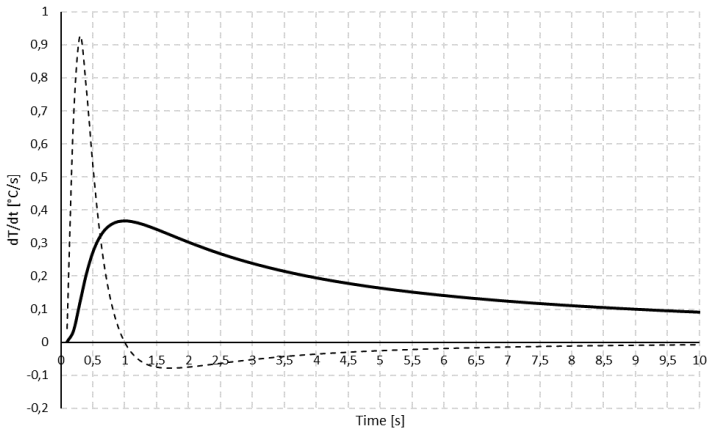

Source: The author (2025).

Fig. 8 shows that heating occurs in the first 0.9 s and the maximum rate is 0.9248 °C/s at t = 0.3 s with a local temperature of 0.1189 °C. The maximum cooling rate is -0.07912 °C/s at t = 1.7 s with a local temperature of 0.3266 °C. The peak temperature value is 0.3678 °C.

With the reduction of the temperature gradient as a function of time, the rate of change after 6s tends to zero.

6 MATHEMATICAL MODEL

According to the principle of conservation of energy, the aggregate temperature distribution with phase change during the welding process can be described by the following Eq. 1 (39, 40) in the domain Ω composed of the domains Ω_s (solid) Ω_{sl} (solid + liquid) e Ω_l (liquid).

$$\rho(T)\frac{\partial}{\partial t}H(T) = \vec{\nabla} \bullet \left(\bar{k}(T) \bullet \vec{\nabla}T\right) + \dot{q} + \dot{q}_s \tag{16}$$

where T temperature, t time and $\dot{q}$ the term source and $\dot{q}_s$ the term for energy loss by convection and radiation. Physical properties: enthalpy $H(T)$, second-order isotropic thermal conductivity tensor $\bar{k}(T)$ and density $\rho(T)$ are considered temperature dependent. In this work we will not assume the advective term (41). The source term can be written as,

$$\dot{q} = \dot{q}_f(r,t) \tag{5}$$

$\dot{q}_f(r,t)$ represents the volumetric heat input generated by the welding arc, which will be described in detail in Chapter 7. The enthalpy term $H(T)$ takes into account the phase change resulting from heating or cooling the sample and can be given by

$$H = \int_{T_0}^{T} c(T)dT + f_L(T).L \tag{18}$$

where L is the latent heat and f_L represents the liquid fraction reasonably given by a linear variation with the temperature within the liquid region that can be given by (42);

$$f_L = \{0, \quad T \leq T_{sol} \quad \epsilon \quad \Omega_s \; \frac{T - T_{sol}}{T_{liq} - T_{sol}}, \quad T_{sol} \leq T \leq T_{liq} \quad \epsilon \quad \Omega_{sl} \; 1, \tag{19}$$

The term T_{sol} represents the temperature of solid and T_{liq} the liquid temperature in order to take into account a wide range of phase change. For the condition moments before the source's action, the body is considered to be at room temperature.

Eq. 18 can be written as

$$H = \{c(T).T \;\; para \;\; T \leq T_{sol} \quad \epsilon \quad \Omega_s \; c(T).T + \frac{T - T_{sol}}{T_{liq} - T_{sol}} L \;\; para \tag{20}$$

Substituting Eq. 18 and 20 into Eq. 16, we have

$$\rho(T)\frac{\partial}{\partial t}H(T) = \vec{\nabla} \bullet \left(\bar{k}(T).\vec{\nabla}T\right) + \dot{q}(r,t) - \rho(T)L\frac{\partial f_L}{\partial T}\frac{\partial T}{\partial t} \tag{21}$$

Eq. 21 can easily be written as

$$\rho(T)\left(\frac{\partial}{\partial t}H(T) + L\frac{\partial f_L}{\partial T}\frac{\partial T}{\partial t}\right) = \vec{\nabla} \bullet \left(\bar{k}\vec{\nabla}T\right) + \dot{q}(r,t) \tag{22}$$

6.1 Heat Transfer Mechanism

Heat transfer occurs naturally due to the temperature difference between two points in a system. Transfer processes are classified as conduction, convection, and radiation. A temperature distribution in a thermodynamic system is characterized by a combination of these modes of thermal energy transfer. Thermal energy transfer processes, although they generally occur in a combined and simultaneous manner, the analysis of heat transfer will place greater emphasis on the predominant process in that thermodynamic system.

6.1.1 Conduction Heat Transfer

The conduction process is given in a conducting or non-conducting solid system. Transport in non-conductive media is carried out by vibrational waves and in conductive media by translational movement of free electrons. Conduction also occurs in static fluids

through the direct movement of molecules. The conduction of thermal energy was founded in 1822 by Joseph Fourier. The constitutive equation of Fourier's nonlinear isotropic heat flux is given by Eq. 23 (43)

$$q'' = \; - \; k.\nabla T \tag{23}$$

k represents the conductivity tensor and T represents the scalar temperature field.

6.1.2 Radiation Heat Transfer

The process of heat propagation by radiation occurs through the emission and absorption of electromagnetic waves or photons, as a result of variation in the electronic configurations of atoms or molecules. It is the only process that does not need a material medium to occur and is more efficient in environments with a smaller amount of matter.

For opaque solids, such as metals, radiation is generally considered a surface phenomenon, since radiation emitted by the interior regions of these materials never reaches the surface, and radiation incident on such bodies is absorbed in a layer up to a few microns from the surface. If a surface is assumed to have an emissivity coefficient ε, the net rate of heat transfer by radiation that the surface emits can be expressed per unit area as (43):

$$q''_{rad} = \; \sigma\varepsilon\left(T^4 - \; T_0{}^4\right) \tag{24}$$

q''_{rad} is the heat flux emitted (W/m²), σ and ε are respectively the Stefan-Boltzmann constant and emissivity of the material. Eq. 27 can be seen as the Eq. 25

$$q''_{rad} = \; h_{rad}\left(T \; - \; T_0\right) \tag{25}$$

h_{rad} is the temperature-dependent heat coefficient resulting from radiation.

6.1.3 Convection Heat Transfer

Convection is the mechanism of thermal energy transfer between a solid surface and the liquid or gas in motion adjacent to the surface. This type of transfer involves the combined effects of conduction and fluid motion. The greatest heat transfer by convection occurs at the moment of the faster fluid intensity. The transfer between the solid surface and the adjacent fluid is by pure conduction, in the absence of macroscopic fluid motion. For any macroscopic fluid motion, the heat transfer between the solid surface and the fluid increases, but it also complicates the determination of heat transfer rates.

Eq. 26 describes heat transfer by convection regardless of its type (43).

$$q''_{conv} = h.\left(T_s - T_\infty\right) \tag{26}$$

q''_{conv} the flow of heat by convection (W/m²), h is the convection heat transfer coefficient, T_s is the surface temperature and T_∞ is the average temperature of the fluid.

7 EQUATIONS THAT DESCRIBES THE GEOMETRIC AND THERMAL BEHAVIOR OF THE ENERGY SOURCE

In general, the electric arc is modeled in two ways: by prescribing the temperature at the weld or by specifying a heat distribution prescription. When using the technique of prescribing temperature using the finite element method, which is the most widely used method, the temperature is established at nodes within a region. In heat distribution, the most commonly used method is a Gaussian distribution. For this work, a Gaussian heat distribution was used at each vertex of the control subvolume element. Four heat source models will be analyzed: the double ellipsoid model (W/m³) (Goldak Model) (34, 44), the semi-ellipsoid model (W/m³) (45) and two flat sources (W/m²), which are the circular model (46) and double ellipse model (47).

Four weld passes will be performed with an interval controlled by an inter-pass temperature of 250°C. The time the source operates at the melting temperature will be given by the entire length of the welding bead. The movement of the source is given by repeating the distribution of the heat flux, node after node, to simulate the movement of the source.

7.1 Double Ellipsoid Model

The double ellipsoid heat source is composed of a quarter of an ellipsoid in the front region and a quarter of an ellipsoid in the back region, as shown in Fig. 9The parameters **a** and **b** are the semiaxes of the ellipsoid. Furthermore, c_1 and c_2 address the axis segments on the front and rear ellipsoids, respectively.

Figure 9 – Goldak's double ellipsoid (34).

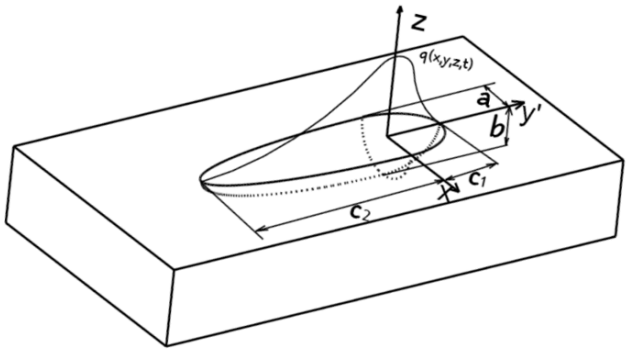

Source: (46, p. 32).

The function representing the source shown in Fig. 9 is formed by Eq. 27 for the front side

$$Q_1(x,\xi,z,t) = \frac{6\sqrt{3}.f_1.U}{a.b.c_1.\pi^{\frac{3}{2}}} e^{\left[-3\frac{(x-x_0)^2}{a^2}-3\frac{(\xi)^2}{c_1^2}-3\frac{(z-z_0)^2}{b^2}\right]} if\ \{\xi \geq 0\ \frac{x^2}{a^2} + \frac{\xi^2}{c_1^2} + \frac{z^2}{b^2}$$

$$Q_1(x,\xi,z,t) = 0\ if\ \{\xi \geq 0\ \frac{x^2}{a^2} + \frac{y^2}{c_1^2} + \frac{\xi^2}{b^2} > 1 \quad (27)$$

and Eq. 28 for the rear.

$$Q_2(x,\xi,z,t) = \frac{6\sqrt{3}.f_2.U}{a.b.c_2.\pi^{\frac{3}{2}}} e^{\left[-3\frac{(x-x_0)^2}{a^2}-3\frac{(\xi)^2}{c_2^2}-3\frac{(z-z_0)^2}{b^2}\right]} if\ \{\xi < 0\ \frac{x^2}{a^2} + \frac{\xi^2}{c_2^2} + \cdot$$

$$Q_2(x,\xi,z,t) = 0\ if\ \{\xi < 0\ \frac{x^2}{a^2} + \frac{y^2}{c_2^2} + \frac{\xi^2}{b^2} > 1 \quad (28)$$

In Eqs. 27 and 28, U is the net power of the electric arc defined as

$$U = \eta V I \tag{29}$$

where η the thermal efficiency of welding, V the average source voltage and I the average current of the welding source.

The terms f_1 and f_2 are constants that will represent fractions of heat deposited in the front and rear parts of the source, respectively, and must satisfy the following conditions (48)

$$f_f = \frac{2c_1}{c_1 + c_2} \tag{30}$$

$$f_r = \frac{2c_2}{c_1 + c_2} \tag{31}$$

$$f_f + f_r = 2 \tag{32}$$

The values used for the parameters in this work were taken from the experimental stage. Figs. 10, 11 and 12 show the shape of the double ellipsoid source in the mesh used in the numerical process. Fig. 10 shows the upper part of the part. The reddish region indicates the central region of the torch with the highest intensity of thermal energy.

Figure 10 – Double ellipsoid font shape representing propagation in simulated geometry with top view of part.

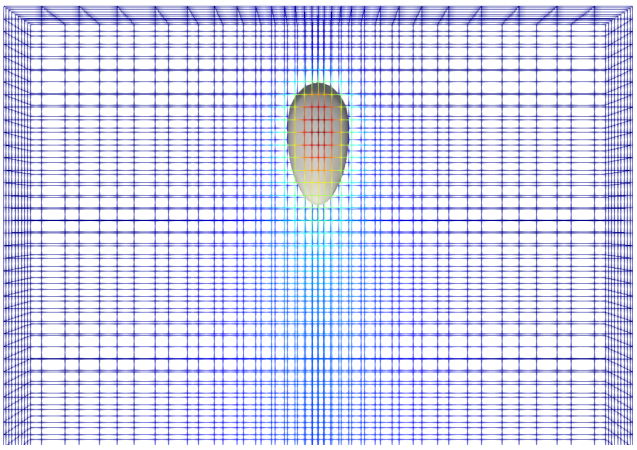

Source: The author (2025).

Fig. 11 shows the source from a bottom view of the part built on a simulated geometry.

Figure 11 – Double ellipsoid source shape representing propagation in simulated geometry with view of the base portion of the part.

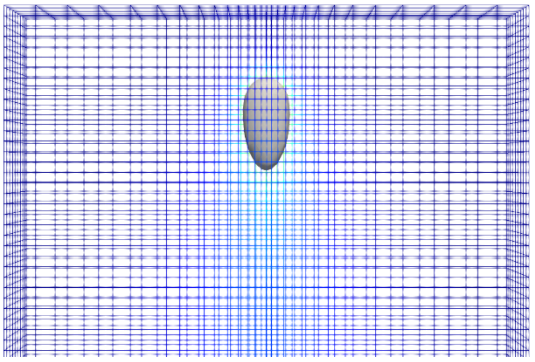

Source: The author (2025).

Fig. 12 shows a profile view of the source in the part indicating the penetration format of the heat source into the part.

Figure 12 – Double ellipsoid source shape representing propagation in simulated geometry with profile view.

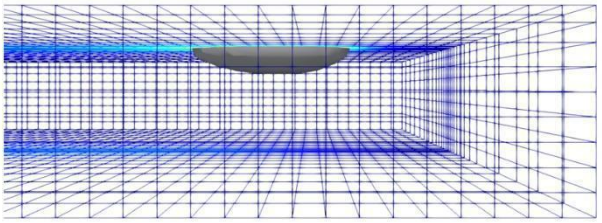

Source: The author (2025).

7.2 Semi Ellipsoid Model

The semi-ellipsoidal heat source is composed of half an ellipsoid as shown in Fig. 13.

$$Q_2(x,\xi,z,t) = \frac{6\sqrt{3}U}{a.b.c.\pi^{\frac{3}{2}}} e^{\left[-3\frac{(x-x_0)^2}{a^2} - 3\frac{\xi^2}{c^2} - 3\frac{(z-z_0)^2}{b^2}\right]} \; if \; \{\frac{x^2}{a^2} + \frac{\xi^2}{c_2^{\,2}} + \frac{z^2}{b^2} :$$

$$Q_2(x,\xi,z,t) = \; 0 \; if \; \{\frac{x^2}{a^2} + \frac{y^2}{c^2} + \frac{\xi^2}{b^2} > 1 \qquad (33)$$

Figs. 13, 14 and 15 show the shape of the semi-ellipsoid source in the mesh used in the numerical process. Fig. 13 shows the top of the part. The red region in the center of the source indicates the region of greatest intensity of thermal energy.

Figure 13 – Half-ellipsoidal source shape representing propagation in simulated geometry with a view of the top of the part.

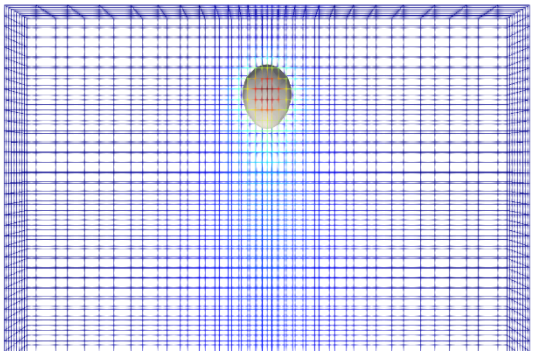

Source: The author (2025).

Fig. 14 shows the underside of the part and the distribution of power from the source within its dimensions.

Figure 14 – Half-ellipsoid source shape representing propagation in simulated geometry with view from underneath the part.

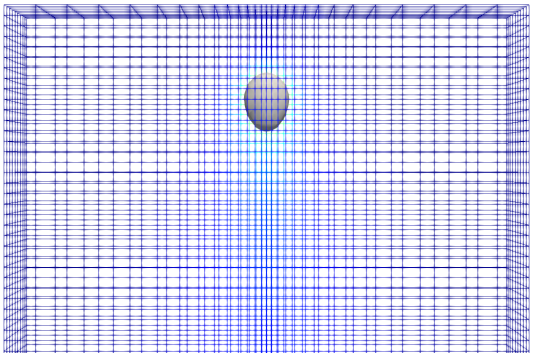

Source: The author (2025).

Fig. 15 presents a profile view of the semi-ellipsoidal source region.

Figure 15 – Shape of the semi-ellipsoid source representing propagation in the simulated geometry with profile view of the part.

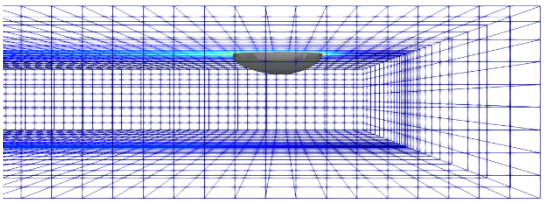

Source: The author (2025).

7.3 Double Ellipse Model

The double ellipse heat source is composed of half of an ellipse in the front plane as given by Eq. 34, and the other half in the rear region as given by Eq. 35.

$$Q_1(x,\ \xi,\ t) = \frac{6.U}{a\pi\left(c_1 + c_2\right)} e^{\left(-3\frac{\left(x-x_0\right)^2}{a^2} - 3\frac{\xi^2}{c_1^{\ 2}}\right)} \qquad if\ \{\xi \geq 0\ \frac{x^2}{a^2} + \frac{\xi^2}{c_1^{\ 2}} \leq$$

$$Q_1(x,\ \xi, t) = 0 \qquad if\ \{\xi \geq 0\ \frac{x^2}{a^2} + \frac{\xi^2}{c_1^2} \geq \quad (34)$$

$$Q_2(x,\ \xi, t) = \frac{6.U}{a\pi(c_1 + c_2)} e^{\left(-3\frac{(x-x_0)^2}{a^2} - 3\frac{\xi^2}{c_2^2}\right)} \qquad if\ \{\xi < 0\ \frac{x^2}{a^2} + \frac{\xi^2}{c_2^2}$$

$$Q_2(x,\ \xi, t) = 0 \qquad if\ \{\xi < 0\ \frac{x^2}{a^2} + \frac{\xi^2}{c_2^2} \quad (35)$$

Figs. 16, 17, and 18 show the shape of the double ellipse source in the mesh used in the numerical simulation. Fig. 16 shows the upper region of the piece. The reddish region in the center of the source indicates an area of greater intensity of thermal energy.

Figure 16 – Double ellipse font shape representing propagation in simulated geometry with top view of part.

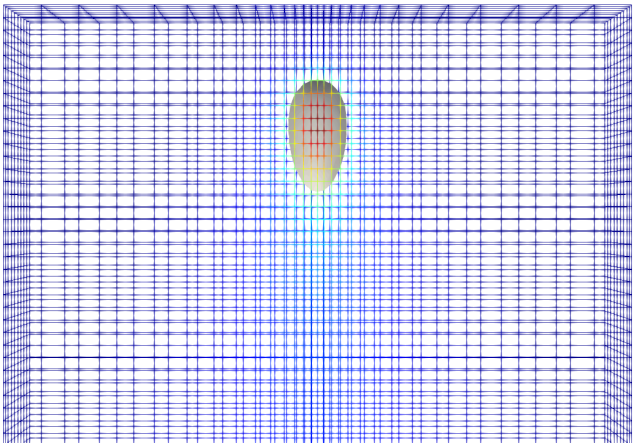

Source: The author (2025).

Fig. 17 shows the base of the welded part and the double ellipse source delimited by the dimensions defined in the simulation process.

Figure 17 – Double ellipse font shape representing propagation in simulated geometry with view of the underside of the part.

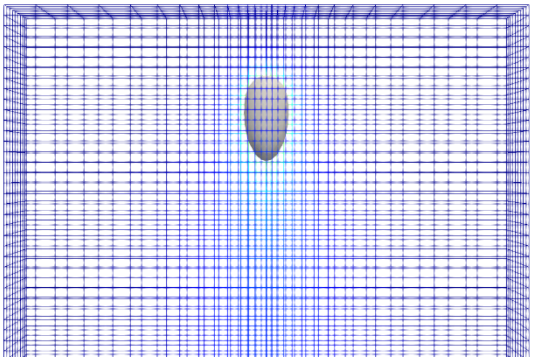

Source: The author (2025).

Fig. 18 shows the part in a profile view of the double ellipse source.

Figure 18 – Double ellipse font shape representing propagation in simulated geometry with profile view of part.

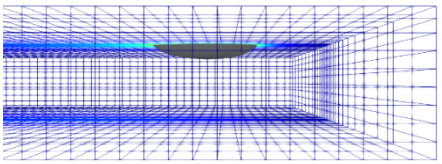

Source: The author (2025).

7.4 Circular Model

The circular heat source is defined by Eq. 36. Figs. 19, 20, and 21 show the shape of the circular source in the mesh used in the numerical process.

$$Q(x,\ \xi, t) = \frac{3U}{\pi a^2} e^{\left(-3\frac{(x-x_0)^2}{a^2} - 3\frac{\xi^2}{a^2}\right)} \qquad if,\ x^2 + \xi^2 \leq a^2 \tag{36}$$

$$Q(x,\ \xi, t) = 0 \qquad if, x^2 + \xi^2 > a^2$$

Fig. 19 shows the top view of the piece. The reddish region, at the center of the source, indicates the region of greatest intensity of thermal energy.

Figure 19 – Circular source shape representing propagation in simulated geometry with top view of part.

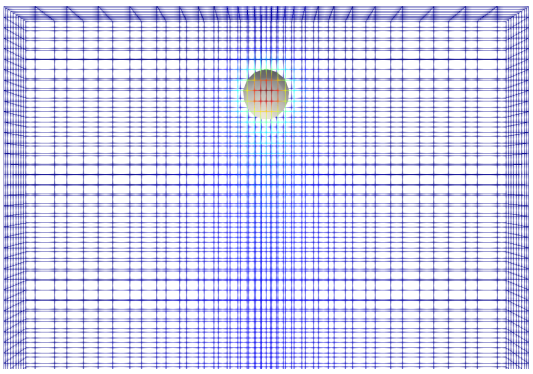

Source: The author (2025).

Fig. 20 shows the part from below and the distribution of the source within its dimensions.

Figure 20 – Circular source shape representing propagation in simulated geometry with a view of the underside of the part.

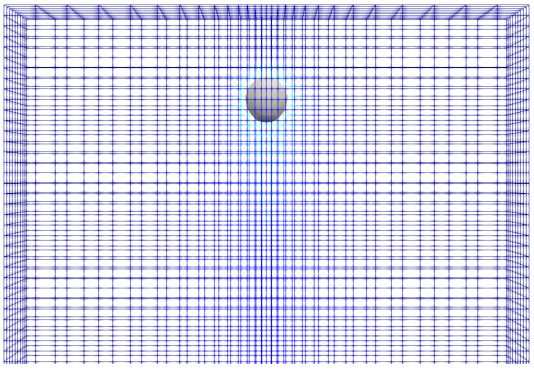

Source: The author (2025).

Fig. 21 presents a profile view of the circular source region.

Figure 21 – Shape of the semi-ellipsoid source representing propagation in the simulated geometry with profile view of the part.

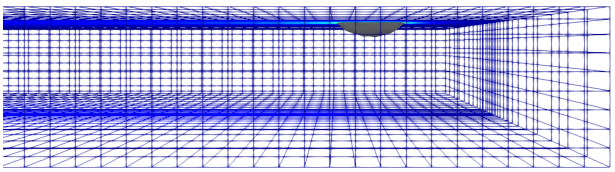

Source: The author (2025).

The relationship between the fixed coordinate system (x, y, z) and the moving coordinate system for each source can be expressed as

$$\xi = \left(y - y_0\right) - vt \tag{37}$$

where $\left(x_0, y_0, z_0\right)$ which defines the position of the heat source at the initial time, and v the speed of the welding source.

8 DISCRETIZATION PROCEDURE USING EBFVM

The approach that uses Finite Volume and divides the domain into elements is called *Element based Finite Volume Method* (EbFVM). This methodology subdivides the element into sub-elements that are called sub-control volumes (SVC). The number of subdivisions is associated with the number of vertices present in each element (41, 49, 50). Thus, the first-order triangular element has three sub-control volumes, while the bilinear quadrangular element has four, as shown in Fig. 22.

Figure 22 – Subdivision of elements in EbFVM.

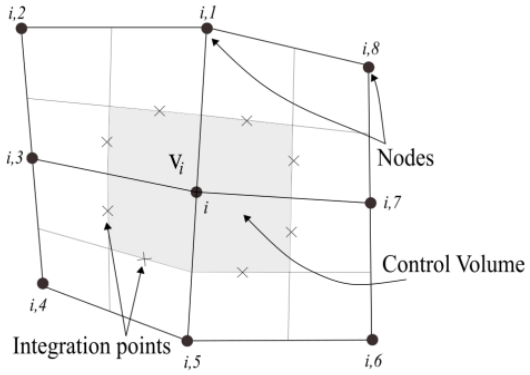

Source: The author (2025).

Usually, in the process of numerical integration, the mathematical models that describe the physical problem (under study) are written in integral form (weak form) and then transformed into a set of non-linear and linear equations (assuming that the terms that depend on temperature are non-linear). In particular, the methodologies that employ FV use the midpoint rule to discretize the equations. Then, within the context of EbFVM, the properties of interest are evaluated at each interface of the sub-control volume, that is, at the integration points. To obtain the approximation at each vertex, it is necessary to establish the control volume, which consists of all sub-elements vertex. The formulation responsible for this organization is known as *cell vertex formulation*. The cell vertex formulation was first proposed by Baliga and Patankar (1983) (51) using triangular elements and Schneide and Zedan (1982) (52) using quadrilaterals.

Since numerical methods using finite elements divide the continuous domain into small parts or elements, the continuous mathematical relations employed are also discretized. Therefore, there is a need to define a transformation that will be used to assist in the process

of discretizing the properties of interest, whether of a physical or geometric nature. For this purpose, the shape function is introduced in terms of parametric coordinates ξ and η which, for the isoparametric bilinear quadrilateral element, Fig. 23, can be represented in the form:

$$N_1(\xi,\eta) = \frac{1}{4}(1 - \xi - \eta + \xi\eta) \tag{38}$$

$$N_2(\xi,\eta) = \frac{1}{4}(1 - \xi + \eta - \xi\eta) \tag{39}$$

$$N_3(\xi,\eta) = \frac{1}{4}(1 + \xi + \eta + \xi\eta) \tag{40}$$

$$N_4(\xi,\eta) = \frac{1}{4}(1 + \xi - \eta - \xi\eta) \tag{41}$$

Thus, for an arbitrary continuous function, let that function be $\varphi(x, y)$, for any point within a quadrilateral element, it is valid:

$$\varphi(x,y) \approx \sum_{i=1}^{4} N_i \varphi_i \tag{42}$$

Figure 23 – Bilinear quadrilateral element represented in the Cartesian and parametric plane.

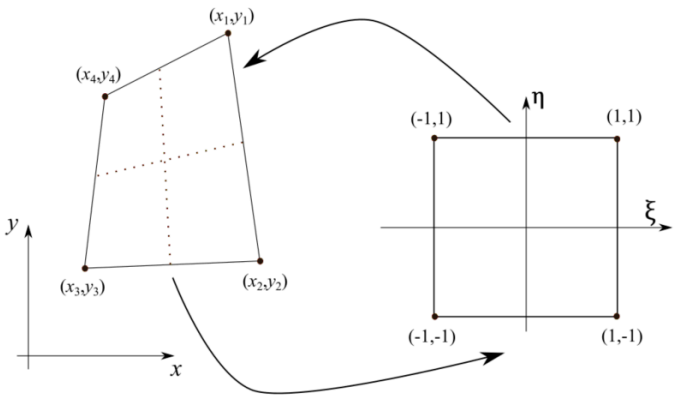

Source: The author (2025).

Additionally, the derivatives of the function in the Cartesian plane can be evaluated numerically in terms of the parametric coordinates as

$$\frac{\partial \varphi(\xi,\eta)}{\partial x} = \sum_{i=1}^{4} \frac{\partial N_i}{\partial x} \varphi_i \tag{43}$$

$$\frac{\partial \varphi(\xi,\eta)}{\partial y} = \sum_{i=1}^{4} \frac{\partial N_i}{\partial y} \varphi_i \tag{44}$$

since the derivatives of the shape functions use the mapping

$$\frac{\partial N_i}{\partial x} = \frac{1}{|J|}\left(\frac{\partial y}{\partial \eta}\frac{\partial N_i}{\partial \xi} - \frac{\partial y}{\partial \xi}\frac{\partial N_i}{\partial \eta}\right) \tag{45}$$

$$\frac{\partial N_i}{\partial y} = \frac{1}{|J|}\left(\frac{\partial x}{\partial \xi}\frac{\partial N_i}{\partial \eta} - \frac{\partial x}{\partial \eta}\frac{\partial N_i}{\partial \xi}\right) \tag{46}$$

where $|J|$ is the transformation matrix or Jacobian, which is expressed by:

$$|J| = \left(\frac{\partial x}{\partial \xi}\frac{\partial y}{\partial \eta} - \frac{\partial x}{\partial \eta}\frac{\partial y}{\partial \xi}\right) \tag{47}$$

In the integration process in EbFVM, the definition of the infinitesimal volume element is necessary and is written, for the two-dimensional case, in the form:

$$dV = dxdyh \tag{48}$$

where h arbitrary term representing the depth of the domain. In terms of the parameterized coordinates, the volume of element is rewritten as:

$$dV = \left(\frac{\partial x}{\partial \xi}\frac{\partial y}{\partial \eta} - \frac{\partial x}{\partial \eta}\frac{\partial y}{\partial \xi}\right)d\xi d\eta h \tag{49}$$

The normal are vector $\vec{ds}$ to the interfaces of each sub-control volume is given by

$$\vec{ds} = h\sum_{i=1}^{4}\left[\left(\frac{\partial N_i}{\partial \xi}d\xi + \frac{\partial N_i}{\partial \eta}d\eta\right)y_i\hat{i} - \left(\frac{\partial N_i}{\partial \xi}d\xi + \frac{\partial N_i}{\partial \eta}d\eta\right)x_i\hat{j}\right] \quad (50)$$

From the numerical foundations introduced for the two-dimensional case, extending these concepts to three-dimensional models are a straightforward task. In this work, other elements are adopted, such as the hexahedron, Fig. 24, whose shape functions in terms of parametric coordinates ξ, η, and ζ are given by:

Figure 24 – Parameterized hexagonal element highlighting the interfaces of each sub-control volume.

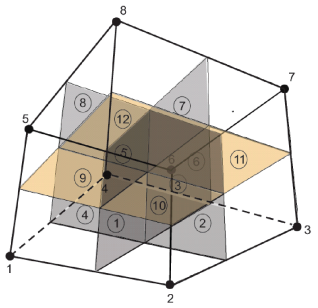

Source: (52, p. 283).

$$N_1(\xi, \eta, \zeta) = \frac{1}{8}(1 + \xi)(1 - \eta)(1 + \zeta) \quad (51)$$

$$N_2(\xi, \eta, \zeta) = \frac{1}{8}(1 + \xi)(1 - \eta)(1 - \zeta) \quad (52)$$

$$N_3(\xi, \eta, \zeta) = \frac{1}{8}(1 - \xi)(1 - \eta)(1 - \zeta) \quad (53)$$

$$N_4(\xi, \eta, \zeta) = \frac{1}{8}(1 - \xi)(1 - \eta)(1 + \zeta) \quad (54)$$

$$N_5(\xi, \eta, \zeta) = \frac{1}{8}(1 + \xi)(1 + \eta)(1 + \zeta) \quad (55)$$

$$N_6(\xi, \eta, \zeta) = \frac{1}{8}(1 + \xi)(1 + \eta)(1 - \zeta) \quad (56)$$

$$N_7(\xi, \eta, \zeta) = \frac{1}{8}(1 - \xi)(1 + \eta)(1 - \zeta) \tag{57}$$

$$N_8(\xi, \eta, \zeta) = \frac{1}{8}(1 - \xi)(1 + \eta)(1 + \zeta) \tag{58}$$

Thus, for a continuous function $\varphi(x, y, z)$ the derivatives are given by

$$\frac{\partial \varphi(\xi,\eta,\zeta)}{\partial x} = \sum_{i=1}^{NV} \frac{\partial N_i}{\partial x} \varphi_i \tag{59}$$

$$\frac{\partial \varphi(\xi,\eta,\zeta)}{\partial y} = \sum_{i=1}^{NV} \frac{\partial N_i}{\partial y} \varphi_i \tag{60}$$

$$\frac{\partial \varphi(\xi,\eta,\zeta)}{\partial z} = \sum_{i=1}^{NV} \frac{\partial N_i}{\partial z} \varphi_i \tag{61}$$

where *NV* is the number of vertices. The derivatives of the functions for the hexagonal element are written as:

$$\frac{\partial N_i}{\partial x} = \frac{1}{|J|}\left[\left(\frac{\partial y}{\partial \eta}\frac{\partial z}{\partial \zeta} - \frac{\partial y}{\partial \zeta}\frac{\partial z}{\partial \eta}\right)\frac{\partial N_i}{\partial \xi} - \left(\frac{\partial y}{\partial \xi}\frac{\partial z}{\partial \zeta} - \frac{\partial y}{\partial \zeta}\frac{\partial z}{\partial \xi}\right)\frac{\partial N_i}{\partial \eta} + \left(\frac{\partial y}{\partial \xi}\frac{\partial z}{\partial \eta} - \right. \tag{62}$$

$$\frac{\partial N_i}{\partial y} = \frac{1}{|J|}\left[-\left(\frac{\partial x}{\partial \eta}\frac{\partial z}{\partial \zeta} - \frac{\partial x}{\partial \zeta}\frac{\partial z}{\partial \eta}\right)\frac{\partial N_i}{\partial \xi} + \left(\frac{\partial x}{\partial \xi}\frac{\partial z}{\partial \zeta} - \frac{\partial x}{\partial \zeta}\frac{\partial z}{\partial \xi}\right)\frac{\partial N_i}{\partial \eta} - \left(\frac{\partial x}{\partial \xi}\frac{\partial}{\partial}\right. \tag{63}$$

$$\frac{\partial N_i}{\partial z} = \frac{1}{|J|}\left[\left(\frac{\partial x}{\partial \eta}\frac{\partial y}{\partial \zeta} - \frac{\partial x}{\partial \zeta}\frac{\partial y}{\partial \eta}\right)\frac{\partial N_i}{\partial \xi} - \left(\frac{\partial x}{\partial \xi}\frac{\partial z}{\partial \zeta} - \frac{\partial x}{\partial \zeta}\frac{\partial y}{\partial \xi}\right)\frac{\partial N_i}{\partial \eta} + \left(\frac{\partial x}{\partial \xi}\frac{\partial y}{\partial \eta}\right. \tag{64}$$

So that the Jacobian is given by:

$$|J| = \left(\frac{\partial y}{\partial \eta}\frac{\partial z}{\partial \zeta} - \frac{\partial y}{\partial \zeta}\frac{\partial z}{\partial \eta}\right)\frac{\partial x}{\partial \xi} - \left(\frac{\partial y}{\partial \xi}\frac{\partial z}{\partial \zeta} - \frac{\partial y}{\partial \zeta}\frac{\partial z}{\partial \xi}\right)\frac{\partial x}{\partial \eta} + \left(\frac{\partial y}{\partial \xi}\frac{\partial z}{\partial \eta} - \frac{\partial y}{\partial \eta}\frac{\partial}{\partial}\right. \tag{65}$$

The volume of the sub-control volume regular hexahedron is given by

$$V_{scv,i} = |J| \tag{66}$$

the area for quadrilateral integration surfaces is given by

$$d\vec{A} = \left(\frac{\partial y}{\partial \eta}\frac{\partial z}{\partial \zeta} - \frac{\partial y}{\partial \zeta}\frac{\partial z}{\partial \eta}\right)d\eta d\zeta \hat{i} + \left(\frac{\partial x}{\partial \xi}\frac{\partial z}{\partial \zeta} - \frac{\partial x}{\partial \zeta}\frac{\partial z}{\partial \xi}\right)d\xi d\zeta \hat{j} + \left(\frac{\partial x}{\partial \xi}\frac{\partial y}{\partial \eta} - \frac{\partial}{\partial}\right. \tag{67}$$

The reader is invited to have a more general overview of the numerical methods presented here in (8).

8.1 Numerical integration of the heat conduction equation with source term

The numerical integration of the heat conduction equation with source term in transient regime is performed for each sub-control volume V of the domain,

$$\int_t \int_V \rho(T)\frac{\partial(H(T))}{\partial t} dV dt = \int_t \int_V \nabla \bullet (\kappa \nabla T) dV dt + \int_t \int_V q dV dt + \int_t \int_s h\left(T_\infty \cdot\right.$$

(68)

Applying the Gauss's divergence theorem for the first term in the right-hand side of Eq. 68, we obtain

$$\int_t \int_V \rho(T)\frac{\partial(H(T))}{\partial t} dV dt = \int_t \int_s \kappa \nabla T \cdot \vec{ds} dt + \int_t \int_V q dV dt + \int_t \int_s h\left(T_\infty - T\right)d. \tag{69}$$

From the consideration of an arbitrary sub-control volume, the first term of Eq. 72 can be approximated by the midpoint rule as:

$$\int_t \int_V \rho(T)\frac{\partial(H(T))}{\partial t} dV dt \approx \left(\rho H_i|^{n+1} - \rho H_i|^n\right)\Delta V_i \tag{73}$$

For the diffusive term on the right of the equality, we have

$$\int_t \int_s (\kappa \nabla T) \cdot \vec{ds} dt = \theta \sum_{i=1}^{NV} \left(\sum_{j=1}^{NP} (k \nabla T)_j \cdot \vec{\Delta s}_j \right)_i^{n+1} \Delta t + (1 - \theta) \sum_{i=1}^{NV} \left(\sum_{j=1}^{NP} (k \nabla T)_j \cdot \right.$$

(74)

Note that the parameter θ ($0 \leq \theta \leq 1$) is used as a weight and is intended to evaluate the flow of a property of interest in the control volume during a time interval Δt. For the study in this work, implicit interpolation was used, which implies $\theta = 1$, i.e

$$\int_t \int_s (\kappa \nabla T) \cdot \vec{ds} dt = \sum_{i=1}^{NV} \left(\sum_{j=1}^{NP} (k \nabla T)_j \cdot \vec{\Delta s}_j \right)_i^{n+1} \Delta t \tag{75}$$

For the other parts of the Eq. 72, has been

$$\int_t \int_V q dV dt = q_i^{n+1} \Delta V_i \Delta t \tag{76}$$

and

$$\int_t \int_s h\left(T_\infty - T\right) ds dt = h\left(T_\infty - T_i\right)^{n+1} \Delta s_i \Delta t \tag{77}$$

Substituting the Eqs. 73, 75, 76 and 77 in Eq. 72, obtain

$$\left(\rho H_i|^{n+1} - \rho H_i|^n\right) \Delta V_i \approx \sum_{i=1}^{NV} \left(\sum_{j=1}^{NP} (\kappa \nabla T)_j \bullet \vec{\Delta s}_j \right)_i^{n+1} . \Delta t + q_i^{n+1} \Delta V_i \Delta t + h\left(\tag{78}$$

We have the following system of nonlinear algebraic equations, considering all control volume equations in a mesh:

$$A^{n+1}H^{n+1} = B^{n} \tag{79}$$

where A the coefficient matrix, H the vector of enthalpies at the nodes, and B the vector of independent terms. It is important to highlight that the nonlinearities introduced in the system of equations above are due to properties dependent on temperature, heat source and boundary conditions.

To solve the thermal problem, which is given by Eq. 79, an incremental procedure was used. The incremental approach (time marching) starts with a certain initial enthalpy field H_0. Then the system of nonlinear algebraic equations is solved. Finally, the enthalpy H is attributed to T_0 so that the temperature field is updated and the solution keeps adding new time steps. However, due to nonlinearities, an iterative procedure needs to be performed during this process.

8.2 Iterative solution method for thermal analysis

Eq. 79 is a nonlinear system of equations, so an iterative approach is required to linearize and subsequently solve them at each time step. To accomplish this task, the Newton-Raphson iterative method is used. Eq. 79 is rewritten as follows

$$A_{i+1}^{n+1}H_{i+1}^{n+1} - B_{i+1}^{n} = R_{i+1}^{n+1} \tag{80}$$

where R is a residue vector and the subscript i is the iteration counter. Iterative corrections to the enthalpy increment are made through a predictor H_i for the first iteration and subsequently by an iterative corrector δH_i. This can be calculated mathematically as

$$H_{i+1}^{n+1} = H_{i}^{n+1} + \delta H_i \tag{81}$$

Then one must find the iterative correction that can be obtained $R_{i+1}^{n+1} = 0$ in the following iteration. This can be achieved by

$$R_{i+1}^{n+1} \approx R_i^{n+1} + \frac{\partial R^{n+1}}{\partial H}\delta H_i = 0 \tag{82}$$

Eq. 82 can be written as

$$-\frac{\partial R^{n+1}}{\partial H}\delta H_i = R_i^{n+1} \tag{83}$$

In Eq. 83, the derivatives can be calculated as follows

$$-\frac{\partial R^{n+1}}{\partial H} = \left(\frac{\partial A_i^{n+1} H_i^{n+1}}{\partial H} - \frac{\partial B_i^n}{\partial H}\right) \approx -A_i^{n+1} \tag{84}$$

Therefore, the increase δH_i can be finally calculated as

$$\delta H_i = -\left[A_i^{n+1}\right]^{-1} R_i^{n+1} \tag{85}$$

The incremental and iterative procedures for solving the heat conduction equation are summarized in Fig. 25.

Figure 25 – Incremental and iterative procedures.

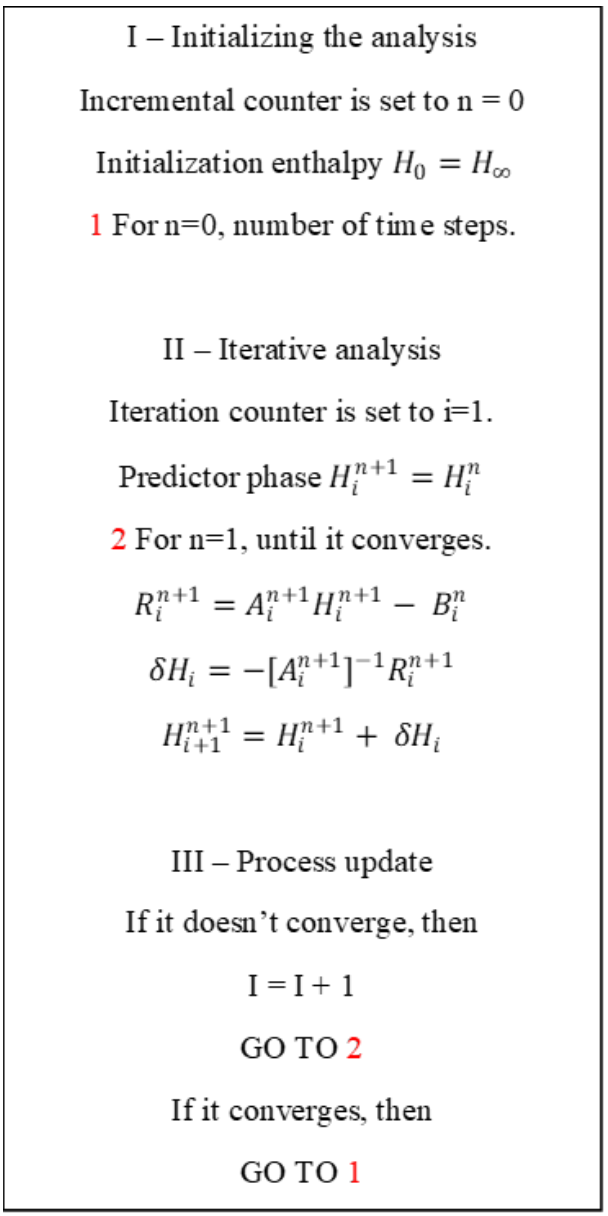

Source: The author (2025).

9 SIMULATOR VALIDATION

Fig. 26 shows a layout of a steel plate with dimensions and positions of thermocouples on the upper and lower surfaces taken from the literature (55). Data taken from the literature were used to validate the code written using the EbFVM methodology.

Figure 26 – Steel plate under analysis of the welding process. (a) Represents the top of the plate and the temperature capture points. (b) Represents the base of the plate and the temperature capture points.

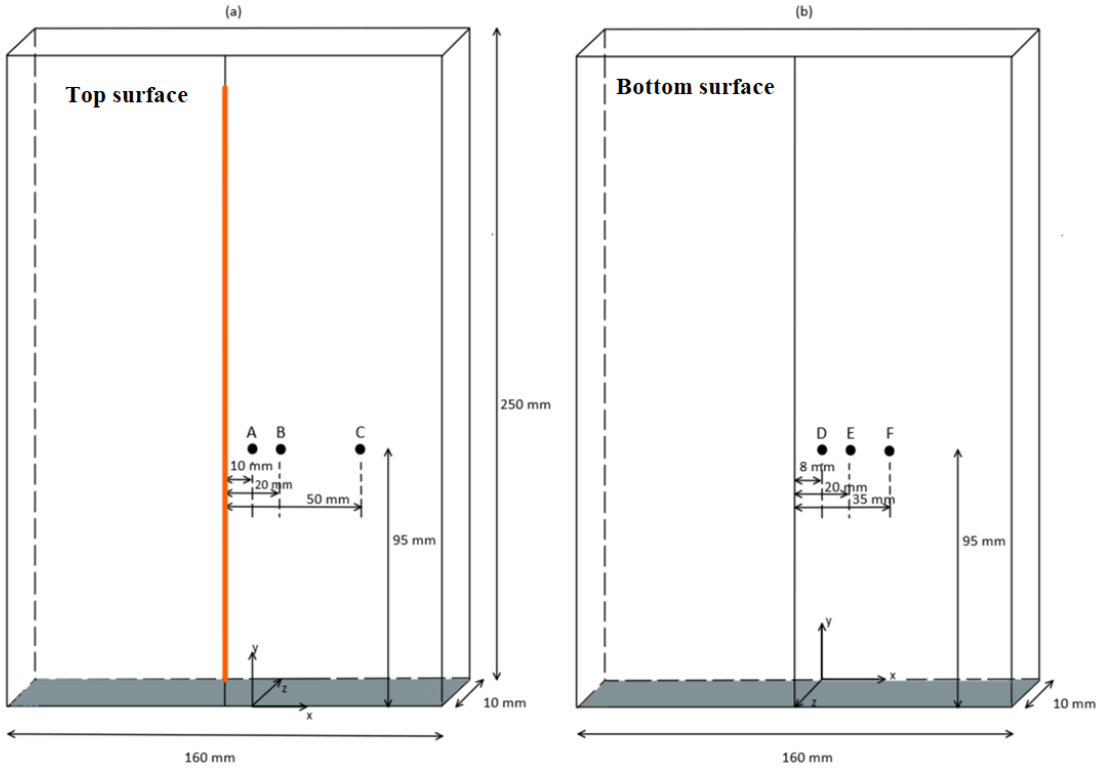

Source: The author (2025).

The welding process took as data the welding voltage was 10 V, the welding electric current was 150 A, the welding efficiency was 0.65 and the torch speed was 1 mm/s. Welding starts at position (80, 10, 0) mm and ends at (80, 240, 0) mm. The convection coefficient is h=10W/m² °C and the initial temperature is 29 °C (55).

Fig. 27 shows the 3D mesh used in the plate simulation process. The refinement is greater between the positions, x = 0 mm and x = 20 mm, as this is a region of greater temperature gradient. Between x = 20 mm and x = 35 mm, the refinement is smaller than the

first and larger than the region between x = 35 mm and x = 80 mm. For simplicity, and due to the symmetry of the problem, only one side of the plate was generated.

Figure 27 – 3D mesh used in the simulation process.

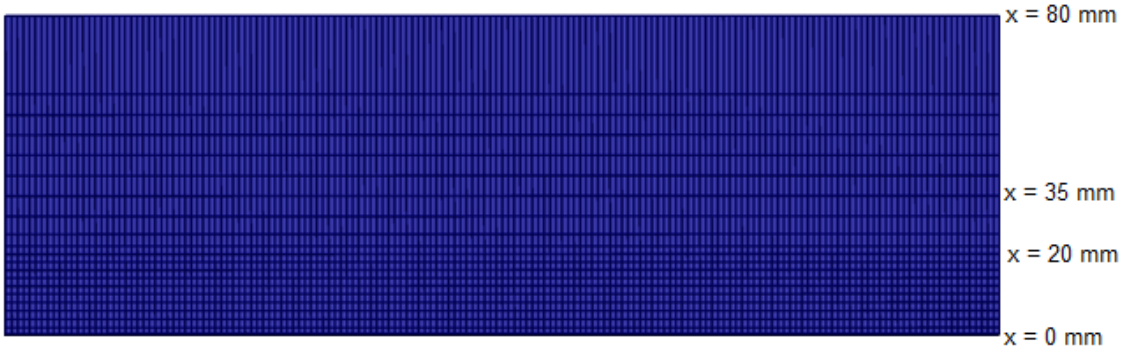

Source: The author (2025).

9.1 Code validation with literature.

Fig. 28 shows the position of the source at the top of the plate, Fig. 29 a profile view of the source on the plate and Fig. 30 the position of the source at the base of the plate at times 50s, 100s and 150s, respectively.

Figure 28 – Temperature field in degrees Celsius at the top of the plate (a) t =50 s, (b) t =100 s and (c) t =150s.

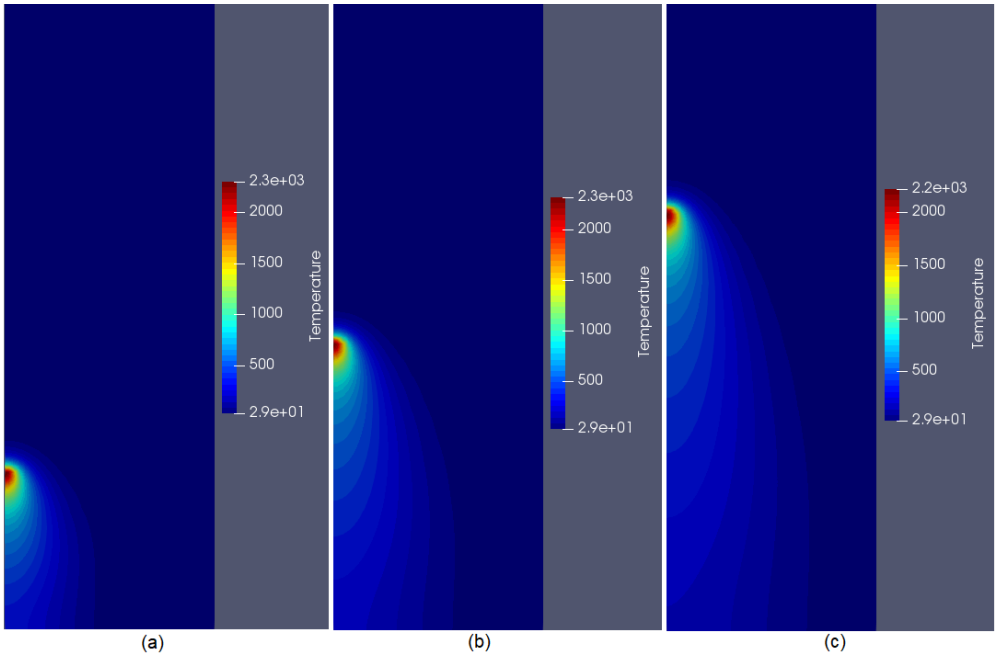

Source: The author (2025).

The evolution of the temperature field is influenced by the parameters of the heat source and the welding heat input. The contours of this field are directly influenced by the welding speed and the physical properties of the material (54).

Figure 29 – Temperature field in Celsius degress, the profile view of the plate. (a) t = 50s, (b) t = 100s and (c) t = 150s.

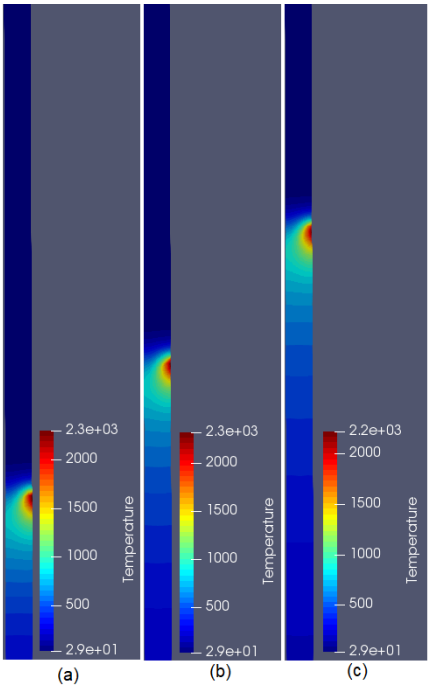

Source: The author (2025).

Figure 30 – Temperature field in Celsius degrees at the base of the plate. (a) t =50s, (b) t = 100s and (c) t = 150s.

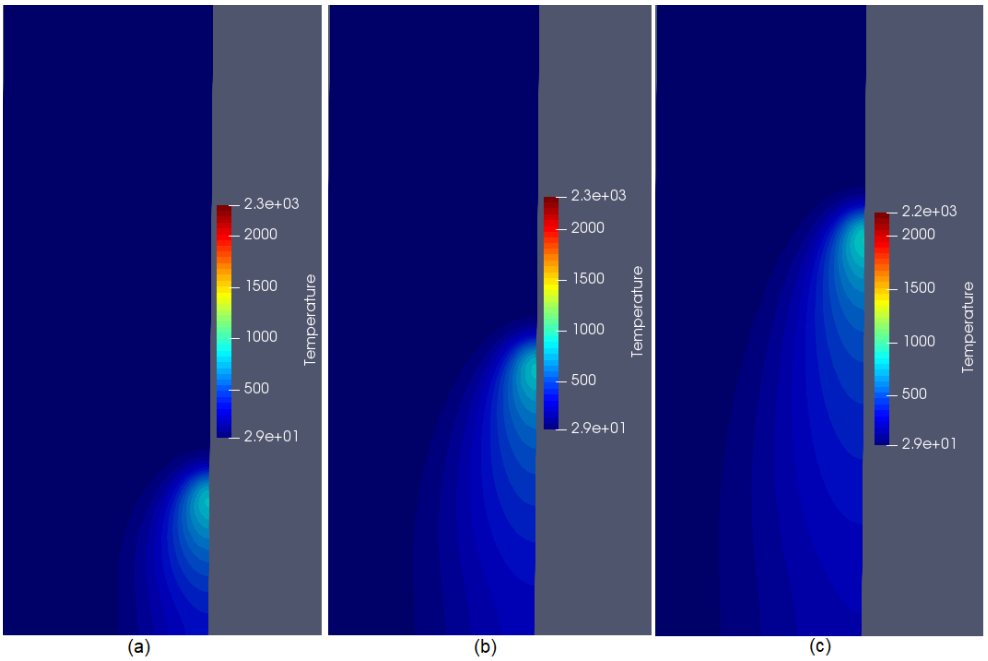

Source: The author (2025).

Fig. 31 presents the comparison of results extracted from the literature (55) with numerical results using the EbFVM method. The temperature fields presented in Fig. 31 were captured at the base of the plate.

Figure 31 – Results obtained by 3D simulation and experimental taken at the base of the plate.

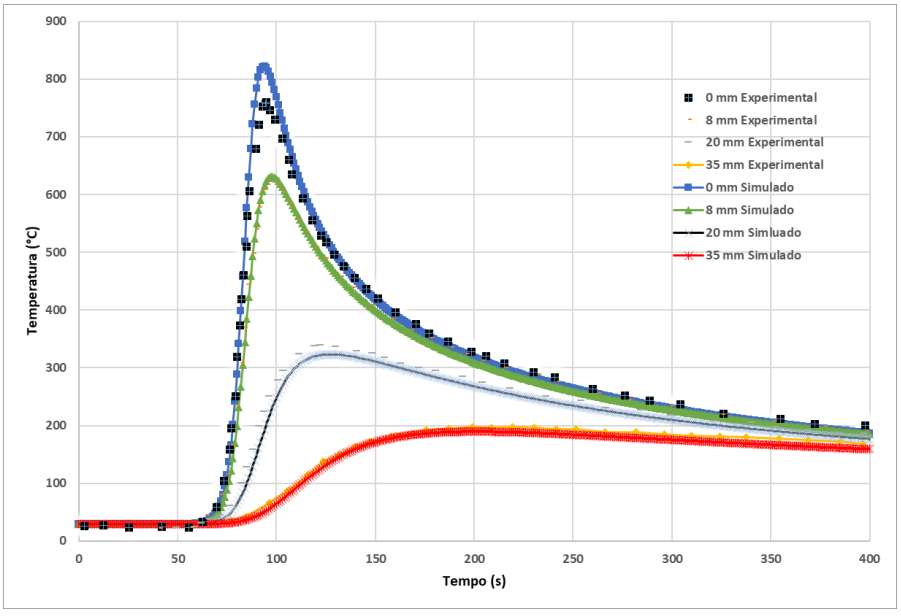

Source: The author (2025).

The thermal cycles shown in Fig. 32 were captured on top of the plate.

Figure 32 – Results obtained by 3D simulation and experimental taken from the top of the plate.

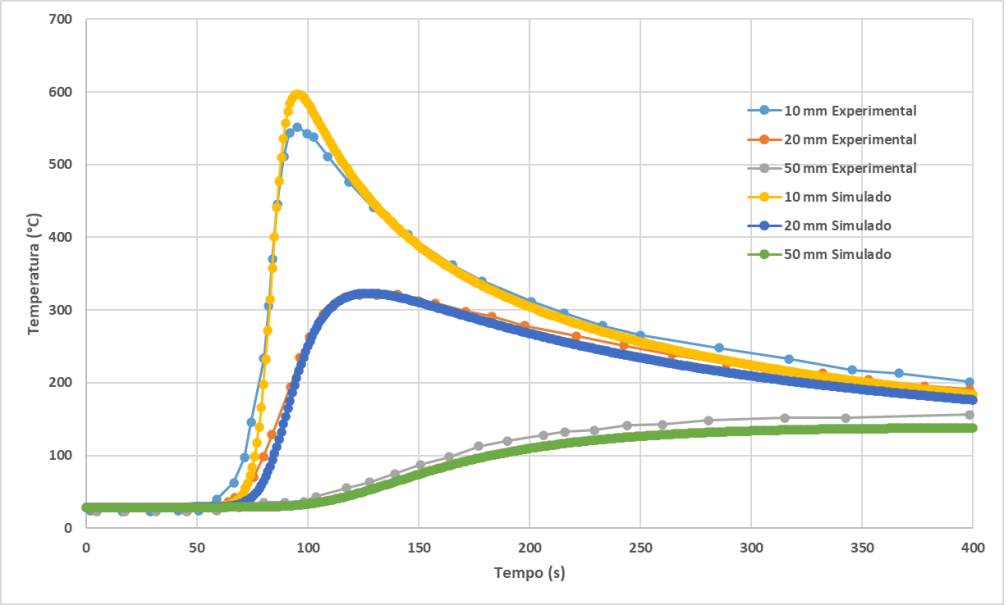

Source: The author (2025).

The numerical results obtained in the 3D simulation and compared with the experimental results generally have a high degree of agreement. Fig. 31 for thermal cycles captured at the base of the board the values furthest from the weld bead present similar heating and cooling profiles as well as peak temperature. For the thermocouple located exactly below the weld bead, the heating and cooling profiles are similar. The peak temperature value for the region indicating the peak temperature has divergence, with the simulated value being greater than the experimental value.

Fig. 32 presents similarity in behavior with the results presented in Fig. 31. The value of the thermal cycle captured closest to the weld bead has divergence in the peak region and similar behavior of temperature variations in the heating and cooling regions. For thermal cycle capture points in the region furthest from the weld bead, the thermal cycles have good behavior agreements in the heating and cooling regions as well as in the peak temperature position.

Given the simulations carried out and their results compared to experimental data extracted from the literature (55), it was possible to estimate confidence in the code written using the EbFVM methodology.

9.2 Mesh refinement study

The equations that govern the energy balance are evaluated by means of the integral at the midpoint of the interfaces of the control volumes of the mesh. The non-uniform mesh used was the one with the best result accuracy. The mesh was refined only in the weld bead region to reduce the computational time, see Fig. 33. Therefore, the mesh used has larger element sizes in regions far from the fusion zone when compared to those close to the fusion zone. This is a very desirable feature since the thermal problem in welding is highly non-linear (56).

Figure 33 – Mesh with refinement located in the center.

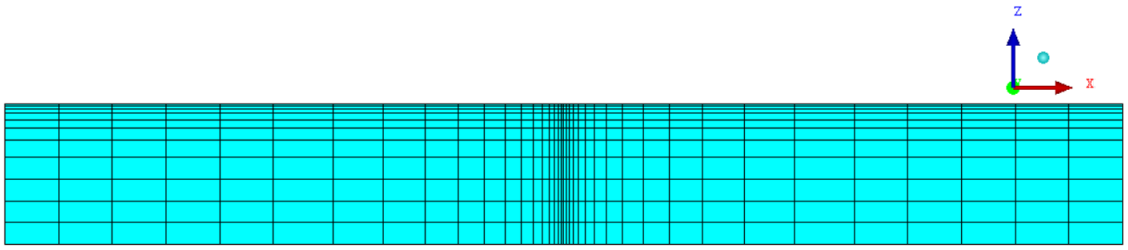

Source: The author (2025).

Table 2 shows the number of nodes and elements of the meshes used in the simulations. After analysis of the results, the third mesh was chosen.

Table 2 – Number of nodes used for each case.

Welding process AISI 409 ferritic		
Type of element	**Node**	**Element**
Hexahedron First Mesh	56350	47040
Hexahedron Second Mesh	81807	72000
Hexahedron Third mesh	150228	133760
Hexahedron Fourth mesh	284085	259840

Source: The author (2025).

Fig. 34 presents the liquid mass fraction using the four hexahedron grids at 10 seconds after the welding process starts.

Figure 34 – Cross-section perpendicular to the torch movement. (a) torch position at t = 10s - mesh with 259,840 elements. (b) torch position at t = 10s - mesh with 133,760 elements. (c) torch position at t = 10s - mesh with 72,000 elements. (d) torch position at t = 10s – mesh with 47040 elements.

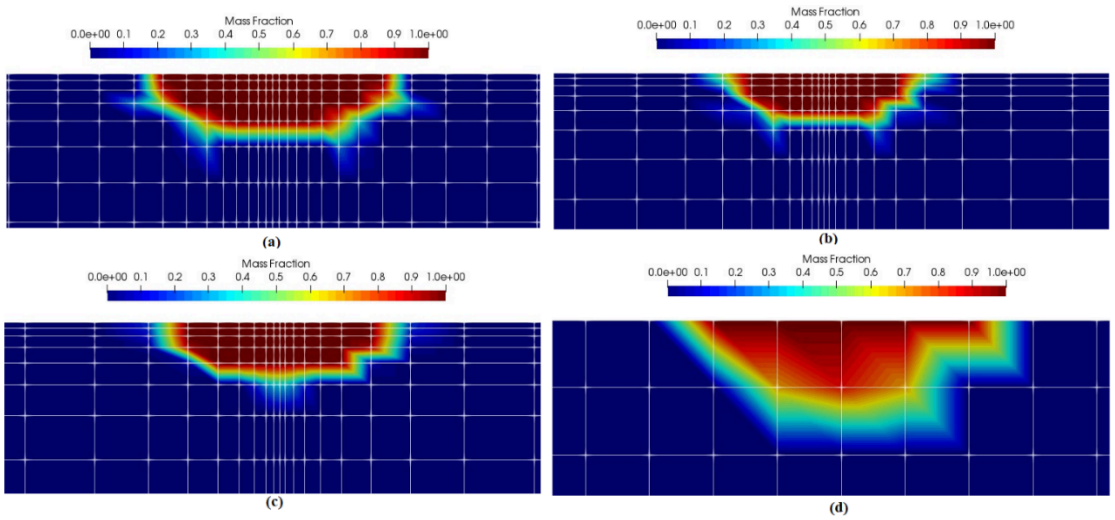

Source: The author (2025).

9.3 Analysis of input parameters

The model used is sensitive to the source input variables. Fig. 35 shows the fraction of liquid for different values of current used as input variable. A comparison of the numerical results, in terms of melt zone, with the experimental ones is shown in Fig. 56 indicating the similarity of dimensions for the melt, the heat-affected zone, and the base metal.

Figure 35 – (a) Current equal to 165A. (b) Current equal to 215A. (c) Current equal to 265A.

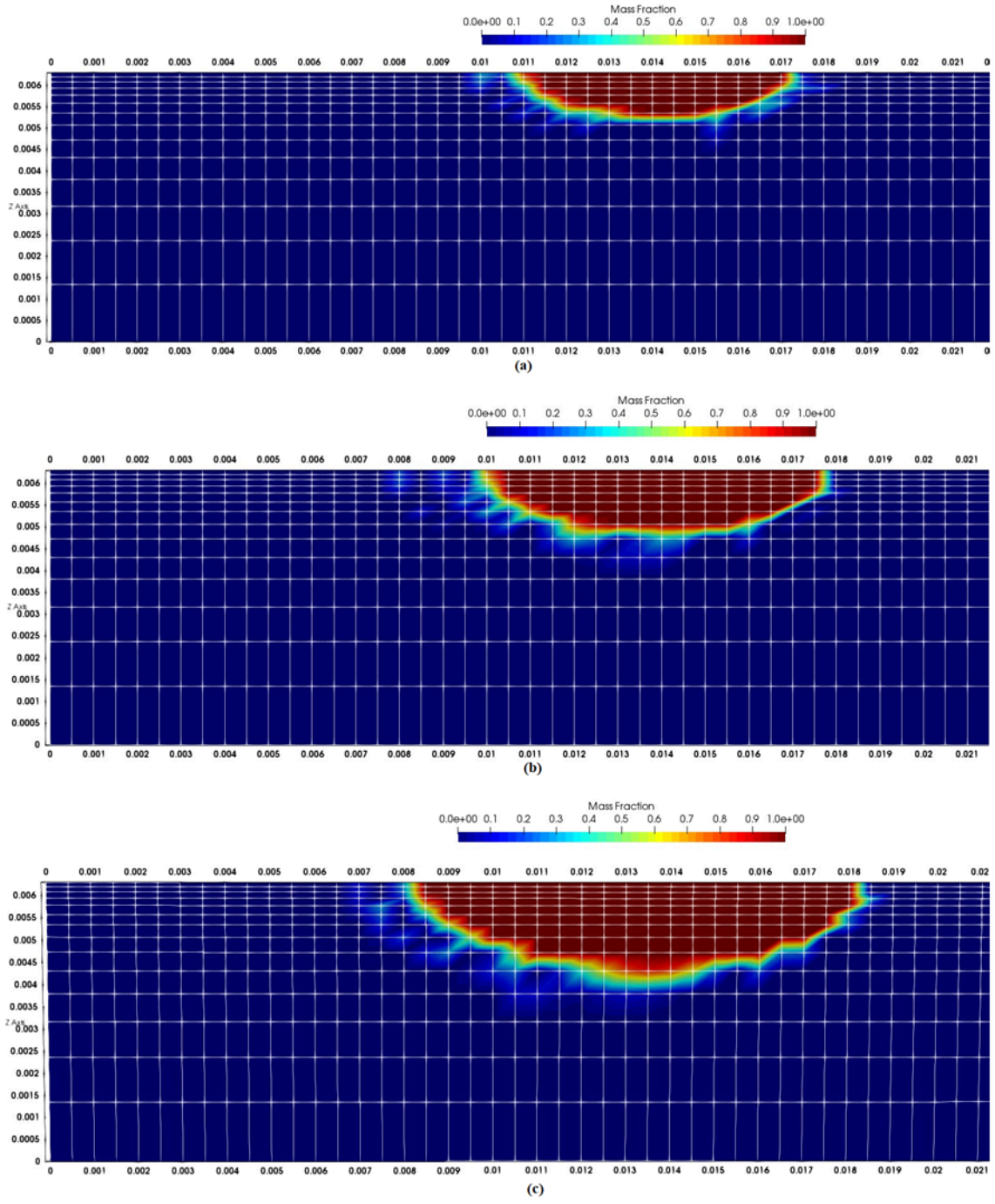

Source: The author (2025).

Fig. 36 shows that the average mass fraction increases from 7.75% to 25.44% as the source power increases from 1320W to 2120W.

Figure 36 – Impact of power on the average mass fraction of the base metal.

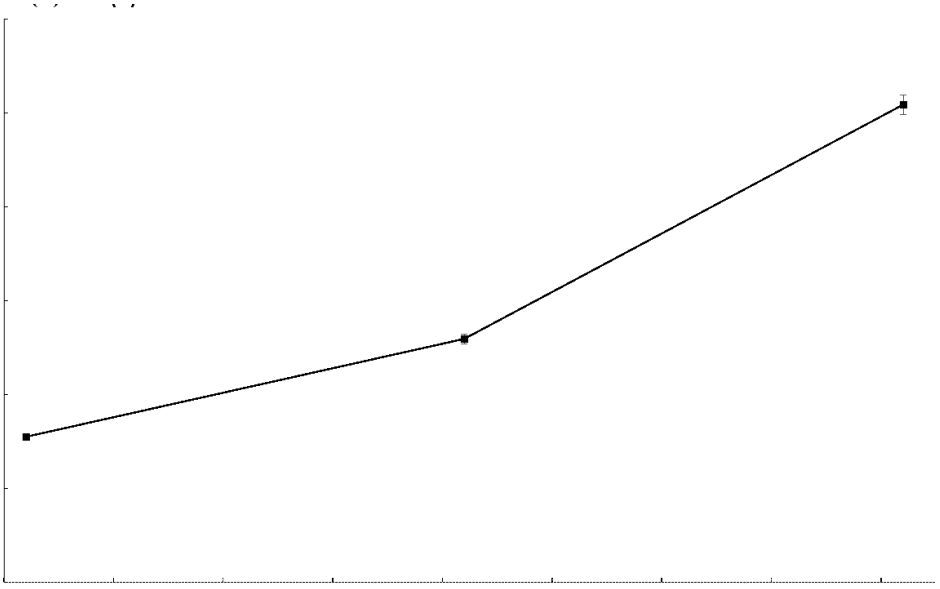

Source: The author (2025).

The analysis of the liquid fraction of the molten zone in the weld bead region corroborates to solidify the accuracy between the mathematical model and the experimental process. For this purpose, macrographic analyses of the weld bead region were carried out in the AISI 409 ferritic steel sample and the melted pool geometries of the four sources used in the numerical simulation process (57). The results can be seen in section 10.2 this work.

10 MATERIALS, EQUIPMENT, AND METHODS

This chapter will describe the materials used in the experimental welding procedure, the macrographic analysis stage for acquiring values of the geometry of the energy source and the mesh used in the numerical simulation stage.

10.1 Base Metal AISI 409

AISI 409 stainless steel plates with dimensions of 160 mm in length, 50 mm in width and 6.3 mm in thickness and chemical compositions indicated in Tab. 3 were used as base metal for the autogenous GTAW welding process.

Table 3 – Chemical composition of AISI 409 ferritic steel in mass fraction (%).

Cr	Mn	Fe	Si	P	S	Ni
10,75	0,821	87,05	0,706	0,034	33	0,455

Source: The author (2025).

The thermophysical properties of the steel used in the experimental stage are presented in Figs. 37 - 39. These properties were provided by the JMatpro@ software.

Figure 37 – Thermal conductivity as a function of temperature.

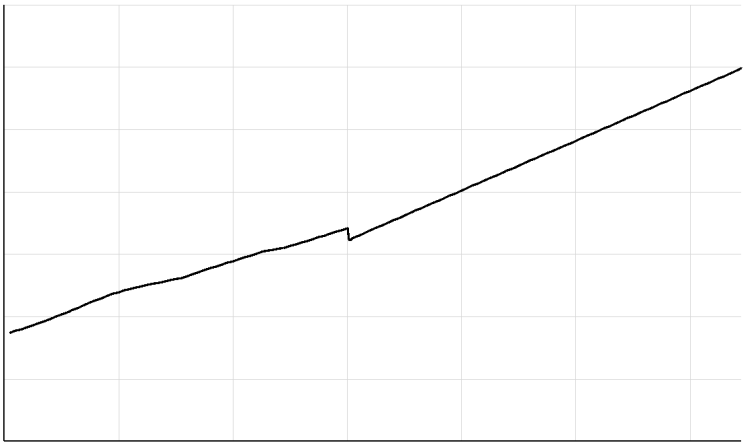

Source: The author (2025).

Figure 38 – Density as a function of temperature.

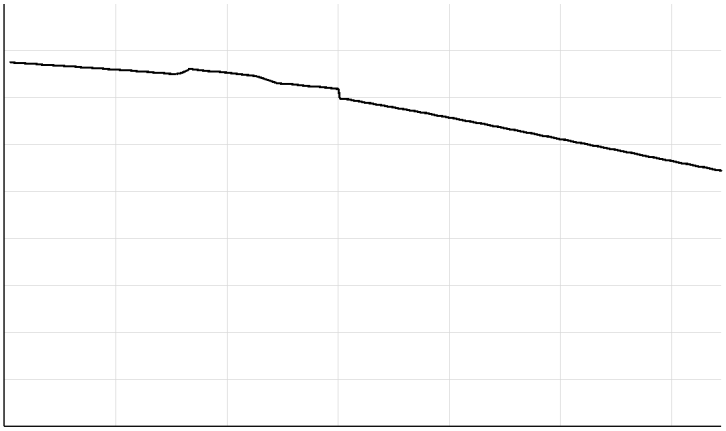

Source: The author (2025).

Figure 39 – Specific heat as a function of temperature.

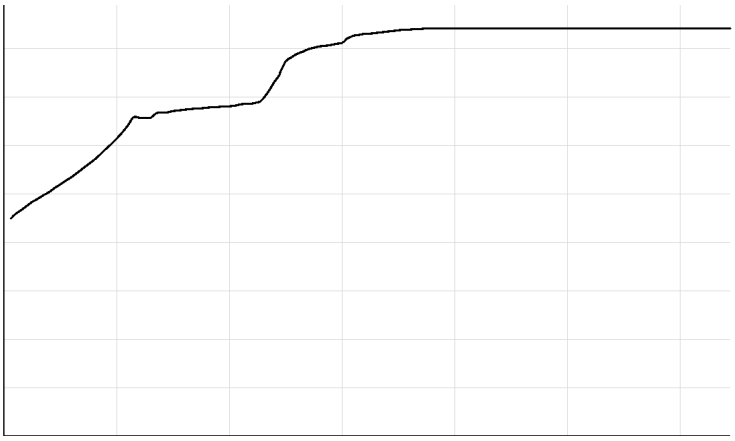

Source: The author (2025).

The materials were provided by LPTS-UFC (Welding Research and Technology Laboratory) of the Federal University of Ceará.

10.2 Welding

The electrode used in welding, with an average current of 165 A, was pure tungsten with a diameter of 2.4 mm. For an average current of 216 A, an electrode made of the same material and with a diameter of 3.2 mm was used. The distances between the electrodes and the surface of the steel workpiece (Electrode to Workpiece Distance - DEP) adopted in the experimental tests are their respective diameters. The electrodes were sharpened at an angle of 45°, see Fig. 40.

Figure 40 – Electrode tip before welding.

Source: The author (2025).

Fig. 41 shows all the equipment used to perform the TIG welding process. Item “A” in Fig. 41 indicates the argon cylinder, “B” the computer with software for capturing temperature fields, “C” and “D” the Tartilope (welding automation system) and “E” the amplifier for acquiring temperatures (MX 1609KB) connected to type k thermocouples (Cromel-Alumel).

Figure 41 – Description of equipment used in the experimental procedure.

Source: The author (2025).

A steel rail was designed to support the AISI 409 samples that were welded to acquire experimental thermal cycles used in this work. Two small steel pieces were positioned at the lower ends (position A and B) of the sample to reduce the loss of thermal energy by conduction, see Fig. 42.

Figure 42 – Top of the AISI 409 steel sample with the three thermocouples attached.

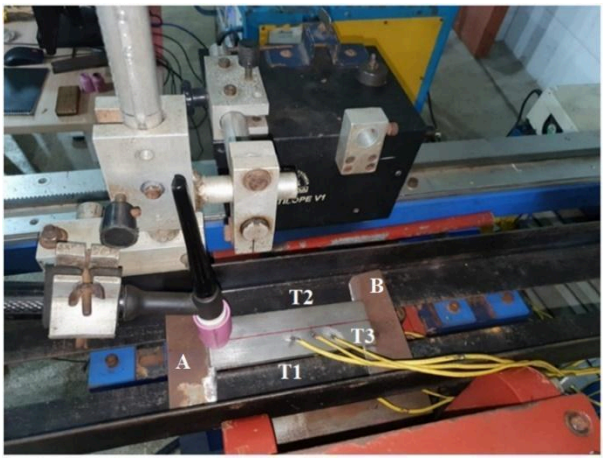

Source: The author (2025).

Three k-type thermocouples were fixed on top of the AISI 409 ferritic stainless-steel sample. The first thermocouple, T1, was fixed 80 mm from the start of the torch path and perpendicularly 8 mm from the center of the weld bead. The thermocouple, T2, was fixed 20 mm after the thermocouple T1 and perpendicularly distant 7 mm from the center of the weld bead. Thermocouple T3 was fixed 20 mm after thermocouple T2 and perpendicularly distant 13 mm from the center of the weld bead. The T2 thermocouple, although well fixed, unfortunately did not capture the voltage signals generated during welding, which made it impossible to record the thermal cycles.

Three thermocouples (T4, T5 and T6) were fixed to the lower surface of the AISI 409 stainless steel sheet, opposite side of the electric arc. Thermocouple T4 was 80 mm and T6 120 mm from the initial position of the torch, they were fixed 2.96 mm and 2.92 mm, respectively, inside the sample from the base and thermocouple T5 was fixed at the base of the sample 100 mm away from the initial position of the torch as shown in Fig. 43.

Figure 43 – View of the bottom surface of the AISI 409 steel sample, before welding at 165 A, with three thermocouples attached.

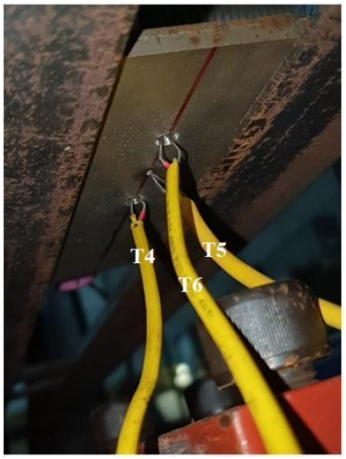

Source: The author (2025).

Fig. 44 shows the AISI 409 sample after the fourth autogenous TIG pass with a current indicated at the source of 165 A and a voltage of 15.1 V.

Figure 44 – Sample of AISI 409 steel after fourth TIG welding pass with 165A current.

Source: The author (2025).

Fig. 45 shows the bench used to perform the experiment in operation.

Figure 45 – Workbench in operation carrying out TIG welding process.

Source: The author (2025).

Another stage of the experiment was changing the electric current used in the TIG welding process from 165 A to 210 A, with the aim of increasing the welding energy. At the end of the experiment, the average current indication was 216 A with an average voltage of 13.7 V. The diameter of the electrode used in this stage of the experiment was 3.2 mm and its distance to the part was also set at 3.2 mm.

Fig. 46 shows a sample of AISI 409 steel with the same dimensions as the previous experiment. At this stage, only four thermocouples were used, one on the top and the other three on the bottom surface of the piece. Figs. 46 and 47 shows the positions of the thermocouples.

Figure 46 – Top of AISI 409 steel sample with a thermocouple fixed 13 mm from the center of the weld bead.

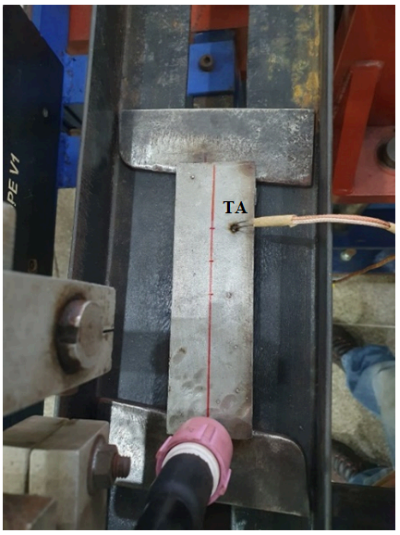

Source: The author (2025).

Figure 47 – Base of the AISI 409 steel sample, before welding at 216 A, with three thermocouples attached.

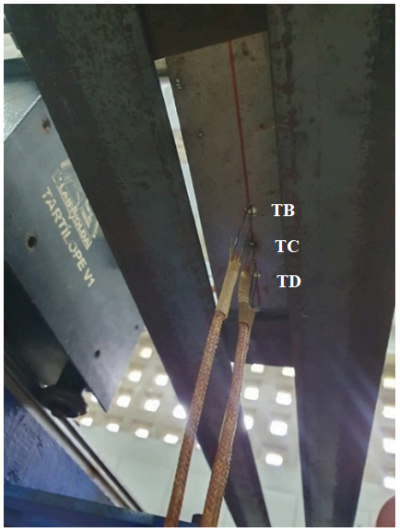

Source: The author (2025).

Fig. 48 shows the AISI 409 steel sample after the fourth TIG welding pass at 216 A and 13.7 V.

Figure 48 – Sample of AISI 409 steel after fourth TIG welding pass with 216A current.

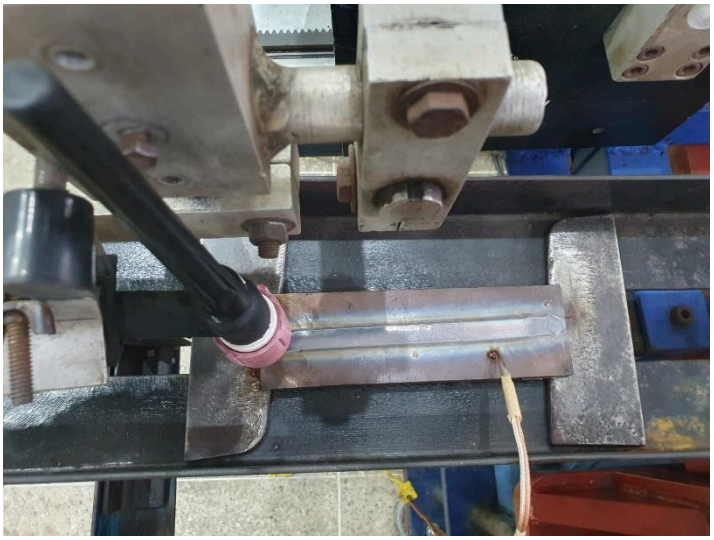

Source: The author (2025).

Fig. 49 shows the tip of the electrode after the four passes with the current of 216 A.

Figure 49 – Electrode tip after four passes of TIG welding using 216 A current.

Source: The author (2025).

The speed used to move the torch in the autogenous TIG welding process was 4 mm/s. The inter-pass temperature for each sample was monitored by the thermocouple fixed to the lower surface of the part at a position 100 mm from the start of the weld bead. That is, for the welding process with a current of 165A, the thermocouple used as a reference was T5

and for the welding process with a current of 216A, the thermocouple used as a reference was TC.

10.3 Analysis of weld bead geometry.

In order to use in the numerical stage of the simulation of the autogenous TIG welding process, the correct dimensions of width and depth of the molten pool of a welding pass, a macro structural analysis of a section of the weld bead was carried out for the two current values electricity used in the experimental stage. The results are shown in Fig. 50(a) for 165 A current and Fig. 50(b) for 216 A current.

Figure 50 – (a) Cross-section of the weld bead, after the first pass, with the dimensions of width and depth using a current of 165A and (b) 216A.

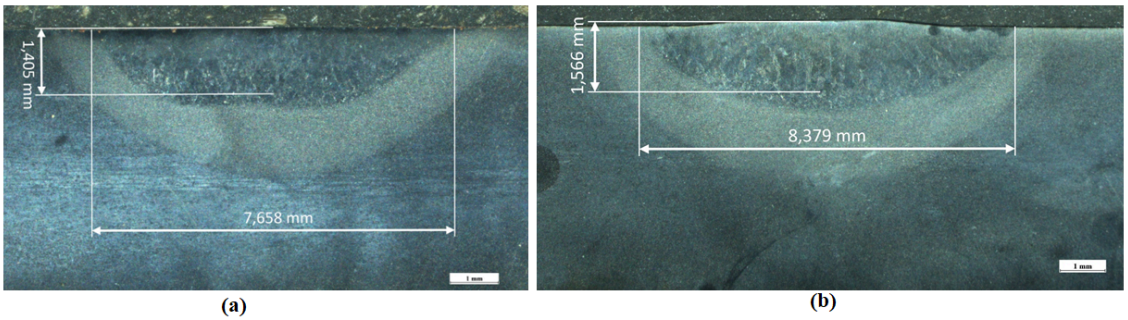

(a) (b)

Source: The author (2025).

Fig. 50(a) shows a weld bead profile with width of 7.65 mm, depth of 1.4 mm. In Fig. 50(b) the weld bead profile has dimensions of 8.37 mm in width and 1.55 mm in depth.

Fig. 50 show three well-defined regions after the four welding passes of the experimental process in AISI 409 steel. It is easy to identify the fusion zone, where temperatures exceed the melting point temperature and, therefore, solidification; the heat-affected zone, where the melting temperature is not reached, but microstructural changes occur in this region, such as grain growth; and the third region, the base metal, where the microstructure is not affected because it does not reach temperature ranges that contribute to microstructural changes.

Figs. 51 and 52 clearly show the two regions: molten zone (FZ), heat-affected zone of coarse grain (HAZ-CG) of the AISI 409 steel sample after the first pass of torch.

Figure 51 – Microstructures of AISI 409 steel after first welding pass with an average current of 165A.

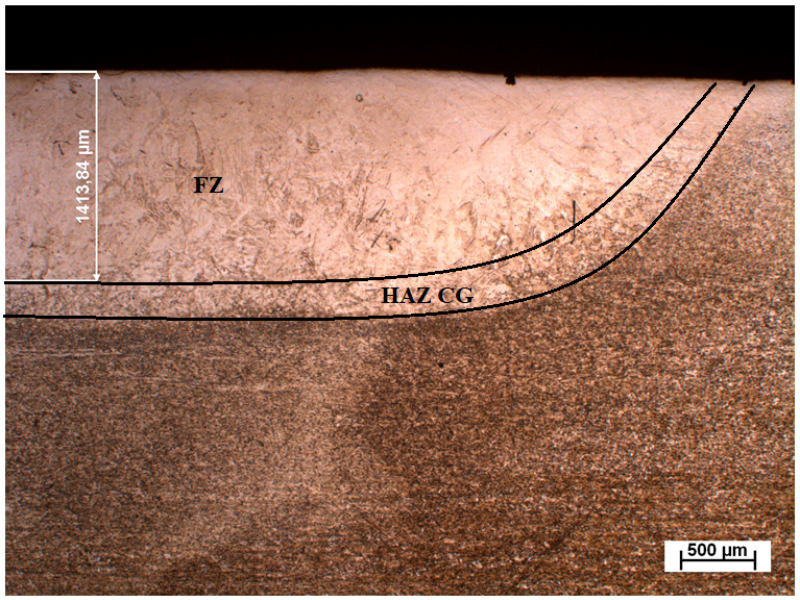

Source: The author (2025).

Figure 52 – Microstructures of AISI 409 steel after first welding pass with an average current of 216A.

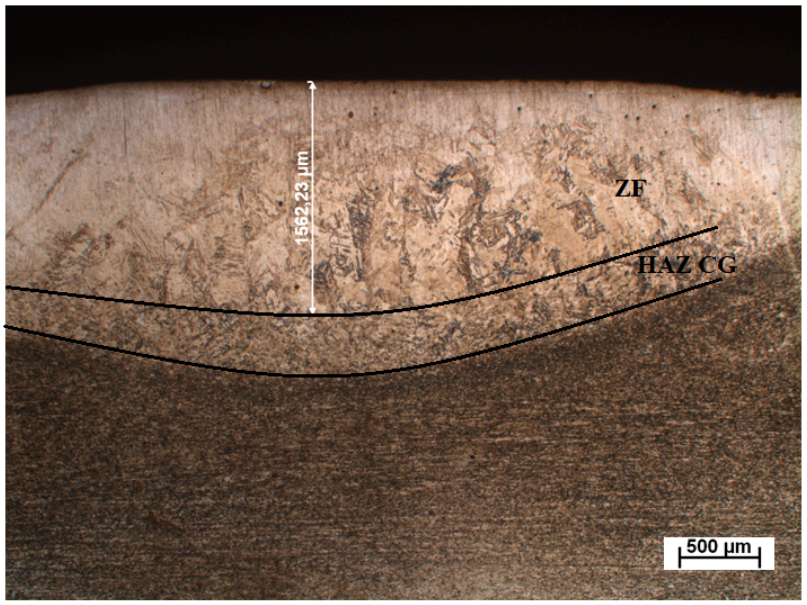

Source: The author (2025).

In the numerical stage, a volumetric heat source of the double ellipsoid type was used. The weld dimensions found in the experimental stage were used as input values in the

simulated power source dimension. The temperature distribution profile in the cross section of the weld bead is shown in Fig. 53(a) for 165A current and 54(b) for 216A current.

The microstructure of the fusion zone presents a dendritic morphology typical of solidification. Dendritic growth occurs in the direction of thermal extraction, with a columnar texture (preferential growth axis) near the HAZ. The structure is composed predominantly of solid alpha ferrite, since AISI 409 solidifies in the ferritic field. No austenite or martensite formation was observed, which is expected for this low-carbon ferritic steel.

The heat-affected zone is the intermediate region between the molten metal and the base metal. Figures 53 and 54 show this region. The growth of ferritic grains is visible, indicating that this region reached temperatures above 900 °C and below the melting point. The grain size distribution will vary depending on the distance from the fusion zone. The grains increase in size the closer they are to the fusion zone, due to the longer exposure time and temperature.

The base metal is shown in figures 53 and 54 at the top. The structure is ferritic homogeneous. Although this region was thermally affected by the welding energy, it maintained its property

Figure 53 – (a) Cross-section of the simulated weld bead for 165A current and (b) 216A current.

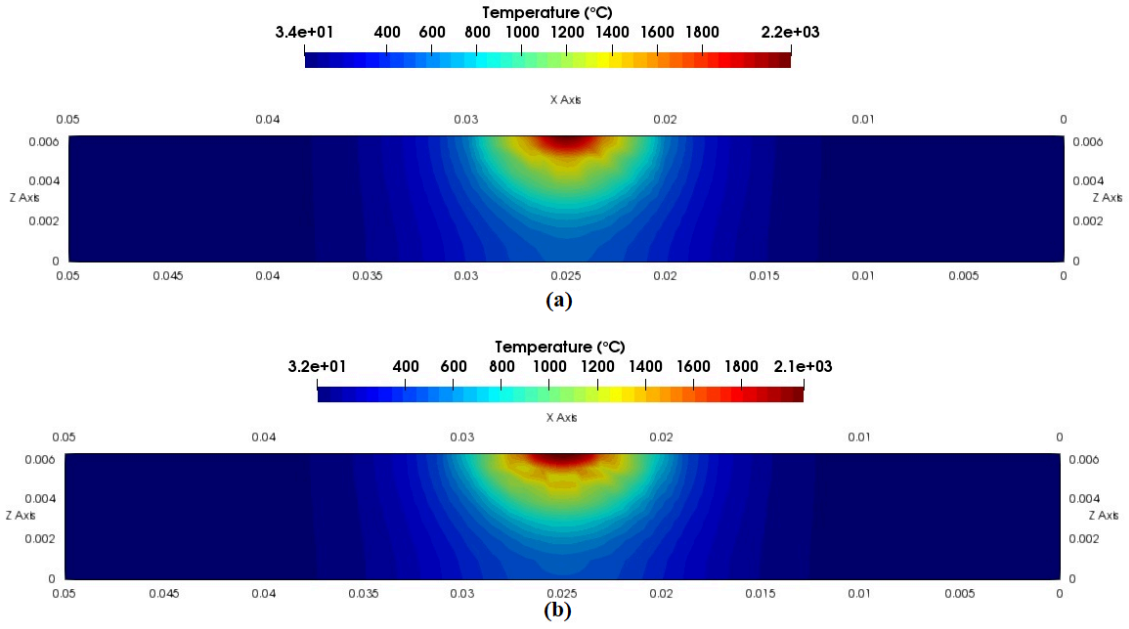

Source: The author (2025).

Fig. 54 shows a good agreement between the experimental and simulated zones.

Figure 54 – (a) Melt zone in AISI 409 ferritic steel (fusion zone, heat-affected zone, base metal). (b) Melt simulated zone (red – liquid, blue – solid and another color mush region).

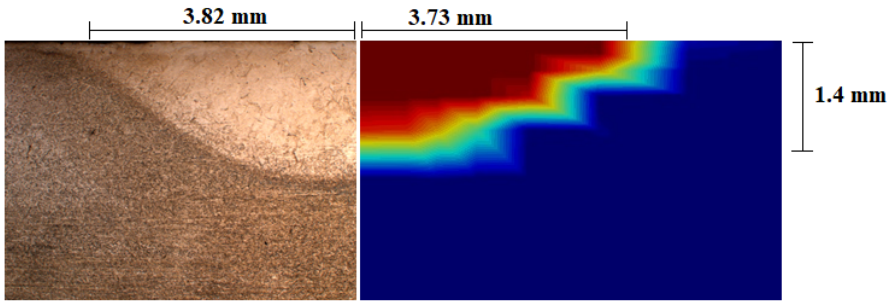

Source: The author (2025).

10.4 Welding thermal efficiency and weld bead shape.

The heat source must be adapted with data obtained approximately in the middle of the weld bead, a region in which the process has already reached a stabilized condition; the global heat input (more precisely the thermal efficiency) must be adjusted by adapting the thermal cycles to those measured by thermocouples at medium distances from the weld bead, in regions not affected by the radiation of the electric arc and which do not have very steep thermal gradients (58).

The thermal efficiency of a welding process was determined inversely, relating the thermal cycles obtained with those acquired from thermocouples, since it is not always possible to perform calorimetry tests to obtain this parameter (59). In some works, the efficiency value was adjusted for better comparison between experimental and computational results (60, 61). The welding efficiency value in some works is simply assumed by their authors without justification (62, 63, 64).

For other authors, the thermal efficiency of a welding process depends on the type of material, current, voltage, electrode-to-plate distance, electrode tip angle, polarity of the source terminal, among others (65, 31).

Thermal efficiency can be estimated directly through the use of calorimeters. The average amount of heat supplied to the welded body is measured throughout the welding process (67, 68). The use of calorimeters does not determine yield variations that may occur during the experimental welding process.

The efficiency value used in the numerical stage of this work was attributed due to the parameters used in the experimental process. The parameters analyzed that indicated the value used were: polarity of the welding source terminal, welding current value, distance from the electrode to the welded piece and angle of the electrode tip.

After evaluating the parameters in the experimental process, the thermal efficiency value was assigned as an input variable for the numerical process. Table 4 indicates the values and ranges of electric current that the tungsten electrode can withstand.

Table 4 – Current values for tungsten electrodes.

Electrode diameter (mm)	**Current (A) and polarity**					
	CC-	**CC+**	**CA Balanced**		**CA Unbalanced**	
	EWX-X	**EWX-X**	**EWP**	**EWP-X**	**EWP**	**EWX-X**
0,3	Até 15	-	Até 15	Até 12	Até 15	Até 15
0,5	5 - 20	-	10 - 20	5 - 20	5 - 15	5 - 20
1	15 - 80	-	20 - 60	15 - 80	10 - 30	20 - 60
1,6	70 - 150	10 - 20	50 - 100	70 - 150	30 - 80	60 - 120
2,4	150 - 250	15 - 30	100 - 160	140 - 235	60 - 130	100 - 180
3,2	250 - 400	25 - 40	150 - 200	225 - 325	100 - 180	160 - 250
4,0	400 - 500	40 - 55	200 - 275	300 - 400	160 - 240	200 - 320
4,8	500 - 750	55 - 80	250 - 350	400 - 500	190 - 300	290 - 390
6,4	750 - 1000	80 - 125	325 - 450	500 - 630	250 - 400	340 - 525

Fonte: (69).

The present work uses current values very close to the minimum current limit for each electrode. At the end of the four welding passes, the tip was visually analyzed to identify whether there was significant wear on the tip, sufficient to change the angle. Therefore, in the experiment that used low current and low wear on the electrode tip, it was established that for this experiment the thermal welding efficiency in the numerical simulation process would be 0,55.

Figs. 57 and 58 show images of the weld bead after a few passes. The weld beads did not suffer any deviation during the process. This reinforces an experiment under conditions of good welding arc stability.

Figure 55 – (a) AISI 409 steel part after the first welding pass with a current of 165A. (b) after the fourth welding pass.

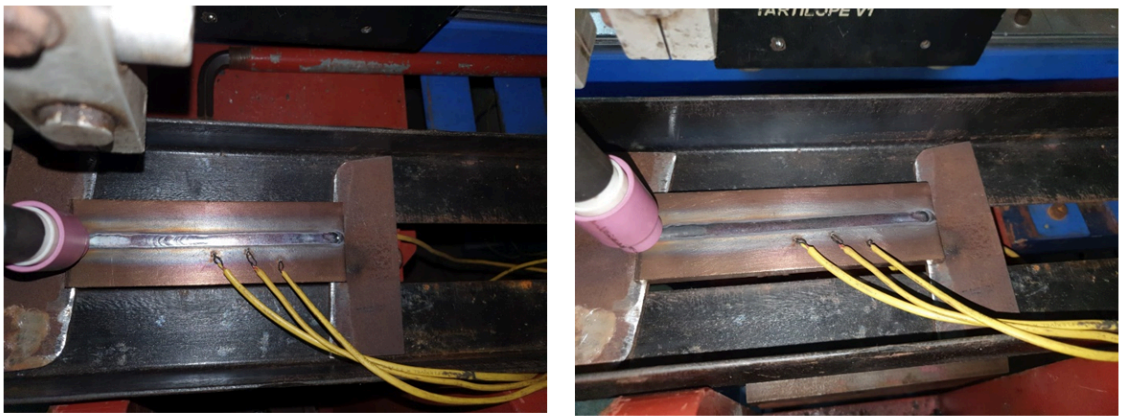

(a) (b)

Source: The author (2025).

Figure 56 – (a) AISI 409 steel part after the first welding pass with a current of 216A. (b) after the second welding pass. (c) after the third welding pass. (d) after the fourth welding pass.

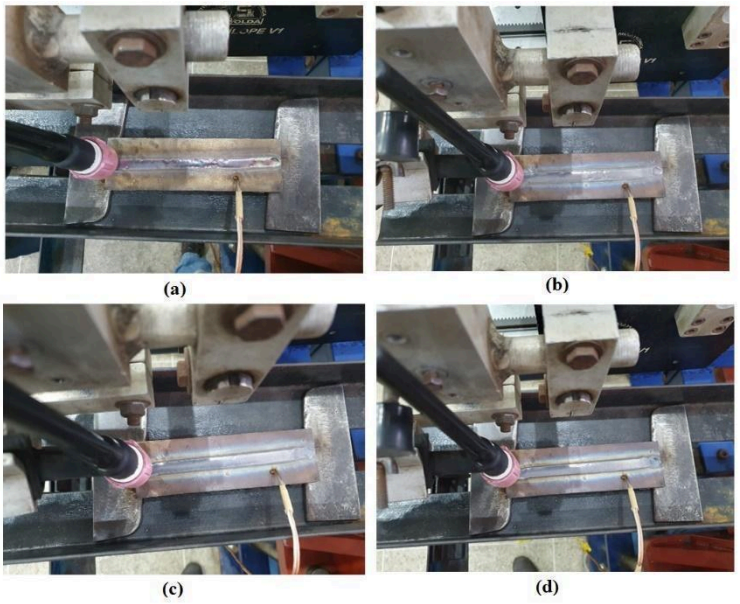

(a) (b)

(c) (d)

Source: The author (2025).

11 RESULTS

In this chapter, the results acquired from the experimental and numerical stage with four welding passes using the autogenous TIG process will be presented. The first section presents the study of three of the four thermal source models used in the numerical model. The second presents the experimental results of the thermal cycles in the AISI 409 steel sample with a current of 165A and the numerical results using the thermal source that best adjusted to the experimental results. In the third section, the experimental results of the thermal cycles on the AISI 409 steel sample with a current of 216A and the numerical results using the thermal source that best adjusted to the experimental results are presented.

11.1 Numerical results with different thermal source models.

Figs. 59(a), 59(b) and 59(c) present the results of the acquisition of experimental and numerical thermal cycles for thermocouples T4, fixed 80 mm from the initial position of the torch in a blind hole 2.96 mm deep from the base of the steel sample, T5 fixed at the base 100 mm from the initial position of the torch and T1 fixed at the top of the sample 80 mm from the initial position of the torch and perpendicular to the center of the weld bead 8 mm, respectively current of 165 A. For a better understanding of the position of the thermocouples, each thermocouple will be referenced by the coordinates (x = distance from the center of the bead, y = distance from the initial position of the torch, z = thickness, with the value zero indicating the base). Thus, we have: T1(8mm, 80mm, 6.3mm), T4(0mm, 80mm, 2.96mm), T5(0mm, 100mm, 0mm). The numerical results were obtained with a semi-ellipsoidal source model.

Figure 57 – Thermal cycles of the four experimental and numerical welding passes with a Semi-Ellipsoid source at the positions of thermocouples T4(a), T5(b) and T1(c).

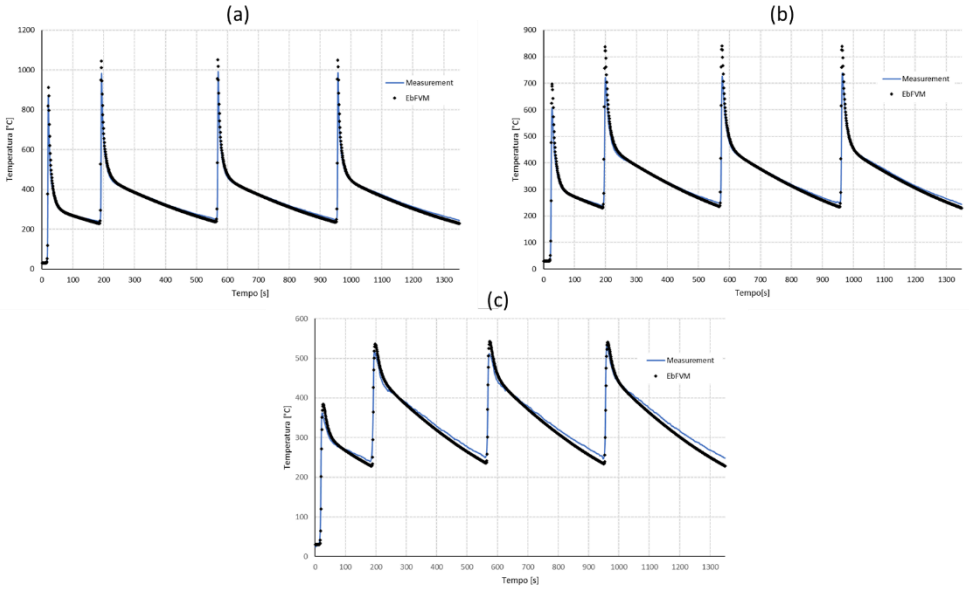

Source: The author (2025).

Figs. 60(a) and 60(b) present the results of the acquisition of the experimental and numerical thermal cycles of the thermocouples T6, fixed at 120 mm from the initial position of the torch in a blind hole of 2.92 mm depth from the base of the steel sample, i.e., T6(0mm, 120, 2.92mm) and T3 fixed at the top of the sample at 120 mm from the initial position of the torch and perpendicular to the center of the weld bead 13 mm, i.e., T3(13mm, 120mm, 6.3mm), respectively, for the welding experiment with 165A current.

Figure 58 – Thermal cycles of the four experimental and numerical welding passes with a Semi-Ellipsoid source at the positions of thermocouples T6(a) and T3(b).

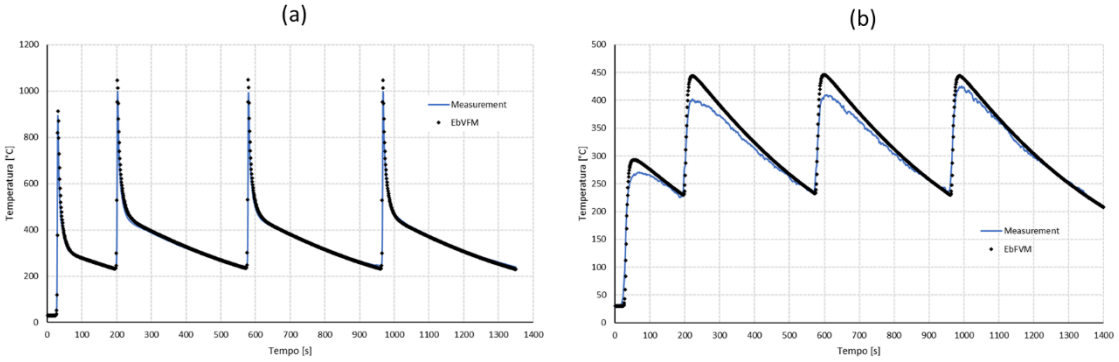

Source: The author (2025).

Figs. 61 (a), 61(b) and 61(c) present the results of the acquisition of experimental and numerical thermal cycles for thermocouples T4(0mm, 80mm, 2.96mm), T5(0mm, 100mm, 0mm) and T1(8mm, 80mm, 6.3mm), respectively, for the welding experiment with a current of 165A. For the numerical stage, the source used was a double ellipse model.

Figure 59 – Thermal cycles of the four experimental and numerical welding passes with double ellipse source at the positions of thermocouples T4(a), T5(b) and T1(c).

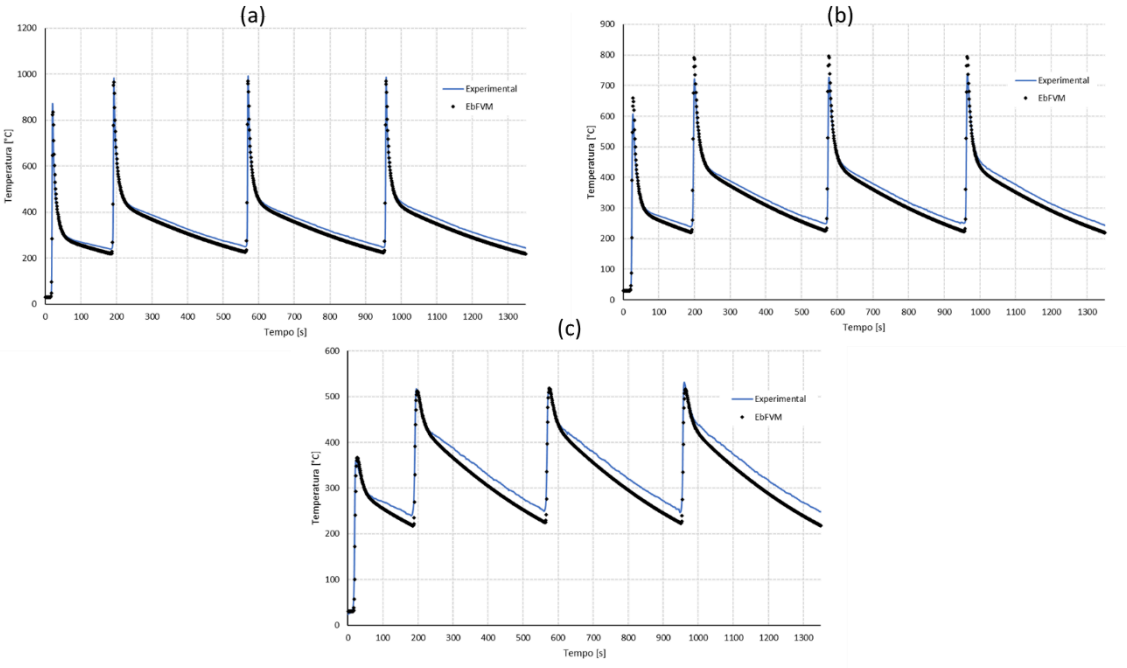

Source: The author (2025).

Figs. 62(a) and 62(b) present the results of the acquisition of the experimental and numerical thermal cycles of the thermocouples T6(0mm, 120mm, 2.92mm) and T3(13mm, 120mm, 6.3mm), respectively, for the welding experiment with a current of 165A.

Figure 60 – Thermal cycles of the four experimental and numerical welding passes with double ellipse source at the positions of thermocouples T6(a) and T3(b).

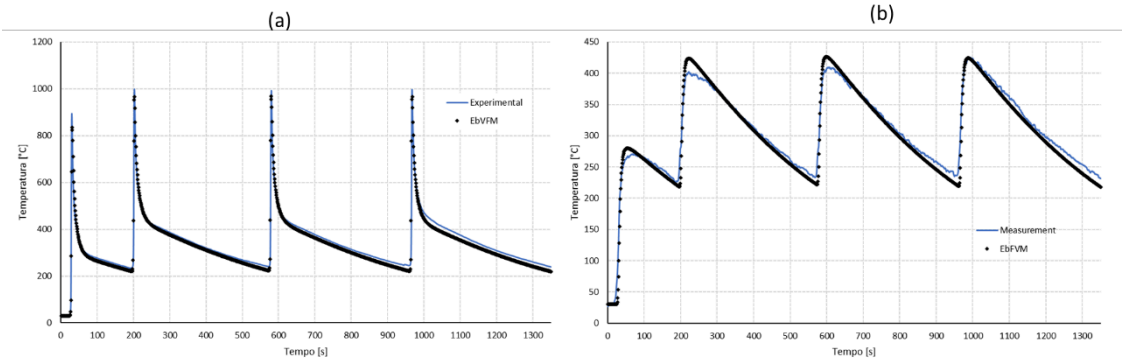

Source: The author (2025).

Figs. 63(a), 63(b) and 63(c) present the results of the acquisition of experimental and numerical thermal cycles for thermocouples T4(0mm, 80mm, 2.96mm), T5(0mm, 100mm, 0mm) and T1(8mm, 80mm, 6.3mm), respectively, for the welding experiment with a current of 165A. For the numerical stage, the source used was a circular model.

Figure 61 – Thermal cycles of the four experimental and numerical welding passes with circular source at the positions of thermocouples T4(a), T5(b) and T1(c).

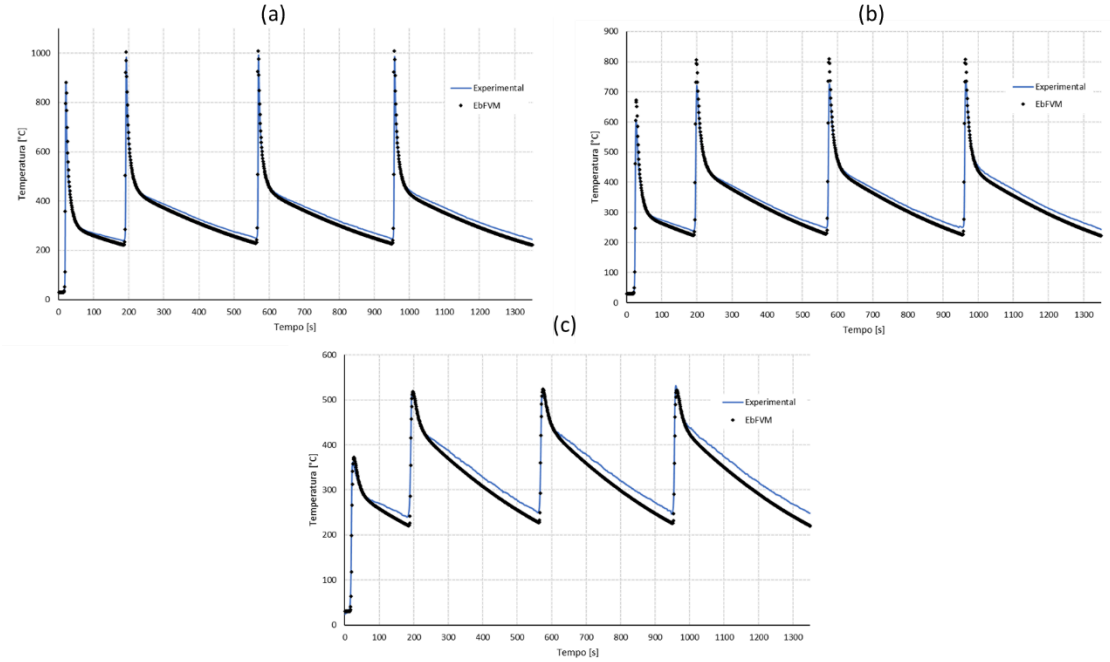

Source: The author (2025).

Figs. 64(a) and 64(b) present the results of the acquisition of the experimental and numerical thermal cycles of the thermocouples T6(0mm, 120mm, 2.92mm) and T3(13mm, 120mm, 6.3mm), respectively, for the welding experiment with a current of 165A.

Figure 62 – Thermal cycles of the four experimental and numerical welding passes with circular source at the positions of thermocouples T6(a) and T3(b).

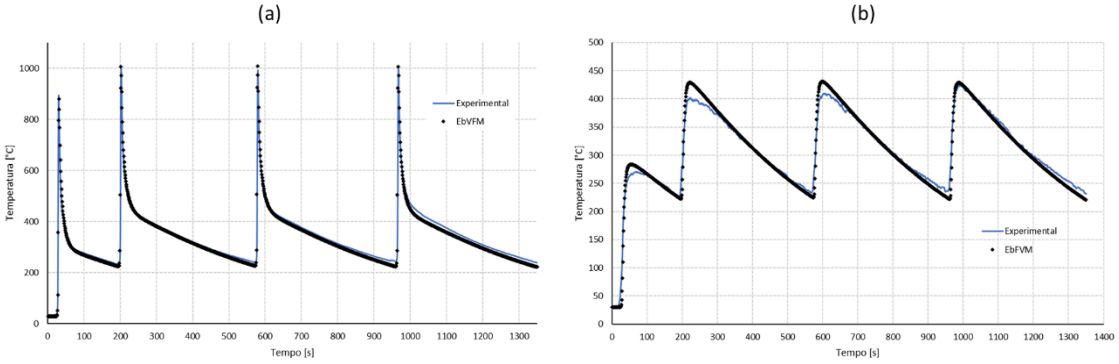

Source: The author (2025).

In a general analysis, the three heat sources presented in Figs. 59 to 64 presented very similar results for the temperature peaks. For the cooling stage, some discrepancies were found when comparing the numerical results with the experimental ones. The dual ellipsoid model source showed overall better agreement with experimental data for peak temperature and cooling profiles. Therefore, the double ellipsoid source was chosen for the simulations with the two welding currents. The results obtained experimentally and numerically, using the double ellipsoid source model with currents of 165 A and 216 A, will be detailed in sections 11.2 and 11.3 of this work.

Fig. 65(a) shows the image of the base of the ferritic stainless steel 409 sample during the autogenous TIG welding process. The movement of the torch allows the shape of the heat propagation in the steel sample to resemble the design of a double ellipsoid. The color variation in Fig. 65(a) makes it clear that the central region of the heat distribution has a higher temperature intensity. The decrease in color intensity around the source indicates a reduction in the temperature value. Fig. 65(b) shows the shape of the source, a double ellipsoid, in the simulated plane. The thermometric scale on the side shows the temperature variation. The simulated source has good agreement with the shape of the source in the real welding process.

Figure 63 – (a) shows the underside of the plate at the time of autogenous TIG welding with a current of 216A. (b) the base of the plate simulated with a current of 216A.

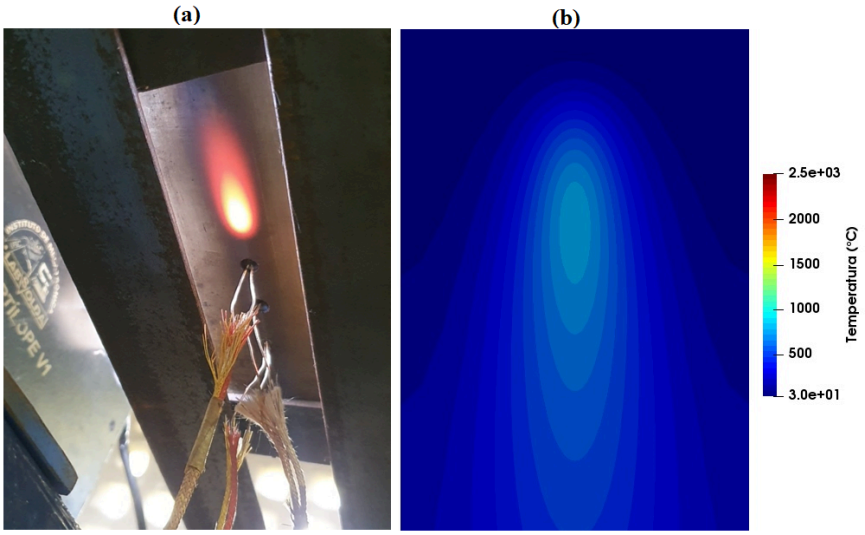

Source: The author (2025).

11.2 Experimental and numerical results, using double ellipsoid source, for AISI 409 steel and average welding current of 165A.

Fig. 66 presents the results of the experimental and numerical thermal cycles of the four welding passes for the thermocouple in position T4, in a blind hole 2.96 mm deep from the base. This thermocouple is 80 mm from the initial torch movement position and is in the same line as the weld bead, see Fig. 43.

Figure 64 – Thermal cycle of the four welding passes with acquisition in the experimental and numerical T4 thermocouple using a double ellipsoid source.

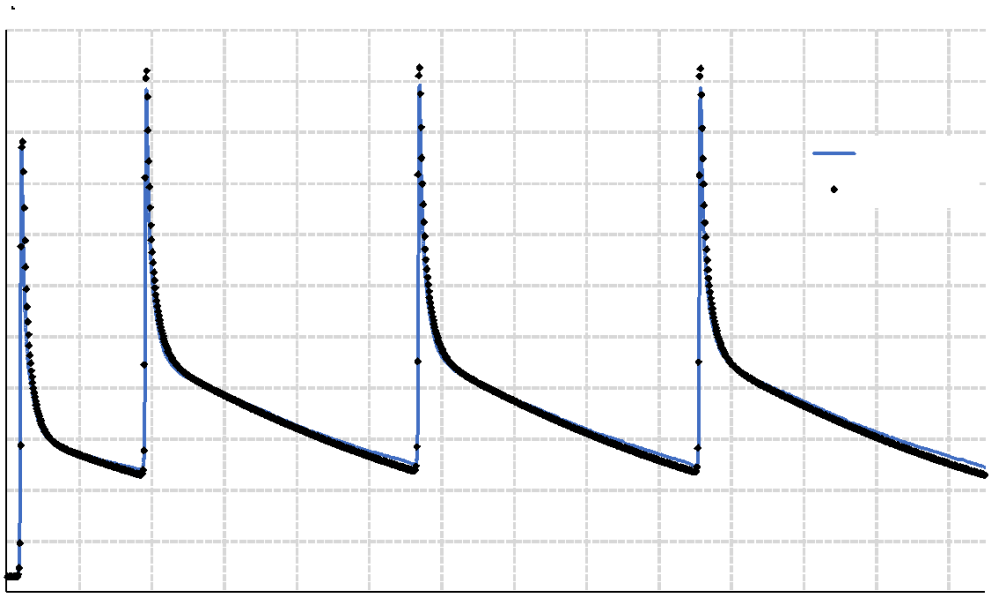

Source: The author (2025).

Heating in the thermocouple T4 (0mm, 80mm, 2.96mm) for the first welding pass occurs between the time interval of 15s and 20.74s, reaching maximum temperature at t = 20.74s for the experimental process. In the numerical stage, heating occurs between the time interval of 15s to 21s, reaching peak temperature at t = 21s. The interval between the peaks of the last three passes is a sum of the torch travel time and the local cooling time of thermocouple T4 until thermocouple T5 (0mm, 100m, 0mm), located at the base of the part, reaches the inter-pass temperature of 250 °C.

For the first welding pass, the dwell time at a temperature of 500 °C is 7.88 s for the experimental and approximately 10.5 s for the numerical. The cooling time from 800 °C to 500 °C is 5.46 s for the experimental one and approximately 6 s for the numerical one, as shown in Fig. 67. The cooling time from 800 °C to 300 °C is 34.7 s for the experimental one and approximately 36 s for the numerical one, as shown in Fig. 67.

The highest heating and cooling rate values for the experimental process occurred at t = 19.2 s and t = 21.56 s, respectively. The highest heating and cooling rate values for the numerical process occurred at t = 18 s and t = 22 s, respectively, as shown in Fig. 67.

Figure 65 – Thermal Cycle and Rate of Temperature Change for First Pass Thermocouple T4.

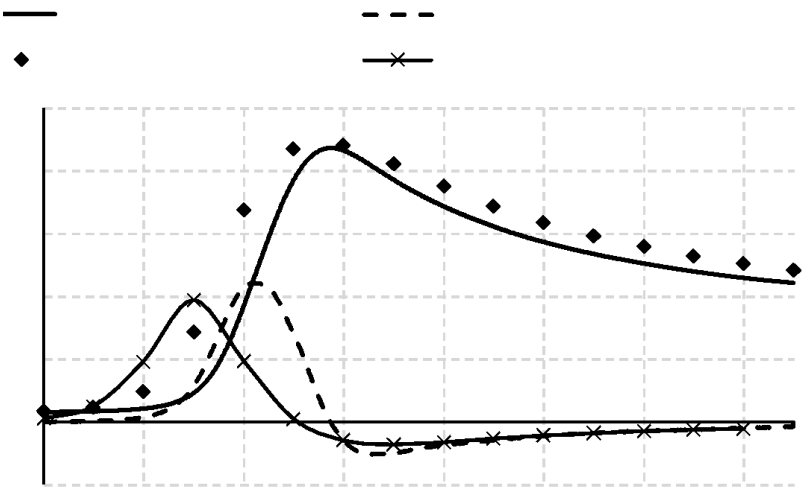

Source: The author (2025).

In the second welding pass, heating occurs between the time interval of 189s to 193.12s, reaching a peak temperature at t = 193.12s for the experimental process. In the numerical stage, heating occurs between the time interval of 189s to 193s, reaching peak temperature at t=193s. The dwell time at a temperature of 500 °C for the second welding pass is 20.68s for the experimental and approximately 24s for the numerical. Cooling from 800 °C to 500 °C takes 16.56s for the experimental and approximately 17s for the numerical, as shown in Fig. 68. Cooling from 800 °C to 300 °C takes 253.88s for the experimental and approximately 239s for the numerical, as shown in Fig. 67.

The largest heating and cooling rate values for the experimental process occurred at t = 192.76s and t = 194.08s, respectively. The largest heating and cooling rate values for the numerical process occurred at approximately t = 191s and t = 194s, respectively, as shown in Fig. 68.

Figure 66 – Thermal Cycle and Rate of Temperature Change for the Second Pass T4 Thermocouple.

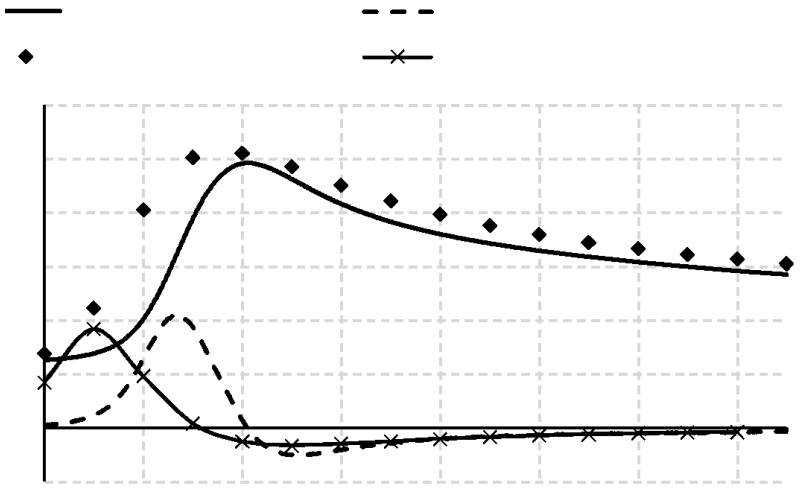

Source: The author (2025).

In the third welding pass, heating occurs between the time interval of 563s to 570.14s, reaching peak temperature at t = 570.14s for the experimental process. In the numerical stage, heating occurs between the time interval 563s to 570s, reaching peak temperature at t = 570s. The residence time for the temperature of 500 °C for the third weld pass is 21.8 s for the experimental and approximately 27 s for the numerical. The cooling from 800 °C to 500 °C has a duration of 17.56 s for the experimental and approximately 20 s for the numerical, as shown in Fig. 69. The cooling from 800 °C to 300 °C has a duration of 265.34 s for the experimental and approximately 246 s for the numerical, as shown in Fig. 67.

The highest heating and cooling rate values for the experimental process occurred at t = 568.76s and t = 571.18s, respectively. The highest values of heating and cooling rates for the numerical process occurred, approximately, at t = 567s and t = 571s, respectively, as shown in Fig. 69.

Figure 67 – Thermal Cycle and Rate of Temperature Change for the Third Pass T4 Thermocouple.

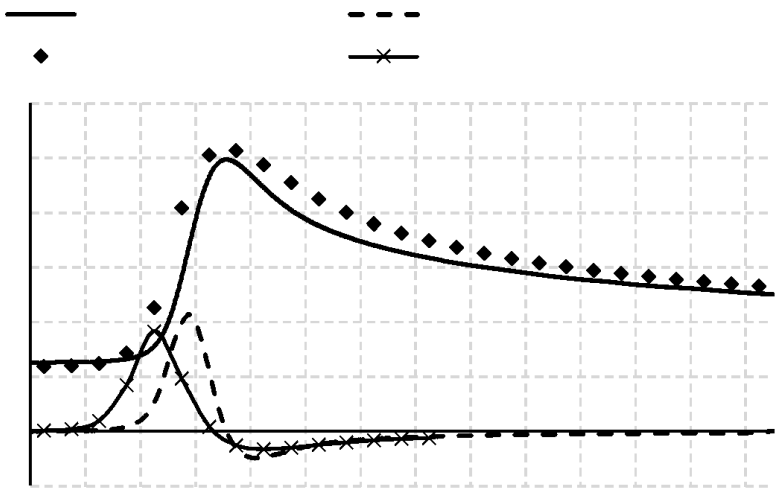

Source: The author (2025).

In the fourth welding pass, heating occurs between the time interval of 953s to 957.96s, reaching peak temperature at t = 957.96s for the experimental process. In the numerical stage, heating occurs between the time interval of 953s to 958s, reaching peak temperature at t = 958s. The dwell time at the temperature of 500 °C for the fourth welding pass is 22.38 s for the experimental and 27 s for the numerical. The cooling from 800 °C to 500 °C has a duration of 18.12 s for the experimental and 20 s for the numerical, as shown in Fig. 70. Cooling from 800 °C to 300 °C takes 265.64 s for the experimental and 243 s for the numerical, as shown in Fig. 67.

The largest heating and cooling rate values for the experimental process occurred at t = 956.48 s and t = 958.86 s, respectively. The largest heating and cooling rate values for the numerical process occurred at approximately t = 955 s and t = 959 s, respectively, as shown in Fig. 70.

Figure 68 – Thermal Cycle and Rate of Temperature Change for Fourth Pass Thermocouple T4.

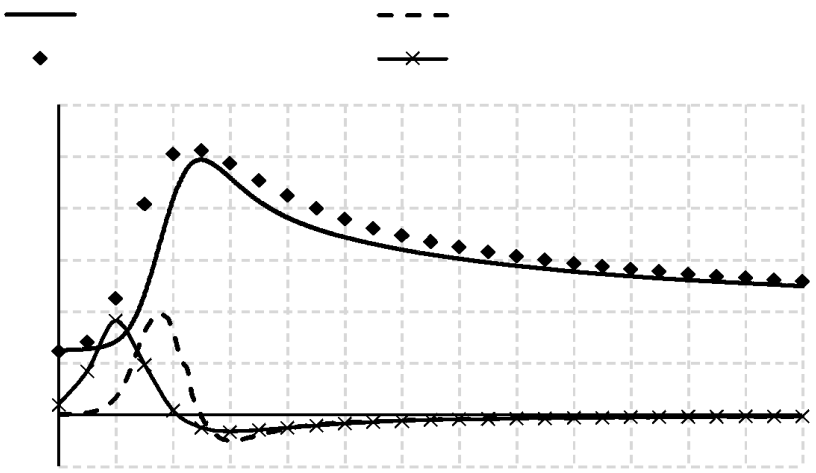

Source: The author (2025).

Table 5 shows the degree of agreement between the experimental and numerical temperature peaks for thermocouple T4.

Table 5 – Percentage error between experimental and simulated peak temperature values for thermocouple T4.

Temperatura (°C)	1 ° Passe	2° Passe	3° Passe	4° Passe
Experimental	872,13	983,5	992,46	986,23
EbFVM	880,64	1019,76	1025,44	1024,02
Erro percentual (%)	0,97	3,68	3,32	3,83

Source: The author (2025).

For the thermocouple T4 (0mm, 80mm, 2.96mm), the experimental results showed almost zero noise rate. The experimental values for the peak temperatures, presented in Tab. 4, and heating and cooling profile were in agreement with the numerical results. The average percentage error for the total simulation time was 4,23%. The heating and cooling rate values were slightly similar when comparing the experimental results with the numerical results. Anisotropic factors of the thermal conductivity of the material in the autogenous TIG welding process stage was not perceived in the numerical simulation process that uses thermal conductivity with isotropic formalism.

Fig. 71 presents the results of the acquisition of the experimental and simulated thermal cycle of the four welding passes for the thermocouple in position T5 located at the base of the sample and 100 mm from the beginning of the torch path below the weld bead line, see Fig. 43.

Figure 69 – Thermal cycle of the four welding passes with acquisition in the experimental and numerical T5 thermocouple using a double ellipsoid source.

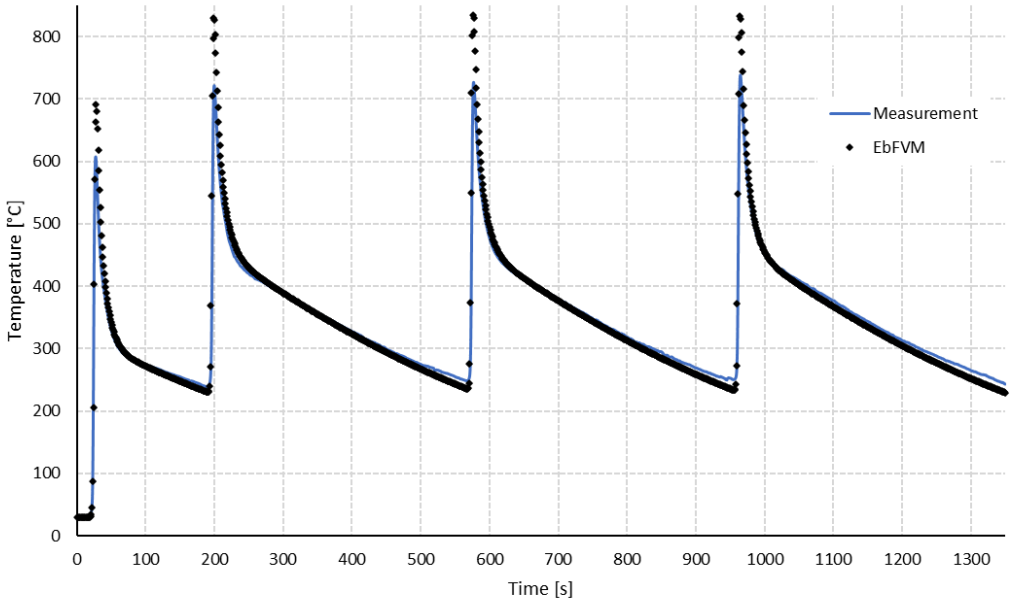

Source: The author (2025).

Heating in the T5 thermocouple for the first welding pass occurs between the time interval of 22s to 27.34s, reaching the maximum temperature at t = 27.34s for the experimental process. In the numerical stage, heating occurs between the time interval of 21s to 27s, reaching the peak temperature at t = 27s. The interval between the peaks of the last three passes is a sum of the torch travel time and the local cooling time until the T5 thermocouple reaches the inter-pass temperature of 250 °C.

For the first weld pass, the dwell time at the 500 °C temperature is 6.22 s for the experimental process and approximately 9 s for the numerical one. The cooling time from the peak temperature to 500 °C is 4 s. Since the numerical process has a higher peak temperature, its duration to reach the temperature of 500°C is 7s, as shown in Fig. 72. The cooling time

from 600 °C to 300 °C is 33s in the experimental process. In the numerical process the cooling time from the peak temperature to 300 °C is 36s, as shown in Fig. 71.

The highest heating and cooling rate values for the experimental process occurred at t = 24.4 s and t = 28.96 s, respectively. The highest heating and cooling rate values for the numerical process occurred at t = 23 s and t = 29 s, as shown in Fig. 71.

Figure 70 – Thermal Cycle and Rate of Temperature Change for First Pass T5 Thermocouple.

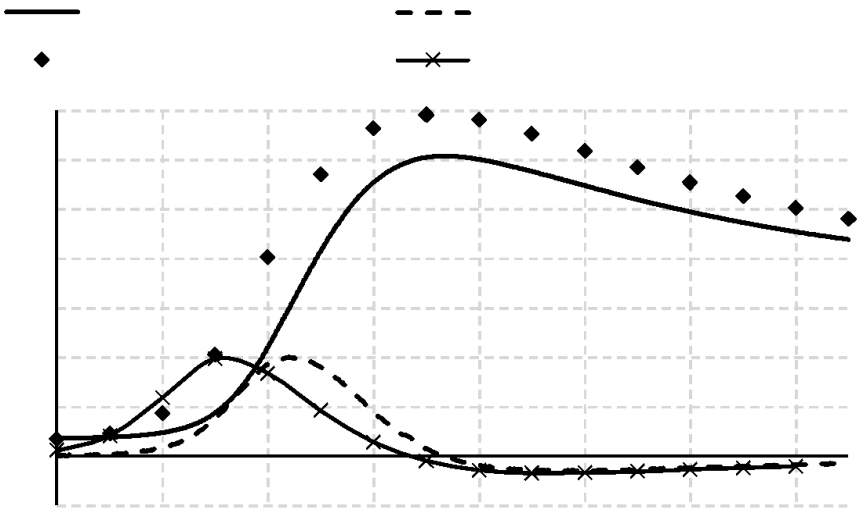

Source: The author (2025).

In the second welding pass, heating occurs between the time interval 193s to 199.74s and the peak temperature is reached at t = 199.74s for the experimental process. In the numerical stage, heating occurs between the time interval 193s to 199s with peak temperature at t = 199s. The dwell time at a temperature of 500 °C for the second welding pass is 20s for the experimental method and approximately 26s for the numerical method, as shown in Fig. 73. The cooling from 721.43 °C to 500 °C takes 16.82s for the experimental stage. The cooling from the peak temperature to 500 °C in the numerical stage is 22s, as shown in Fig. 73. The cooling from 721.43 °C to 300 °C takes 249.8s for the experimental stage. In the numerical stage the cooling time from the peak temperature to 300 °C is approximately 240s, as shown in Fig. 71.

The highest heating and cooling rate values for the experimental process occurred at t = 197.06 s and t = 201.82 s, respectively. The highest heating and cooling rate values for the numerical process occurred at approximately t = 195 s and t = 202 s, as shown in Fig. 73.

Figure 71 – Thermal Cycle and Rate of Temperature Change for the T5 Second Pass Thermocouple.

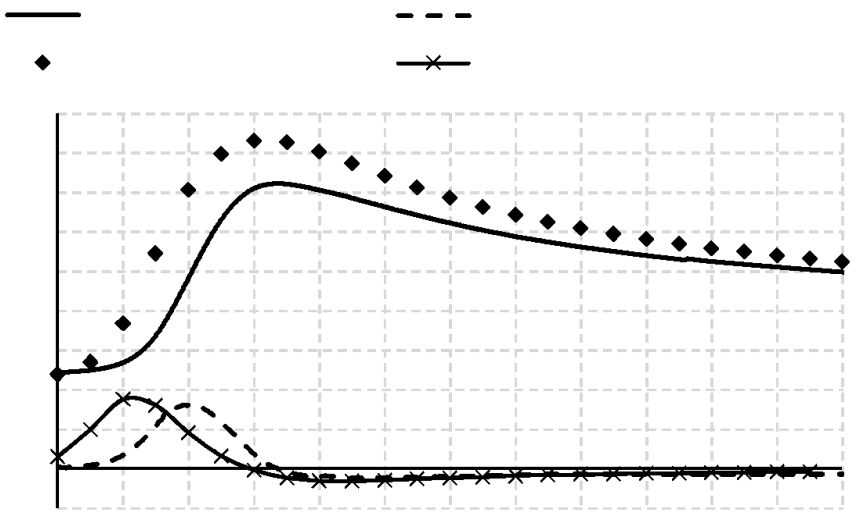

Source: The author (2025).

In the third welding pass, heating occurs between the time interval of 569s to 576.88s, reaching peak temperature at t = 576.88s for the experimental process. In the numerical stage, heating occurs between the time interval of 569s to 576s, reaching peak temperature at t = 576s. The dwell time for the temperature of 500 °C for the third welding pass is 20.88 s for the experimental and approximately 25s for the numerical. Cooling from the peak temperature to 500 °C takes 18.18s for the experimental and approximately 22s, as shown in Fig. 74. Cooling from the peak temperature to 300 °C takes 259.88s for the experimental process and 246s for the numerical one, as shown in Fig. 71.

The highest heating and cooling rate values for the experimental process occurred at t = 574s and t = 580.64s, respectively. The highest heating and cooling rate values for the numerical process occurred at approximately t = 572s and t = 579s, as shown in Fig. 71.

Figure 72 – Thermal Cycle and Rate of Temperature Change for the Third Pass T5 Thermocouple.

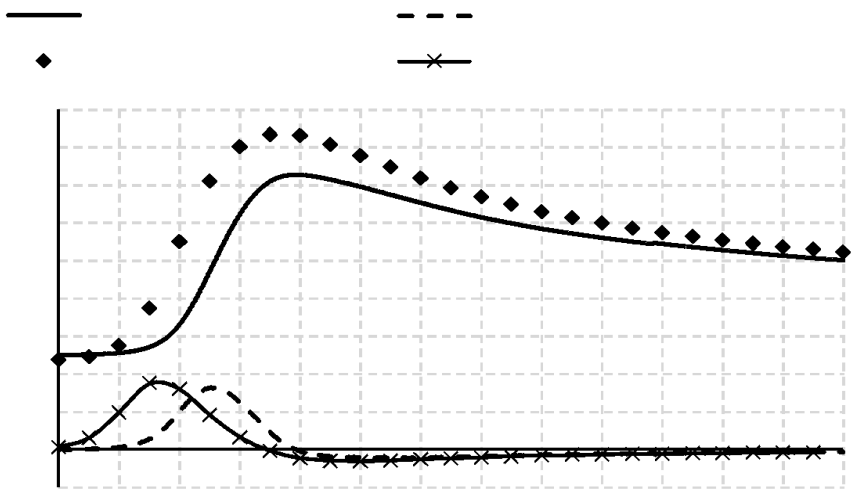

Source: The author (2025).

In the fourth welding pass, heating occurs between the time interval of 957s to 964.8s, reaching a peak temperature at t = 964.8s for the experimental process. In the numerical stage, heating occurs between the time interval 957s to 964s reaching peak temperature at t = 964s. The dwell time at a temperature of 500 °C for the fourth welding pass is 22.08s for the experimental and approximately 25s for the numerical. The cooling from the peak temperature to 500 °C has a duration of 19.2s for the experimental and 21 s for the numerical, as shown in Fig. 75. The cooling from the peak temperature to 300 °C has a duration of 260.6s for the experimental and 243s for the numerical, as shown in Fig. 71.

The highest heating and cooling rate values for the experimental process occurred at t = 962.1s and t = 967.28s, respectively. The highest heating and cooling rate values for the numerical process occurred approximately at t = 960s and t = 967s, as shown in Fig. 75.

Figure 73 – Thermal Cycle and Rate of Temperature Change for Fourth Pass T5 Thermocouple.

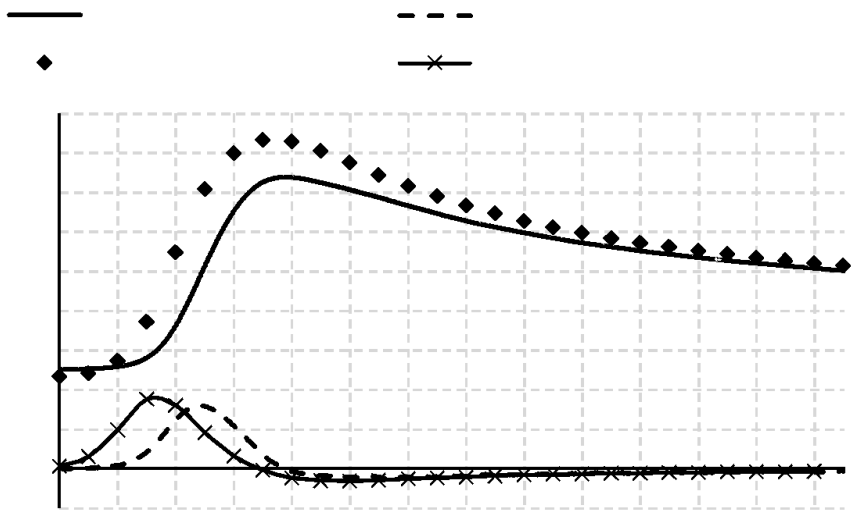

Source: The author (2025).

Table 6 shows the degree of agreement between the experimental and simulated temperature peaks for thermocouple T5.

Table 6 – Percentage error between experimental and simulated peak temperature values for thermocouple T5.

Temperature (°C)	1 ° Pass	2° Pass	3° Pass	4° Pass
Experimental	607,36	721,49	726,7	738,2
EbFVM	691,09	829,92	833,83	832,18
Percentage error (%)	13,78	15,02	14,74	12,73

Source: The author (2025).

For the thermocouple T5(0mm, 100m, 0mm), the experimental results showed almost zero noise rate. The experimental peak values were divergent. The average percentage error for the total simulation time was 3,76%. The anisotropic factor of the thermal conductivity of the material in the autogenous TIG welding process stage was perceived in the numerical simulation process that uses thermal conductivity with isotropic formalism. The heating and cooling profile were in agreement when compared to the numerical results. The heating and cooling rate values were in agreement when comparing the experimental results with the numerical results.

Fig. 76 presents the results of the acquisition of the experimental and numerical thermal cycle of the four welding passes for the thermocouple in position T1 at the top of the sample and 80 mm from the beginning of the part. This thermocouple is located 8 mm away from the weld bead in the perpendicular direction, see Fig. 42.

Figure 74 – Thermal cycle of the four welding passes with acquisition in the experimental and numerical T1 thermocouple using a double ellipsoid source.

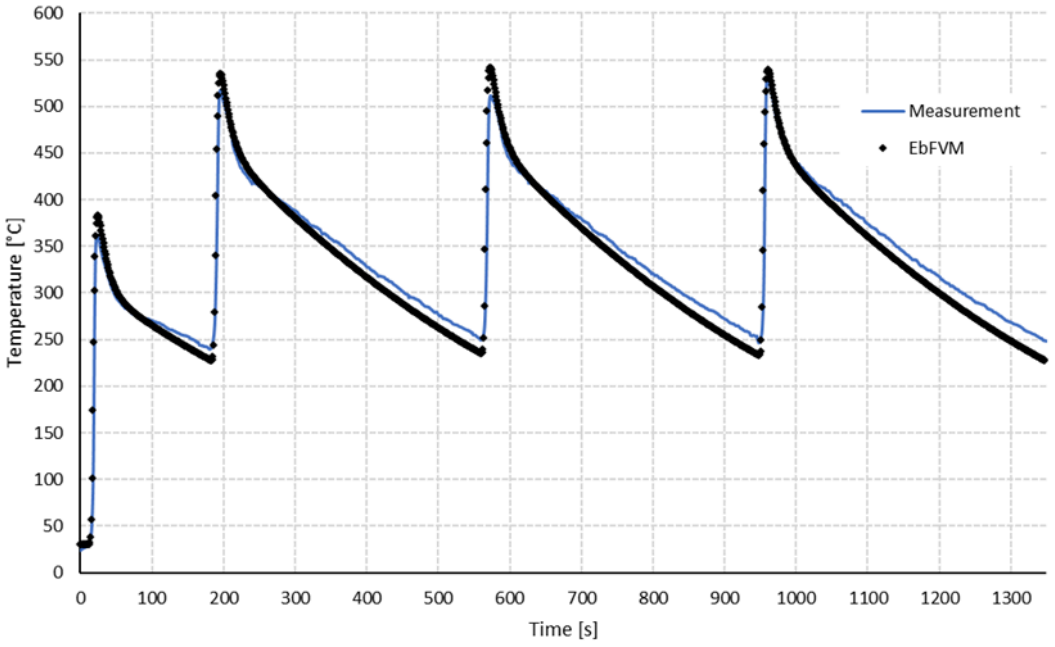

Source: The author (2025).

Heating in thermocouple T1 (8mm, 80mm, 6.3mm) for the first welding pass occurs between the time interval of 16s and 23.46s, reaching maximum temperature at t = 23.46s for the experimental. In the numerical stage, heating occurs between the time interval of 15s to 24s, reaching peak temperature at t = 24s. The interval between the peaks of the last three passes is a sum of the torch travel time and the local cooling time until the T5 thermocouple reaches the inter-pass temperature of 250 °C.

For the first welding pass, the thermocouple fixed in position T1 did not reach a temperature of 500°C and the numerical process was in agreement with the experimental process. The cooling time from the peak temperature to 300 °C is 19.48 s for the experimental process and 27 s for the numerical one, as shown in Fig. 77.

The highest heating and cooling rate values for the experimental process occurred at t = 19.1s and t = 26.76s, respectively. The largest heating and cooling values for the numerical process occurred at t = 16s and t = 29s, as shown in Fig. 77.

Figure 75 – Thermal Cycle and Rate of Change of Temperature for Thermocouple T1 First Pass.

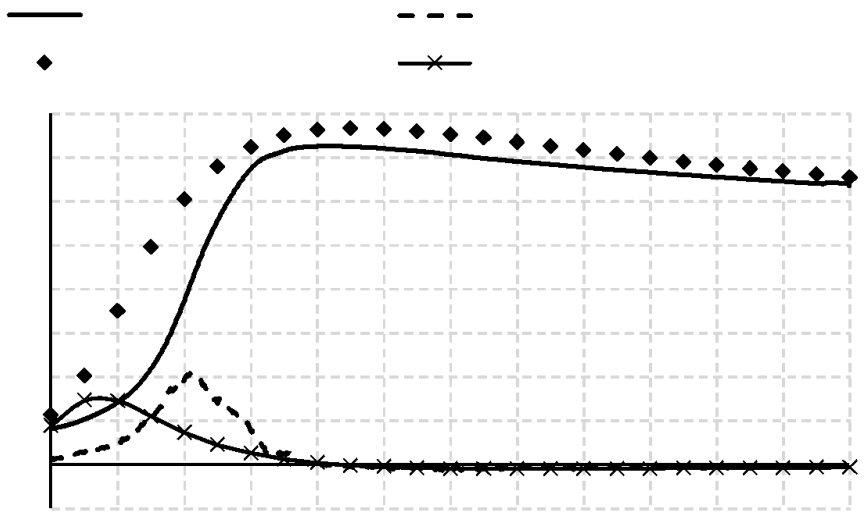

Source: The author (2025).

In the second welding pass, heating occurs between the time interval of 185s to 195.36s, reaching a peak temperature at t = 195.36s for the experimental process. In the numerical stage, heating occurs between the time interval of 185s to 195s, reaching a peak temperature at t = 195s. The time the temperature remains at 500 °C for the second welding pass is 8.36s for the experimental stage and approximately 13s for the numerical stage. Cooling from 517.34 °C to 500 °C takes 6.52 s for the experimental one and from 535.53 °C to 500 °C takes approximately 11 s, as shown in Fig. 78. The cooling time from 516.66 °C to 300 °C is 257 s for the experimental one and for the numerical one from 535.53 °C to 300 °C it is 234 s, as shown in Fig. 78.

The largest heating and cooling rate values for the experimental process occurred at t = 192s and t = 199s, respectively. The largest heating and cooling rates for the numerical process occurred at t = 190s and t = 199s, as shown in Fig. 78.

Figure 76 – Thermal cycle and rate of temperature change for thermocouple T1 second pass.

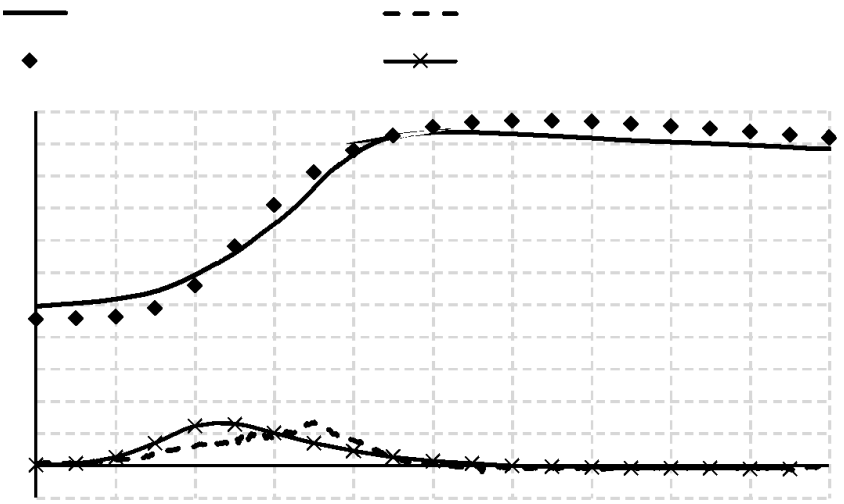

Source – The author (2025).

In the third welding pass, heating occurs between the time interval of 563s to 573s reaching the peak temperature at t = 573s for the experimental process. In the numerical stage, heating occurs between the time interval of 563s to 574s reaching the peak temperature at t = 574s. The dwell time for the temperature of 500 °C for the third welding pass is 9 s for the experimental and approximately 14 s for the numerical. The cooling from the experimental peak temperature to 500 °C lasts 7 s and the duration from the peak temperature of the numerical step to 500 °C is 10 s, as shown in Fig. 79. The cooling from the peak temperatures of the experimental and numerical to the temperature of 300 °C is 266 s and 240 s, respectively, as shown in Fig. 76.

The largest heating and cooling rate values for the experimental process occurred at t = 569 s and t = 581 s, respectively. The largest heating and cooling rates for the numerical process occurred at t = 566 s and t = 579 s, as shown in Fig. 76.

Figure 77 – Thermal Cycle and Rate of Temperature Change for Third Pass Thermocouple T1.

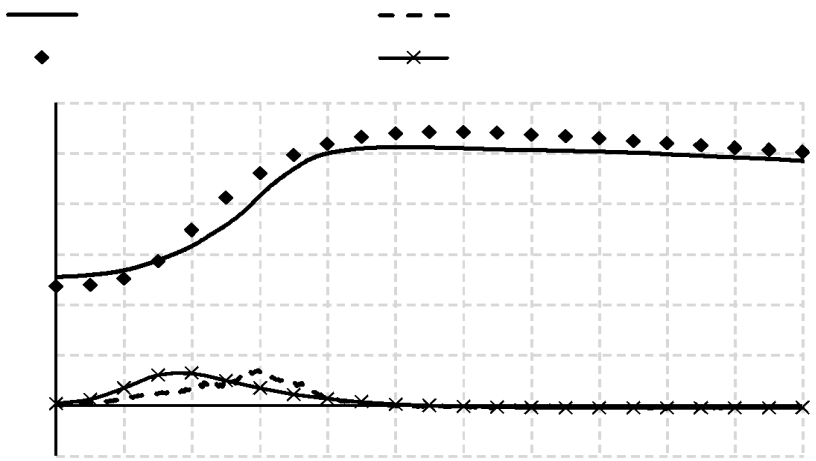

Source: The author (2025).

In the fourth welding pass, heating occurred between the time interval of 952s to 960.12s, reaching a peak temperature at t = 960.12s for the experimental process. In the numerical stage, heating occurred between the time interval of 952s to 962s, reaching a peak temperature at t = 962s. The residence time for the temperature of 500 °C for the fourth welding pass is 10s for the experimental stage and 12s for the numerical stage. The cooling time from the experimental and numerical peak temperature to 500 °C takes 8 s and 10 s, respectively, as shown in Fig. 80. The cooling time from the experimental and numerical peak temperature to 300 °C is 272 s and 242 s, respectively, as shown in Fig. 76.

Figure 78 – Thermal Cycle and Rate of Temperature Change for Fourth Pass Thermocouple T1.

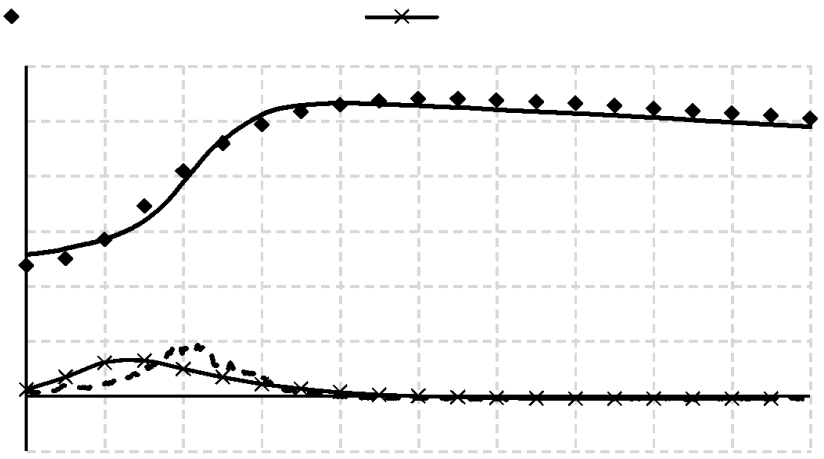

Source: The author (2025).

Table 7 shows the degree of agreement between the experimental and simulated temperature peaks for thermocouple T1.

Table 7 – Percentage error between experimental and simulated peak temperature values for thermocouple T1

Temperatura (°C)	1 ° Passe	2° Passe	3° Passe	4° Passe
Experimental	361,94	516,66	511,65	531,62
EbFVM	383,04	535,53	541,54	540,04
Erro percentual (%)	5,83	3,65	5,84	1,58

Source: The author (2025).

For thermocouple T1 (8mm, 80mm, 6.3mm), located at the top of the part and close to the torch, the experimental results showed a slight noise rate. The experimental peak values and heating and cooling profile were slightly divergent when compared to the numerical results. The average percentage error for the total simulation time was 4%. The heating and cooling rate values showed agreement when comparing the experimental results with the numerical results. Anisotropic factors of the thermal conductivity of the material in the autogenous TIG welding process stage was perceived in the numerical simulation process that uses thermal conductivity with isotropic formalism, which we attribute to the divergence between the experimental and numerical results.

Fig. 81 presents the results of the experimental and numerical thermal cycle acquisition of the four welding passes for the thermocouple at position T6 in a blind hole 2.92 mm from the base. This thermocouple is 120 mm from the initial torch movement position and is in line with the weld bead, see Fig. 43.

Figure 79 – Thermal cycle with experimental and simulated T6 acquisition using a double ellipsoid source.

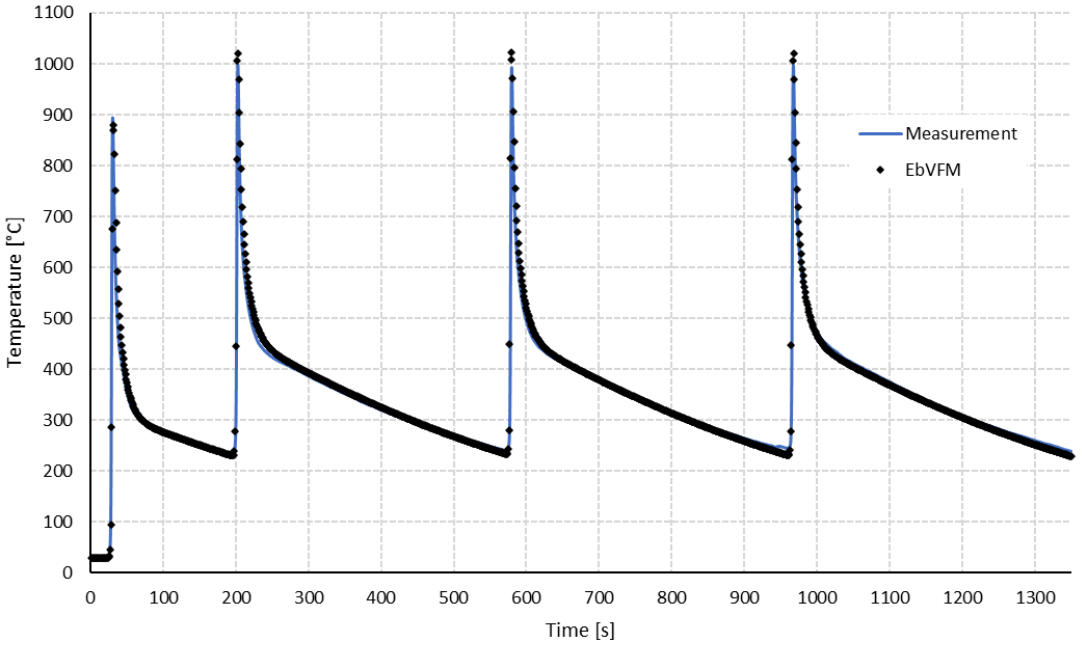

Source: The author (2025).

Heating in the thermocouple T6(0mm, 120mm, 2.92mm) for the first welding pass occurs between the time interval of 19s and 30.44s, reaching maximum temperature at t = 30.44s for the experimental process. In the numerical stage, heating occurs between the time interval of 20s to 31s, reaching peak temperature at t = 31s. The interval between the peaks of the last three passes is a sum of the torch travel time and the local cooling time until the thermocouple T5, located at the base of the part, reaches the inter-pass temperature of 250 °C.

For the first weld pass, the dwell time at a temperature of 500 °C is 6.42 s for the experimental and approximately 9 s for the numerical. The cooling time from 800 °C to 500 °C is 5.3 s for the experimental one and approximately 6 s for the numerical one, as shown in Fig. 82. The cooling time from 800 °C to 300 °C is 36,06 s for the experimental one and approximately 37 s for the numerical one, as shown in Fig. 81.

The highest heating and cooling rate values for the experimental process occurred at t = 28,84s and t = 31,3s, respectively. The highest heating and cooling rate values for the numerical process occurred at t = 28s and t = 32s, as shown in Fig. 82.

Figure 80 – Thermal cycle and rate of temperature change for the T6 thermocouple in the first pass.

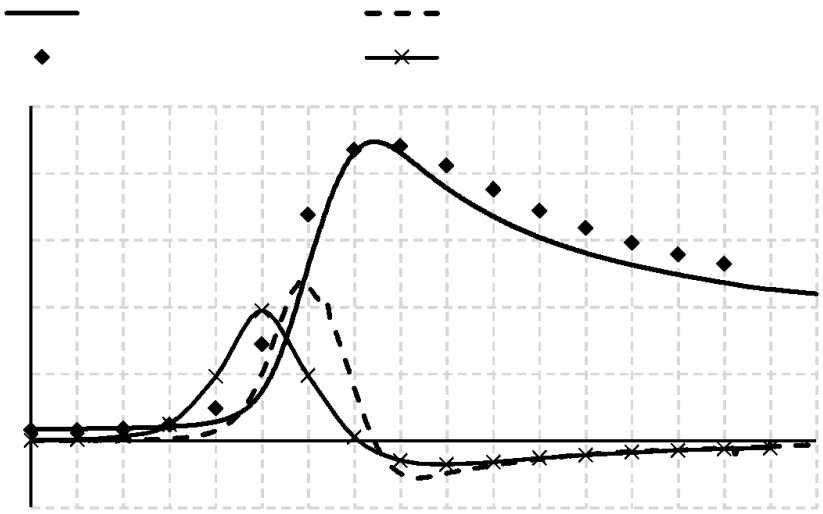

Source: The author (2025).

In the second welding pass, heating occurs between the time interval of 199s to 202,8s, reaching a peak temperature at t = 202,8s for the experimental process. In the numerical stage, heating occurs between the time interval of 199s to 203s, reaching peak temperature at t=203s. The dwell time at a temperature of 500 °C for the second welding pass is 18,68 s for the experimental and approximately 22 s for the numerical. Cooling from 800 °C to 500 °C takes 15.14 s for the experimental and approximately 18 s for the numerical, as shown in Fig. 83. Cooling from 800 °C to 300 °C takes 231.7 s for the experimental and approximately 234 s for the numerical, as shown in Fig. 81.

The highest heating and cooling rate values for the experimental process occurred at t = 202,8s and t = 203,86s, respectively. The highest heating and cooling rate values for the numerical process occurred at approximately t = 200s and t = 204s, as shown in Fig. 83.

Figure 81 – Thermal cycle and rate of temperature change for thermocouple T6 in the second pass.

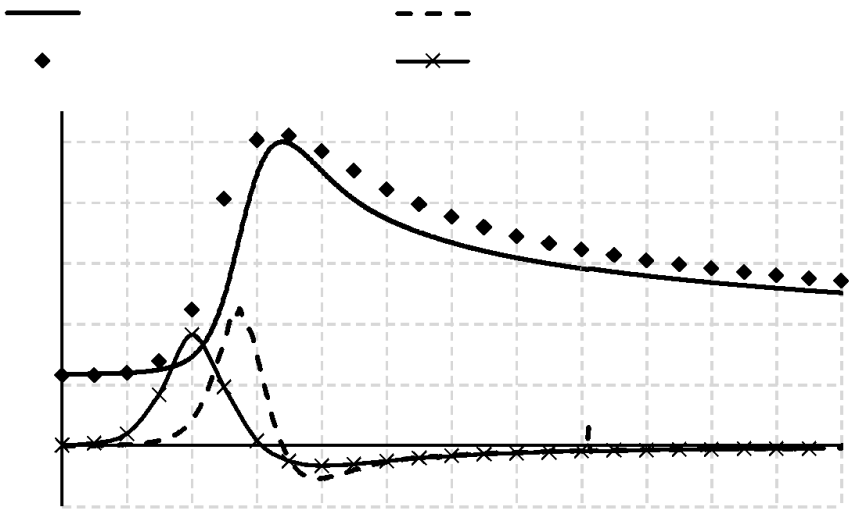

Source: The author (2025).

In the third welding pass, heating occurs between the time interval of 576s to 579.86s, reaching a peak temperature at t = 579.86s for the experimental process. In the numerical stage, heating occurs between the time interval of 576s to 580s, reaching a peak temperature at t = 580s. The residence time for the temperature of 500 °C, for the third welding pass, is 20.86 s for the experimental and approximately 25 s for the numerical. The cooling from 800 °C to 500 °C has a duration of 16.68 s for the experimental and approximately 19 s for the numerical, as shown in Fig. 84. The cooling from 800 °C to 300 °C has a duration of 244.28 s for the experimental and approximately 238 s for the numerical, as shown in Fig. 81.

The largest heating and cooling rate values for the experimental process occurred at t = 578.66 s and t = 580.94 s, respectively. The largest heating and cooling rate values for the numerical process occurred at approximately t = 577 s and t = 581 s, as shown in Fig. 84.

Figure 82 – Thermal cycle and rate of temperature change for thermocouple T6 in the third pass.

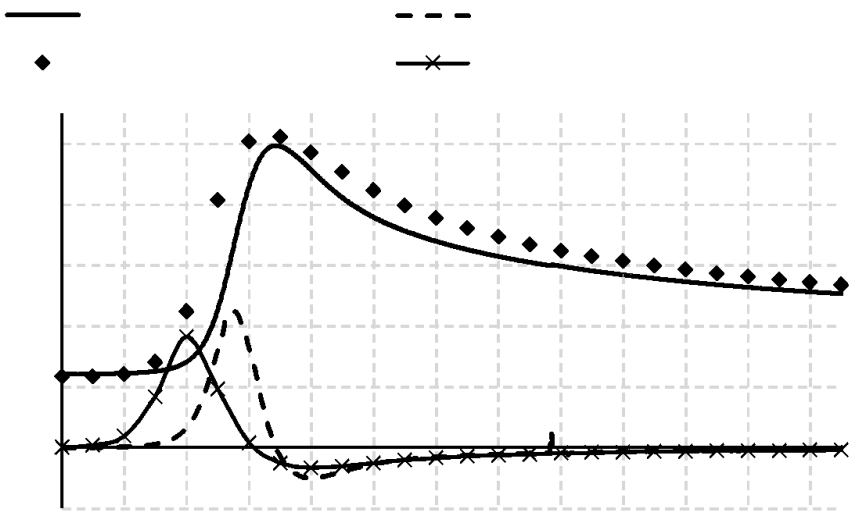

Source: The author (2025).

In the fourth welding pass, heating occurs between the time interval of 963 s to 967.74 s, reaching a peak temperature at t = 967.74 s for the experimental process. In the numerical stage, heating occurs between the time interval of 963 s to 968 s, reaching a peak temperature at t = 968 s. The time the temperature remains at 500 °C for the fourth welding pass is 25.10 s for the experimental and 25 s for the numerical. Cooling from 800 °C to 500 °C lasts 20.88 s for the experimental and 19 s for the numerical, as shown in Fig. 85. Cooling from 800 °C to 300 °C lasts 244.3 s for the experimental and 239 s for the numerical, as shown in Fig. 81.

The highest heating and cooling rate values for the experimental process occurred at t = 956,48 s and t = 958,86 s, respectively. The highest heating and cooling rate values for the numerical process occurred approximately at t = 965 s and t = 969 s, as shown in Fig. 85.

Figure 83 – Thermal cycle and rate of temperature change for thermocouple T6 in the fourth pass.

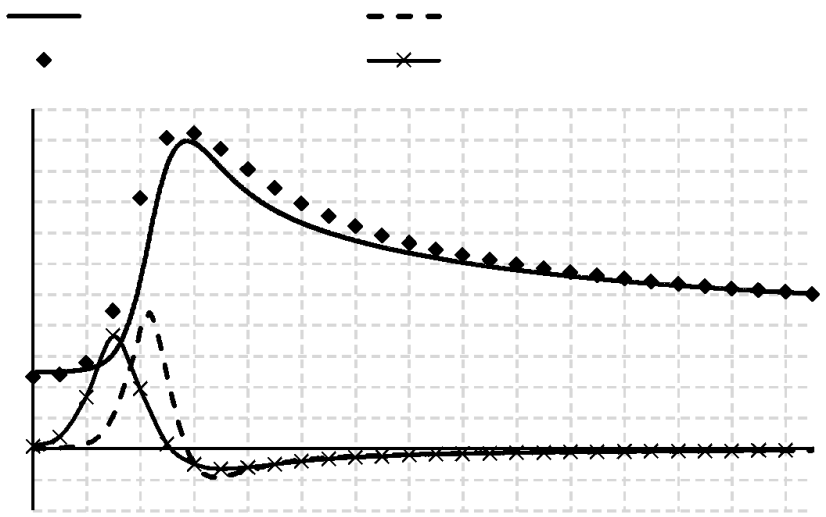

Source: The author (2025).

Table 8 shows the degree of agreement between the experimental and simulated temperature peaks for the T6 thermocouple.

Table 8 – Percentage error between experimental and simulated peak temperature values for thermocouple T6.

Temperatura (°C)	1 ° Passe	2° Passe	3° Passe	4° Passe
Experimental	894,02	998,74	992,65	996,98
EbFVM	880,64	1020,68	1023,2	1021,25
Erro percentual (%)	1,49	2,19	3,07	2,43

Source: The author (2025).

For the T6 thermocouple (0mm, 120mm, 2.92mm), the experimental results showed almost zero noise rate. The experimental values for peak temperatures, presented in Tab. 8, and heating and cooling profile were in agreement with the numerical results. The heating and cooling rate values were slightly similar when comparing the experimental results with the numerical results. The average percentage error for the total simulation time was 3%. Anisotropic factors of the thermal conductivity of the material in the autogenous TIG welding process stage was not perceived in the numerical simulation process that uses thermal conductivity with isotropic formalism. Thus, the level of divergence in the results was not significant.

Fig. 86 presents the results of the acquisition of the experimental and simulated thermal cycle of the four welding passes for the thermocouple in position T3 on top of the sample 120 mm from the starting point of the torch and perpendicularly distant 13 mm from the center of the weld bead, see Fig. 42.

Figure 84 – Thermal cycle with experimental and simulated T3 acquisition using a double ellipsoid source.

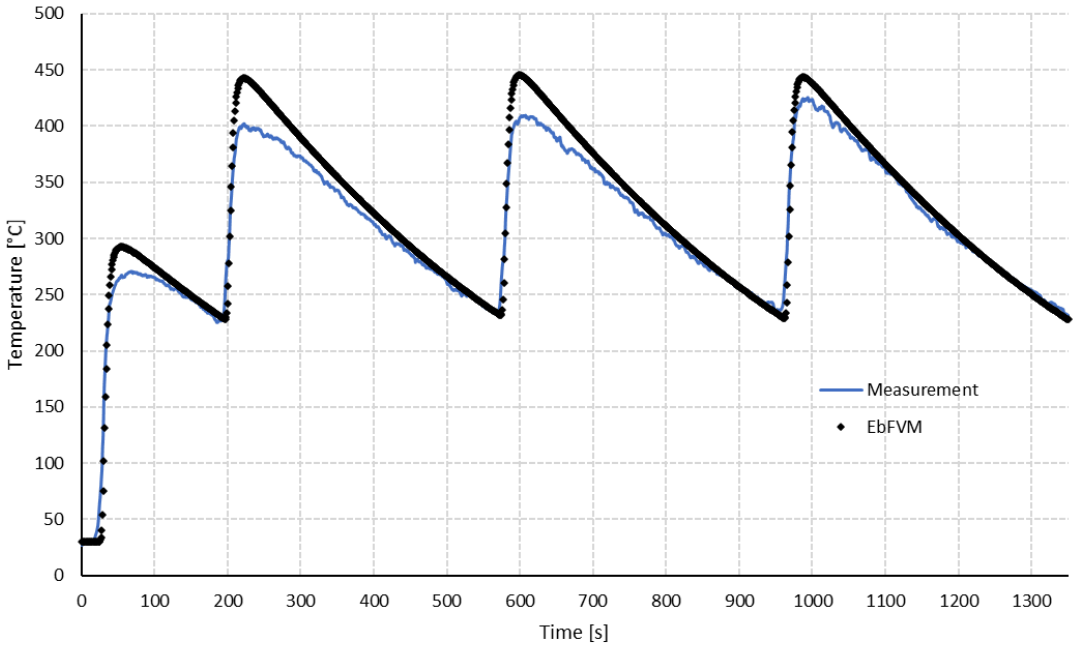

Source: The author (2025).

Heating in thermocouple T3 for the first welding pass occurs between the time interval of 20s to 54,90s, reaching a peak temperature at t = 54,90s for the experimental process. In the numerical stage, heating occurs between the time interval of 20s to 54s, reaching a peak temperature at t = 54s. The interval between the peaks of the last three passes is a sum of the torch travel time and the local cooling time until thermocouple T5, located at the base of the part, reaches the inter-pass temperature of 250 °C.

For the first weld pass, the dwell time of the temperature at 250 °C is 95,36 s for the experimental and approximately 110 s for the numerical. The cooling time from the peak temperature to 250 °C is 82,48 s for the experimental and approximately 145,32 s for the numerical, as shown in Fig. 86.

The highest heating and cooling rate values for the experimental process occurred at t = 30,3s and t=101,78s, respectively. The highest heating and cooling rate values for the numerical process occurred at t = 30s and t=103s, respectively.

In the second welding pass, heating occurs between the time interval of 200 s to 222,9 s, reaching a peak temperature at t = 222,9 s for the experimental process. In the numerical stage, heating occurs between the time interval of 200 s and 222 s, reaching a peak temperature at t = 222 s. The time the temperature remains at 350°C for the second welding pass is 125 s for the experimental one and approximately 150 s for the numerical one. Cooling from the peak temperature to 300°C lasts 202,58 s for the experimental one and approximately 216 s for the numerical one, as shown in Fig. 86.

The highest heating rate value for the experimental process occurred at t = 201,74s. It was not possible to accurately identify the time of the highest cooling rate. The highest heating and cooling rate values for the numerical process occur at t = 202s and t=264s, respectively.

In the third welding pass, heating occurs between the time interval of 570 s to 592,1 s, reaching a peak temperature at t = 592,1 s for the experimental process. In the numerical stage, heating occurs between the time interval of 570 s and 598 s, reaching a peak temperature at t = 598 s. The time the temperature remains at 350°C for the third welding pass is 131,6 s for the experimental one and approximately 155s for the numerical one. Cooling from the peak temperature to 300°C lasts 210,08s for the experimental one and approximately 216s for the numerical one, as shown in Fig. 86.

The highest heating and cooling rate values for the experimental process occurred at t = 580,12s and t= 640,76s, respectively. The highest heating and cooling rate values for the numerical process occurred at t = 580s and t=641s, respectively.

In the fourth welding pass, heating occurs between the time interval of 960 s to 986.58 s, reaching a peak temperature at t = 986.58 s for the experimental process. In the numerical stage, heating occurs between the time interval of 960 s and 987 s, reaching a peak temperature at t = 987 s. The time the temperature remains at 350°C for the fourth welding pass is 152,08s for the experimental one and approximately 153s for the numerical one. Cooling from the peak temperature to 300°C lasts 213,42s for the experimental one and approximately 215 s for the numerical one, as shown in Fig. 86.

The highest heating and cooling rate values for the experimental process occurred at t = 956,94s and t=1024,66s, respectively. The highest heating and cooling rate values for the numerical process occurred at t = 968s and t=1029s, respectively.

Table 9 shows the degree of agreement between the experimental and numerical temperature peaks for thermocouple T3.

Table 9 – Percentage error between experimental and simulated peak temperature values for thermocouple T3.

Temperatura (°C)	1 ° Passe	2° Passe	3° Passe	4° Passe
Experimental	270,64	402,03	409,11	424,13
EbFVM	292,33	442,69	445,41	443,41
Erro percentual (%)	8,01	10,12	8,87	4,55

Source: The author (2025).

For thermocouple T3 (13mm, 120mm, 6.3mm), the peak values showed divergences for the four welding passes. The cooling profile was similar from the middle of the cooling time interval. The heating and cooling rate values are in agreement for the four welding passes. The average percentage error for the total simulation time was 4%. The divergence between the peak values and the beginning of the cooling profile is a result of the anisotropy of the material's thermal conductivity. In the numerical step, the thermal conductivity term used has an isotropic formalism.

11.3 Experimental and numerical results, using double ellipsoid source, for AISI 409 steel and average welding current equal to 216A.

Fig. 87 presents the results of the acquisition of the experimental and numerical thermal cycle of the four welding passes for the thermocouple in the TB position in a blind hole of 3.03 mm from the base. This thermocouple is 80 mm from the initial movement position of the torch and is in the same line as the weld bead, see Fig. 47.

Figure 85 – Thermal cycle of the four welding passes with acquisition in the experimental and numerical TB thermocouple using a double ellipsoid source.

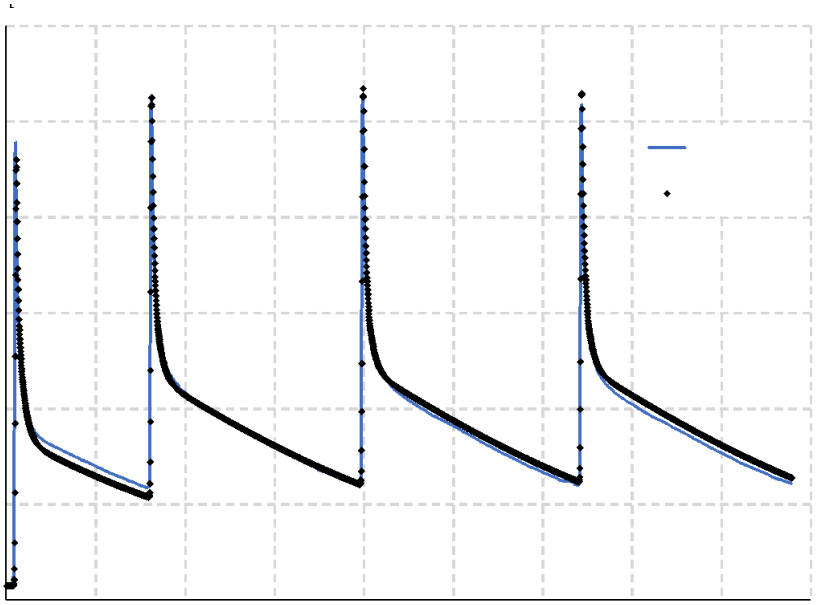

Source: The author (2025).

Heating in the TB thermocouple for the first welding pass occurs between the time interval of 15s and 21s, reaching the maximum temperature at t = 21s for the experimental process. In the numerical stage, heating occurs between the time interval of 15s and 21s, reaching the peak temperature at t = 21s. The interval between the peaks of the last three passes is a sum of the torch travel time and the local cooling time until the TC thermocouple, located at the base of the part, reaches the inter-pass temperature of 250 °C.

For the first weld pass, the dwell time at 500 °C is 12,58 s for the experimental and approximately 15 s for the numerical. The cooling time from 800 °C to 500 °C is 8,66 s for the experimental and approximately 9 s for the numerical, as shown in Fig. 88. The cooling time from 800 °C to 300 °C is 129,32 s for the experimental and approximately 103 s for the numerical, as shown in Fig. 87.

The highest heating and cooling rate values for the experimental process occurred at t = 19s and t = 22.18s, respectively. The highest heating and cooling rate values for the numerical process occurred at t = 19s and t=22s, respectively, as shown in Fig. 88.

Figure 86 – Thermal Cycle and First Pass Temperature Change Rate for Thermocouple TB.

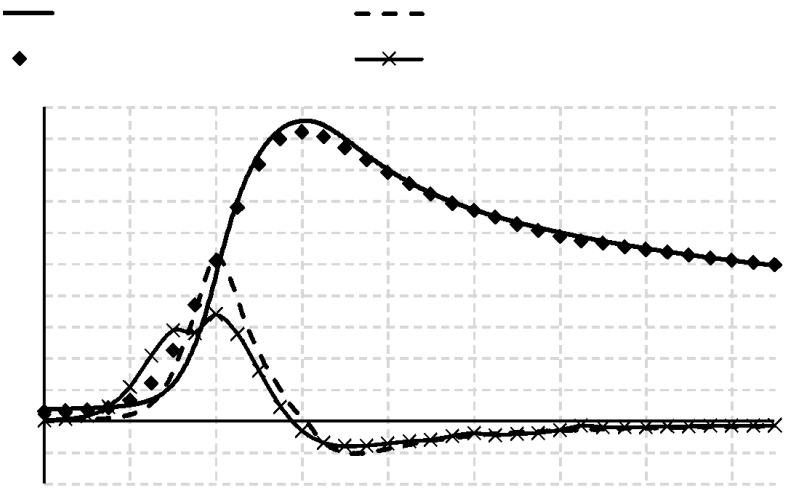

Source: The author (2025).

In the second welding pass, heating occurs between the time interval of 320 s and 325,1 s, reaching the peak temperature at t = 325,1 s for the experimental process. In the numerical stage, heating occurs between the time interval of 320 s and 325 s, reaching the peak temperature at t = 325 s. The time the temperature remains at 500 °C for the second welding pass is 31,66 s for the experimental one and approximately 32 s for the numerical one. Cooling from 800 °C to 500 °C lasts 24,92 s for the experimental one and approximately 22 s for the numerical one, as shown in Fig. 89. Cooling from 800 °C to 300 °C lasts 311,08 s for the experimental one and approximately 319 s for the numerical one, as shown in Fig. 87.

The highest heating and cooling rate values for the experimental process occurred at t = 322.8 s and t = 327.06 s, respectively. The highest heating and cooling rate values for the numerical process occurred approximately at t = 323 s and t = 327 s, respectively, as shown in Fig. 89.

Figure 87 – Thermal cycle and rate of temperature change for the TB thermocouple second pass.

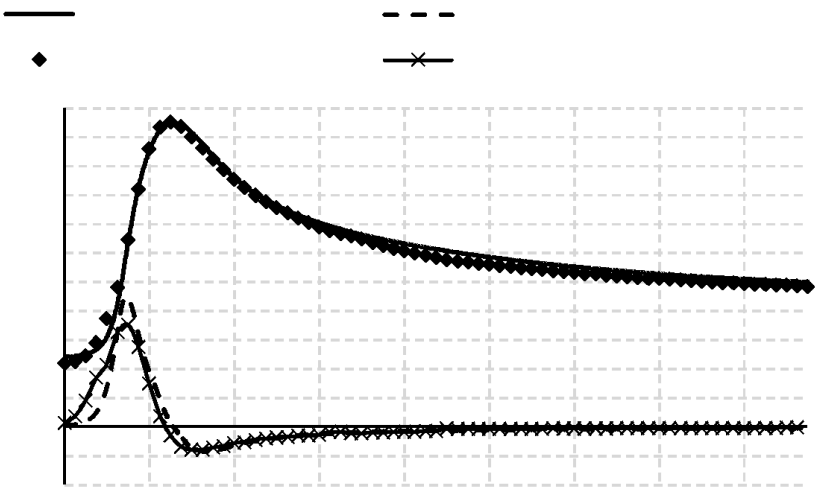

Source: The author (2025).

In the third welding pass, heating occurs between the time interval of 791 s to 797.96 s, reaching a peak temperature at t = 797.96 s for the experimental process. In the numerical stage, heating occurs between the time interval of 791 s and 798 s, reaching a peak temperature at t = 798 s. The residence time for a temperature of 500 °C for the third welding pass is 32.44 s for the experimental one and approximately 33 s for the numerical one. Cooling from 800 °C to 500 °C lasts 26.06 s for the experimental one and approximately 26 s for the numerical one, as shown in Fig. 85. Cooling from 800 °C to 300 °C lasts 322.36 s for the experimental one and 344 s for the numerical one, as shown in Fig. 87.

The highest heating and cooling rate values for the experimental process occurred at t = 796 s and t = 800,52 s, respectively. The highest heating and cooling rate values for the numerical process occur approximately at t = 795 s and t = 800 s, respectively, as shown in Fig. 90.

Figure 88 – Thermal Cycle and Rate of Temperature Change for the Third Pass TB Thermocouple.

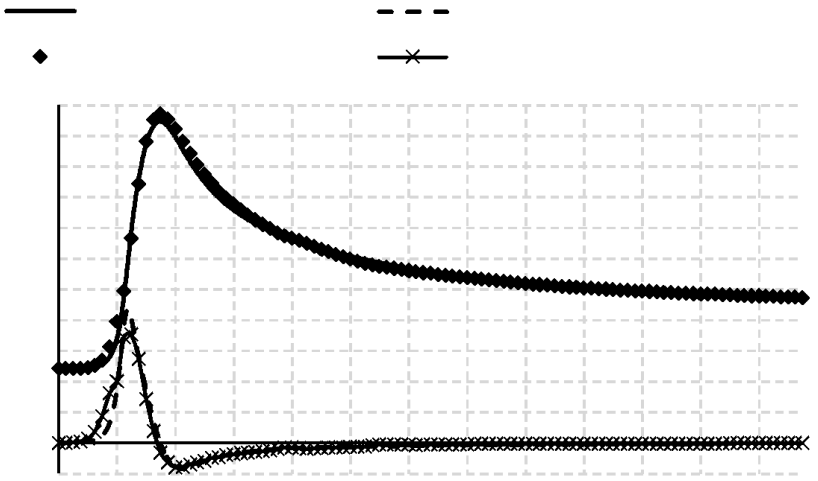

Source: The author (2025).

In the fourth welding pass, heating occurs between the time interval of 1280s and 1287,08s, reaching a peak temperature at t = 1287,08s for the experimental process. In the numerical stage, heating occurs between the time interval of 1280s and 1287s, reaching a peak temperature at t = 1287s. The residence time for the temperature of 500 °C for the fourth weld pass is 31,14 s for the experimental and 34,5 s for the numerical. The cooling from 800 °C to 500 °C has a duration of 25,08 s for the experimental and 27,5 s for the numerical, as shown in Fig. 91. The cooling from 800 °C to 300 °C has a duration of 323,08 s for the experimental and 356 s for the numerical, as shown in Fig. 87.

The highest heating and cooling rate values for the experimental process occurred at t = 1285 s and t = 1288,42 s, respectively. The highest heating and cooling rate values for the numerical process occurred approximately at t = 1285 s and t = 1289 s, respectively, as shown in Fig. 91.

Figure 89 – Thermal Cycle and Rate of Temperature Change for Fourth Pass Thermocouple TB.

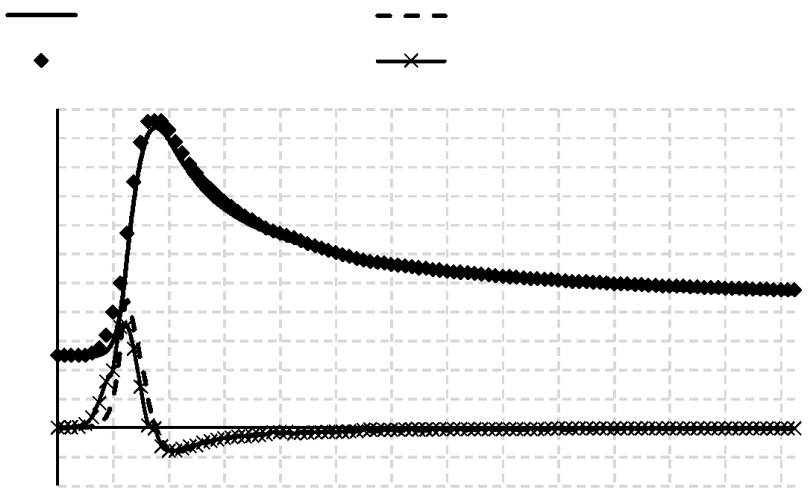

Source: The author (2025).

Table 10 shows the degree of agreement between the experimental and numerical temperature peaks for the thermocouple TB.

Table 10 – Percentage error between experimental and simulated peak temperature values for thermocouple TB.

Temperatura (°C)	1 ° Passe	2° Passe	3° Passe	4° Passe
Experimental	955,29	1047,4	1045,7	1035,6
EbFVM	931,74	1064,77	1069,43	1085,6
Erro percentual (%)	2,46	1,65	2,26	4,85

Source: The author (2025).

For the thermocouple TB(0mm, 80mm, 3,03mm), the experimental results showed almost zero noise rate. The experimental values for peak temperatures and heating and cooling profile were in agreement with the numerical results. The heating and cooling rate values were slightly similar when comparing the experimental results with the numerical results. The average percentage error for the total simulation time was 6,14%. Anisotropic factors of the thermal conductivity of the material in the autogenous TIG welding process stage was not perceived in the numerical simulation process that uses thermal conductivity with isotropic formalism. Thus, the level of divergence in the results was not significant in the peak temperatures and heating and cooling rates.

Fig. 92 presents the results of the acquisition of the experimental and numerical thermal cycle of the four welding passes for the thermocouple in the TC position at the base of the sample and 100 mm from the beginning of the part, see Fig. 47.

Figure 90 – Thermal cycle with experimental and simulated TC acquisition using a double ellipsoid source.

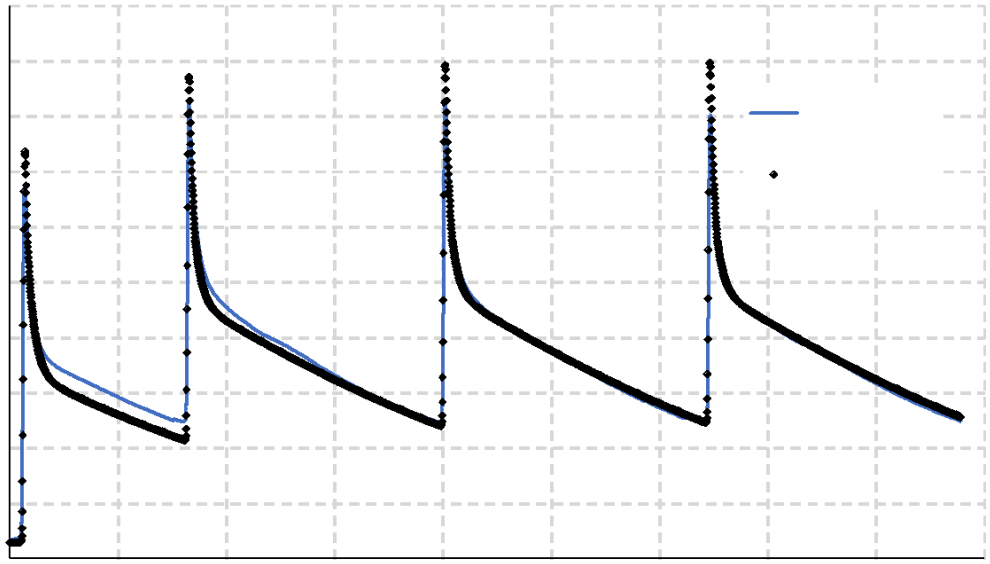

Source: The author (2025).

Heating in the TC thermocouple for the first welding pass occurs between the time interval of 17s and 28s, reaching the maximum temperature at t = 28s for the experimental process. In the numerical stage, heating occurs between the time interval of 17s to 28,5s, reaching the peak temperature at t = 28,5s. The interval between the peaks of the last three passes is a sum of the torch travel time and the local cooling time until the TC thermocouple reaches the inter-pass temperature of 250 °C.

For the first weld pass, the dwell time at 500 °C is 11,92 s for the experimental and approximately 12 s for the numerical. The cooling time from 600 °C to 500 °C is 5,36 s for the experimental and approximately 5 s for the numerical, as shown in Fig. 93. The cooling from 600 °C to 300 °C has a duration of 147,5 s for the experimental and 77,5 s for the numerical, as shown in Fig. 92.

The highest heating and cooling rate values for the experimental process occurred at t = 24,64 s and t = 31,44 s, respectively. The highest heating and cooling rate values for the numerical process occurred at t = 24,5 s and t = 30 s, respectively, as shown in Fig. 93.

Figure 91 – Thermal Cycle and Rate of Change of Temperature for the First Pass TC Thermocouple.

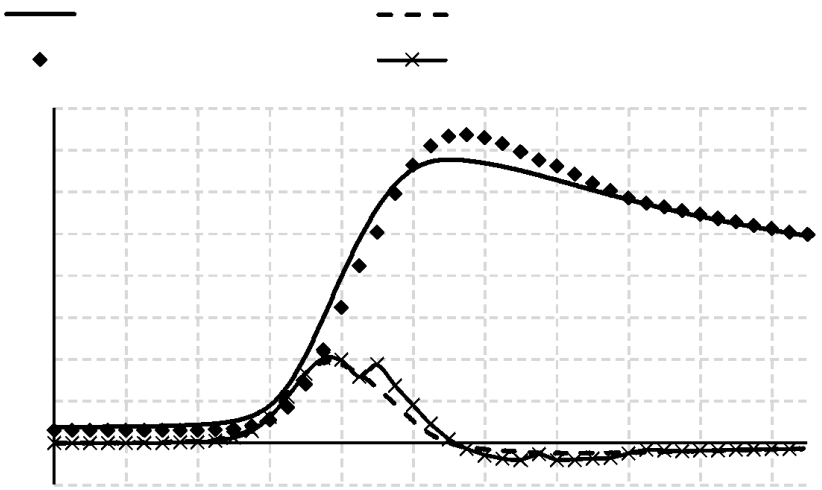

Source: The author (2025).

In the second welding pass, heating occurs between the time interval of 326s and 331,96s reaching peak temperature at t = 331,96s for the experimental process. In the numerical stage, heating occurs between the time interval of 326s to 331,5s reaching peak temperature at t = 331,5s. The dwell time at 500 °C for the second weld pass is 37,28 s for the experimental and 27 s for the numerical. Cooling from 800 °C to 500 °C lasts 32,54 s for the experimental and approximately 21,5 s for the numerical, as shown in Fig. 94. Cooling from 800 °C to 300 °C lasts 325,7 s for the experimental and approximately 314 s for the numerical, as shown in Fig. 92.

The highest heating and cooling rate values for the experimental process occurred at t = 328,66 s and t = 333,06 s, respectively. The highest heating and cooling rate values for the numerical process occurred at t = 328,5 s and t = 333 s, respectively, as shown in Fig. 94.

Figure 92 – Thermal Cycle and Rate of Temperature Change for the Second Pass TC Thermocouple.

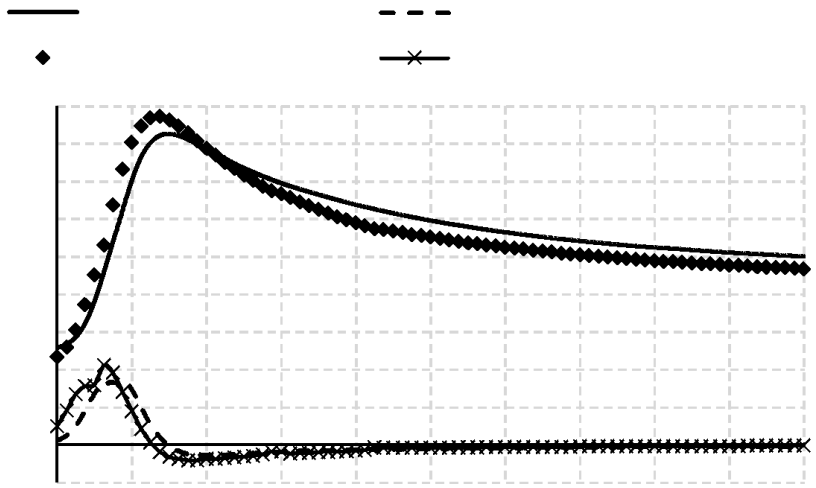

Source: The author (2025).

In the third welding pass, heating occurs between the time interval of 796 s to 804,92 s, reaching the peak temperature at t = 804.92 s for the experimental process. In the numerical stage, heating occurs between the time interval of 796 s to 804,5 s, reaching the peak temperature at t = 804,5 s. The residence time for a temperature of 500 °C for the third welding pass is 36.98 s for the experimental one and approximately 32 s for the numerical one. Cooling from 800 °C to 500 °C lasts 32,44 s for the experimental one and approximately 26 s for the numerical one, as shown in Fig. 95. Cooling from 800 °C to 300 °C lasts 333,06 s for the experimental one and approximately 348 s for the numerical one, as shown in Fig. 92.

The highest heating and cooling rate values for the experimental process occurred at t = 802,1 s and t = 806,78 s, respectively. The highest heating and cooling rate values for the numerical process occurred at t = 801,5 s and t = 806,5 s, respectively, as shown in Fig. 95.

Figure 93 – Thermal Cycle and Rate of Temperature Change for the Third Pass TC Thermocouple.

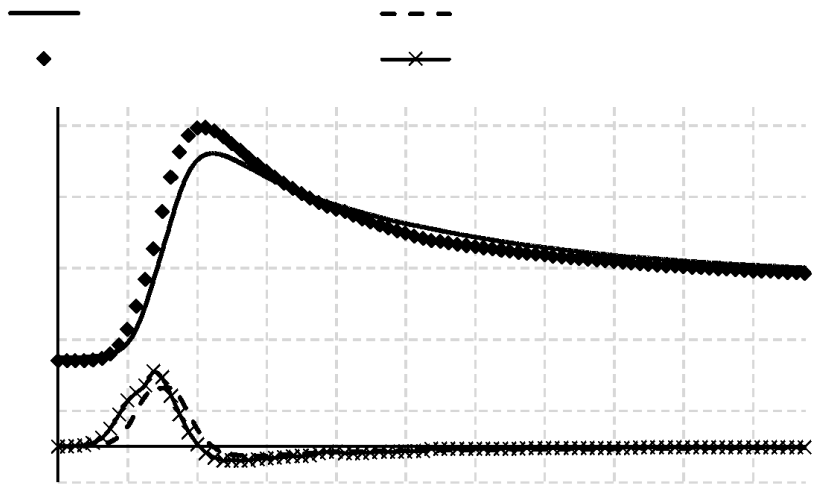

Source: The author (2025).

In the fourth welding pass, heating occurs between the time interval of 1280 s to 1294,16 s, reaching a peak temperature at t = 1294,16 s for the experimental process. In the numerical stage, heating occurs between the time interval of 1280 s to 1293,5 s, reaching a peak temperature at t = 1293,5 s. The residence time for a temperature of 500 °C for the fourth welding pass is 35 s for the experimental one and 33 s for the numerical one. Cooling from 800 °C to 500 °C lasts 31,5 s for the experimental one and 27 s for the numerical one, as shown in Fig. 96. Cooling from 800 °C to 300 °C lasts 338 s for the experimental one and 355 s for the numerical one, as shown in Fig. 92.

The largest heating and cooling rate values for the experimental process occurred at t = 1291,2 s and t = 1296,24 s, respectively. The largest heating and cooling rate values for the numerical process occurred at t = 1290,5 s and t = 1295 s, respectively, as shown in Fig. 96.

Figure 94 – Thermal Cycle and Rate of Temperature Change for Fourth Pass TC Thermocouple.

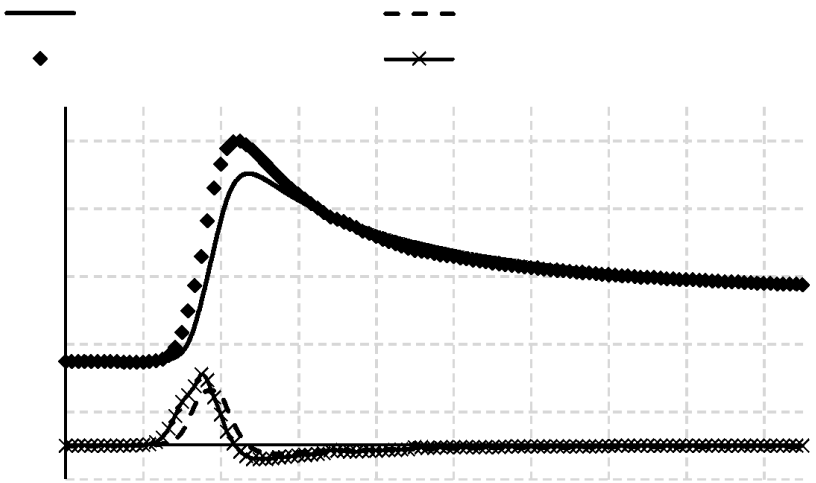

Source: The author (2025).

Table 11 shows the degree of agreement between the experimental and simulated temperature peaks for the TC thermocouple.

Table 11 – Percentage error between experimental and simulated peak temperature values for the TC thermocouple.

Temperatura (°C)	1 ° Passe	2° Passe	3° Passe	4° Passe
Experimental	675,99	825,16	820,09	802,07
EbFVM	736,14	871,61	892,64	897,65
Erro percentual (%)	8,89	5,63	8,84	11,91

Source: The author (2025).

For the TC thermocouple (0mm, 100m, 0mm), the experimental results showed an almost zero noise rate. The experimental peak values were divergent. The average percentage error for the total simulation time was 4,83%. The anisotropic factor of the thermal conductivity of the material in the autogenous TIG welding process stage was perceived in the numerical simulation process that uses thermal conductivity with isotropic formalism for thermocouples fixed in regions distant from the molten zone. The heating and cooling profiles and the heating and cooling rate values were in agreement when comparing the experimental results with the numerical results.

The TC thermocouple captured thermal cycles with a welding current of 216A. The T5 thermocouple captured thermal cycles with a welding current of 165A. Both

thermocouples were in the same position relative to the start of torch movement on different parts. The experiment with the highest temperature has greater penetration power, therefore, the distance between the molten zone and the thermocouple is smaller. When comparing the temperature difference between the two experiments with different welding currents, a smaller difference is observed for the experiment with the highest welding current. This indicates that regions further away from the molten zone are more sensitive to the anisotropy of the material's thermal conductivity coefficient.

Fig. 97 presents the results of the experimental and numerical thermal cycle acquisition of the four welding passes for the thermocouple in the TD position in a blind hole of 2.47 mm from the base of the part. The thermocouple is 120 mm from the initial movement position of the torch and is in the same line as the weld bead, see Fig. 47.

Figure 95 – Thermal cycle of the four welding passes with acquisition in the experimental and numerical TD thermocouple using a double ellipsoid source.

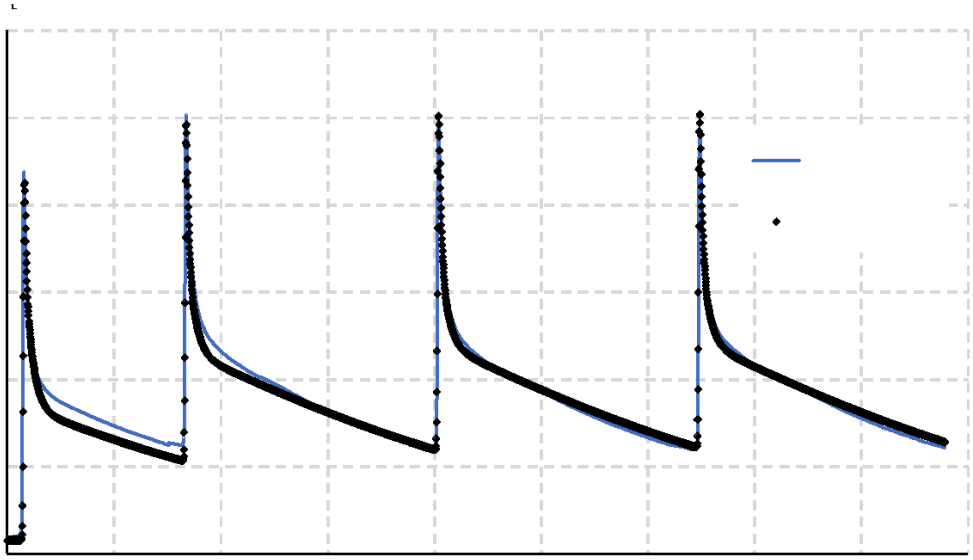

Source: The author (2025).

The heating of the thermocouple TD (0mm, 120mm, 2,47mm) for the first welding pass occurs between the time interval of 20s and 31,60s, reaching a peak temperature at t = 31,60s for the experimental stage. In the numerical stage, the heating occurs between the time interval of 20s and 32s, reaching a peak temperature at t = 32s. The interval between the peaks of the last three passes is a sum of the torch travel time and the local cooling time until the thermocouple TC, located at the base of the part, reaches the inter-pass temperature of 250 °C.

For the first pass, the residence time at 500 °C is 13.36 s for the experimental and approximately 13 s for the numerical. The cooling time from 800 °C to 500 °C is 10,22 s for the experimental and approximately 9 s for the numerical, as shown in Fig. 98. The cooling time from 800 °C to 300 °C is 152,44 s for the experimental and 78 s for the numerical, as shown in Fig. 97.

The largest heating and cooling rate values for the experimental process occurred at t = 29,52 s and t = 32,98 s, respectively. The largest heating and cooling rate values for the numerical process occurred at t = 29,5 s and t = 33,5 s, respectively, as shown in Fig. 98.

Figure 96 – Thermal cycle and rate of temperature change for the TD thermocouple in the first pass.

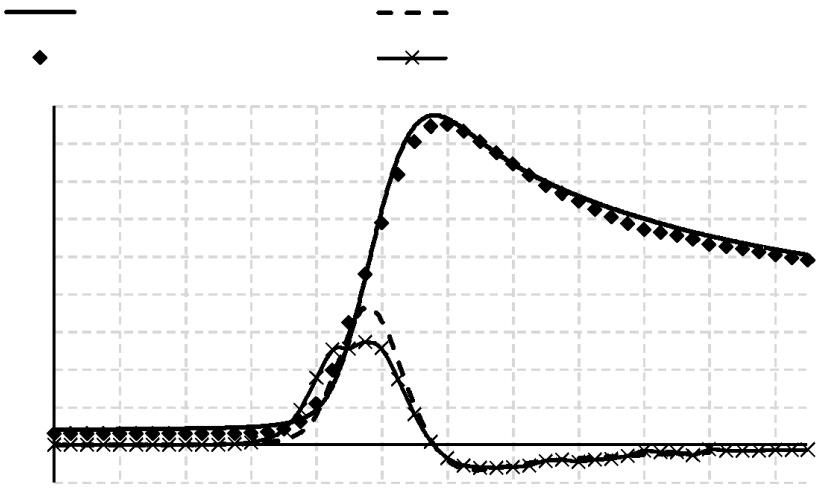

Source: The author (2025).

In the second welding pass, heating occurs between the time interval of 326 s to 336 s, reaching a peak temperature at t = 336 s for the experimental stage. In the numerical stage, heating occurs between the time interval of 326 s and 336 s, reaching a peak temperature at t = 336 s. The time the temperature remains at 500 °C is 42,2 s for the experimental stage and approximately 27 s for the numerical stage. Cooling from 800 °C to 500 °C lasts 35,36 s for the experimental process and approximately 22 s for the numerical stage, as shown in Fig. 99. Cooling from 800 °C to 300 °C lasts 308,24 s for the experimental stage and 310 s for the numerical stage, as shown in Fig. 97.

The largest heating and cooling rate values for the experimental process occurred at t = 333,38 s and t = 337 s, respectively. The largest heating and cooling rate values for the numerical process occurred at t = 333 s and t = 337 s, respectively, as shown in Fig. 99.

Figure 97 – Thermal cycle and rate of temperature change for the TD thermocouple in the second pass.

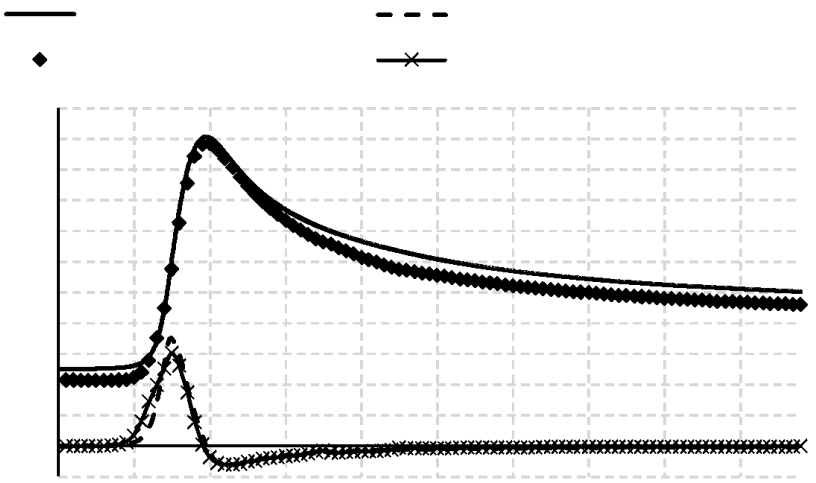

Source: The author (2025).

In the third welding pass, heating occurs between the time interval of 798 s to 809 s, reaching a peak temperature at t = 809 s for the experimental process. In the numerical stage, heating occurs between the time interval of 798 s and 809 s, reaching a peak temperature at t = 809 s. The residence time for a temperature of 500 °C is 40,62 s for the experimental process and approximately 32 s for the numerical process. Cooling from 800 °C to 500 °C lasts 34,1 s for the experimental process and approximately 25 s for the numerical process, as shown in Fig. 100. Cooling from 800 °C to 300 °C lasts 312,24 s for the experimental process and 342 s for the numerical process, as shown in Fig. 97.

The largest heating and cooling rate values for the experimental process occurred at t = 806,32 s and t = 810,14 s, respectively. The largest heating and cooling rate values for the numerical process occurred at t = 806 s and t = 809,5 s, respectively, as shown in Fig. 100.

Figure 98 – Thermal cycle and rate of temperature change for the TD thermocouple in the third pass.

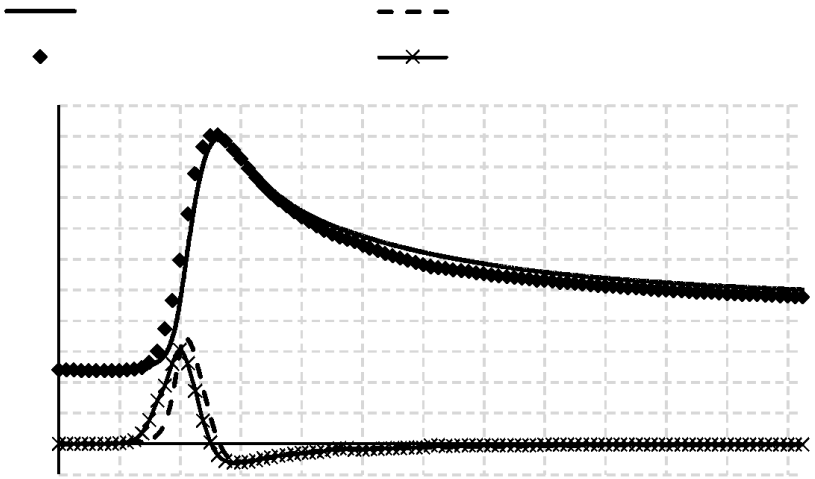

Source: The author (2025).

In the fourth welding pass, heating occurs between the time interval of 1282 s to 1297,84 s, reaching a peak temperature at t = 1297,84 s for the experimental process. In the numerical stage, heating occurs between the time interval of 1282 s and 1298 s, reaching a peak temperature at t = 1298 s. The residence time for a temperature of 500 °C is 41,1 s for the experimental one and approximately 33 s for the numerical one. Cooling from 800 °C to 500 °C lasts 34,9 s for the experimental one and approximately 26 s for the numerical one, as shown in Fig. 101. Cooling from 800 °C to 300 °C lasts 317,8 s for the experimental one and 348 s for the numerical one, as shown in Fig. 97.

The largest heating and cooling rate values for the experimental process occurred at t = 1295,54 s and t = 1299,66 s, respectively. The largest heating and cooling rate values for the numerical process occurred at t = 1295,5 s and t = 1299 s, respectively, as shown in Fig. 101.

Figure 99 – Thermal cycle and rate of temperature change for the TD thermocouple in the fourth pass.

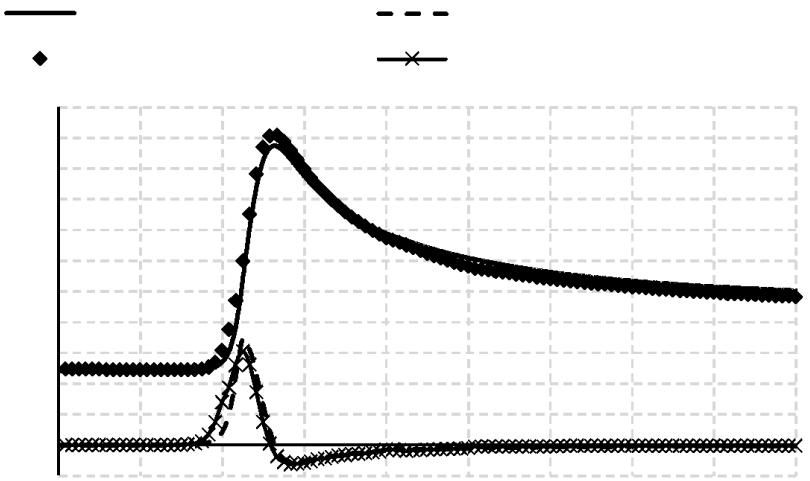

Source: The author (2025).

Table 12 shows the degree of agreement between the experimental and simulated temperature peaks for the TD thermocouple.

Table 12 – Percentage error between experimental and simulated peak temperature values for the TD thermocouple.

Temperatura (°C)	1 ° Passe	2° Passe	3° Passe	4° Passe
Experimental	874,81	1005,2	991,5	973,43
EbFVM	849,72	982,7	1002,73	1005,86
Erro percentual (%)	2,86	2,23	1,06	3,33

Source: The author (2025).

For the TD thermocouple, the experimental results showed almost zero noise rate. The experimental values for peak temperatures and heating and cooling profile were in agreement with the numerical results. The heating and cooling rate values were slightly similar when comparing the experimental results with the numerical results. The average percentage error for the total simulation time was 6%. Anisotropic factors of the thermal conductivity of the material in the autogenous TIG welding process stage was not perceived in the numerical simulation process that uses thermal conductivity with isotropic formalism in regions closer to the molten zone. Thus, the level of divergence in the results was not significant in the peak temperatures and heating and cooling rates.

Fig. 102 presents the results of the experimental and simulated thermal cycle acquisition of the four welding passes for the thermocouple in the TA position on top of the sample. The thermocouple is 120 mm from the welding start position and, in the perpendicular direction, 13 mm from the weld bead, see Fig. 46.

Figure 100 – Thermal cycle with experimental and simulated TA acquisition using a double ellipsoid source.

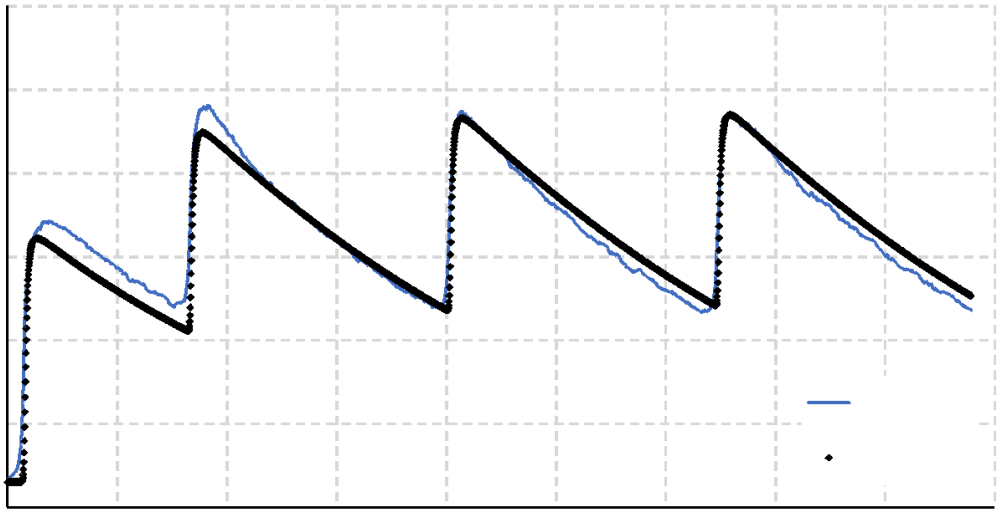

Source: The author (2025).

The heating of the thermocouple TA (13mm, 120mm, 6.3mm) for the first welding pass occurs between the time interval of 22s to 65,38s, reaching a peak temperature at t = 65,38s for the experimental. For the numerical one, the heating occurs between t = 26s and t = 54s from the beginning of the torch movement, reaching a maximum temperature at t = 54s. The interval between the peaks of the last three passes is a sum of the torch travel time and the local cooling time until the thermocouple TC, located at the base of the part, reaches the inter-pass temperature of 250 °C.

For the first welding pass, the dwell time at the temperature of 300 °C is 136,66 s for the experimental and approximately 64 s for the numerical, as shown in Fig. 103.

The highest heating and cooling rate values for the experimental process occurred at t = 29,52 s and t = 130,66 s, respectively. The highest heating and cooling rate values for the numerical process occurred at t = 32 s and t = 126 s, respectively, as shown in Fig. 103.

Figure 101 – Thermal cycle and rate of temperature change for the TA thermocouple in the first pass.

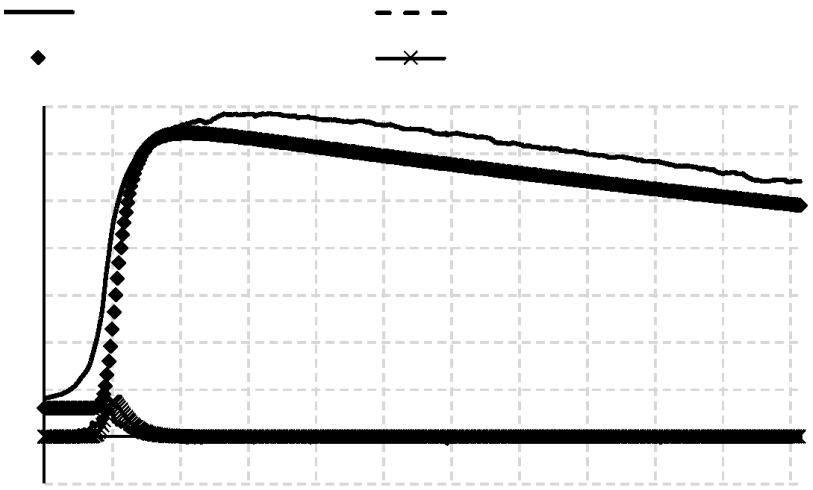

Source: The author (2025).

In the second welding pass, heating occurs between the time interval of 328 s to 351,44 s, reaching a peak temperature at t = 351,44 s for the experimental process. In the numerical stage, heating occurs between the time interval of 328 s to 356 s, reaching a peak temperature at t = 356 s. The time the temperature remains at 400 °C for the second welding pass is 119 s for the experimental one and approximately 105 s for the numerical one, as shown in Fig. 104.

The largest heating and cooling rate values for the experimental process occurred at t = 333,68 s and t = 388,82 s, respectively. The largest heating and cooling rate values for the numerical process occurred at approximately t = 335 s and t = 389 s, respectively, as shown in Fig. 104.

Figure 102 – Thermal cycle and rate of temperature change for the TA thermocouple in the second pass.

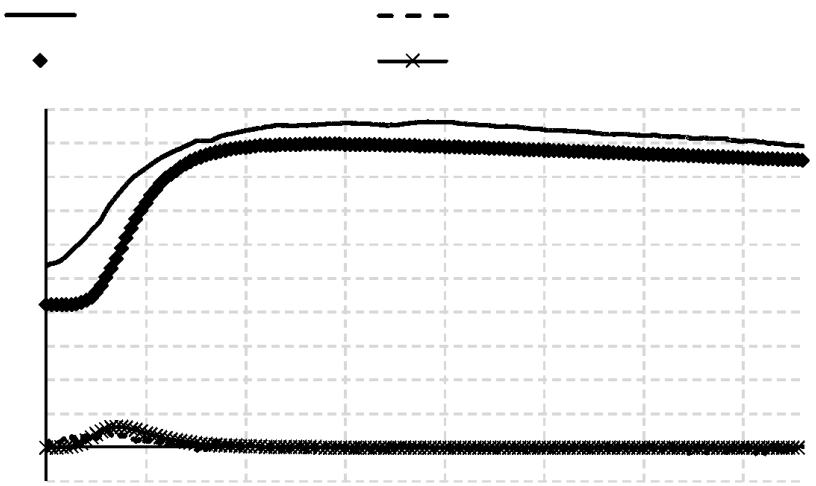

Source: The author (2025).

In the third welding pass, heating occurs between the time interval of 820 s to 829,9 s, reaching a peak temperature at t = 829,9 s for the experimental process. In the numerical stage, heating occurs between the time interval of 800 s to 828,5 s, reaching a peak temperature at t = 828,5 s. The time the temperature remains at 450 °C for the third welding pass is 48,3 s for the experimental one and approximately 44 s for the numerical one, as shown in Fig. 105.

The highest heating and cooling rate values for the experimental process occurred at t = 806,8 s and t = 854,06 s, respectively. The highest heating and cooling rate values for the numerical process occurred, approximately, at t = 808 s and t = 866 s, respectively, as shown in Fig. 105.

Figure 103 – Thermal Cycle and Rate of Temperature Change for the Third Pass TA Thermocouple.

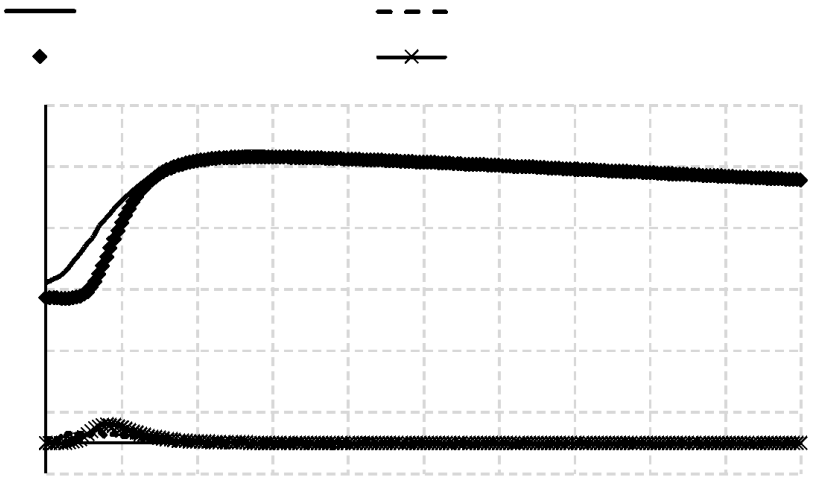

Source: The author (2025).

In the fourth welding pass, heating occurs between the time interval of 1280 s to 1315,84 s, reaching a peak temperature at t = 1315,84 s for the experimental process. In the numerical stage, heating occurs between the time interval of 1280 to 1318 s, reaching a peak temperature at t = 1318 s. The time the temperature remains at 450 °C for the fourth welding pass is 55,2 s for the experimental and 52 s for the numerical, as shown in Fig. 106.

The largest heating and cooling rate values for the experimental process occurred at t = 1295,86 s and t = 1353,9 s, respectively. The largest heating and cooling rate values for the numerical process occurred at approximately t = 1296 s and t = 1356 s, respectively, as shown in Fig. 106.

Figure 104 – Thermal Cycle and Rate of Temperature Change for Fourth Pass Thermocouple TA.

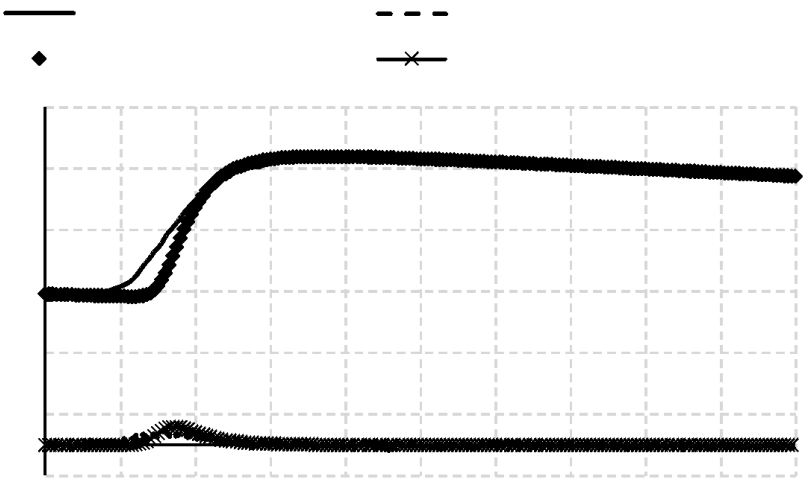

Source: The author (2025).

Tab. 13 shows the degree of agreement between the experimental and numerical temperature peaks for the TA thermocouple.

Table 13 – Percentage error between experimental and simulated peak temperature values for the TA thermocouple.

Temperatura (°C)	1 ° Passe	2° Passe	3° Passe	4° Passe
Experimental	342,29	476,25	473,88	468,03
EbFVM	321,32	447,8	465,08	469,15
Erro percentual (%)	6,12	5,97	1,85	0,23

Source: The author (2025).

For the TA thermocouple, located at the top of the part and close to the torch, the experimental results presented a slight noise rate. The experimental values of peak and heating and cooling profile were slightly divergent when compared to the numerical results. The heating and cooling rate values presented agreement when comparing the experimental results with the numerical results. The average percentage error for the total simulation time was 6%. Better agreement is observed when comparing the TA thermocouple with the T3 thermocouple, both are in the same position, however, in different samples. In the TA thermocouple experiment, the weld bead is wider, bringing the molten zone closer to the TA

thermocouple and reducing the perception of anisotropic influence of the thermal conductivity coefficient.

12 CONCLUSIONS

12.1 The general objective of:

Develop numerical routines written in FORTRAN 90, capable of simulating, from the EbFVM point of view, the behavior of the thermal cycles of the autogenous TIG welding process in metal sheets. It was achieved because the simulator obtained results that agreed with data acquired in the literature and from controlled experiments in the LPTS-UFC laboratory.

12.2 The specific objectives of:

The first objective was: to carry out a controlled laboratory study (LPTS-UFC) of thermal cycles using k-type thermocouples in different positions on the AISI 409 stainless steel sample with two values of electric current, which was successfully achieved. The experimental data were plotted on the graphs in continuous lines showing that the experiment did not obtain noise in the data acquisition. The peak temperature values for the last three passes showed agreement for each welding pass with an inter-pass temperature of 250°C.

The second objective was: to validate the numerical simulator, which uses the EbFVM methodology, by comparing the numerical results with those obtained in the literature, as well as comparison with the experimental results. It was successfully achieved. The results of the EbFVM numerical simulator of the thermal cycles of the autogenous TIG welding process were compared with results consolidated in the article and data from the experimental process controlled in the laboratory.

The third objective was: to analyze the influence of the heat source model in the numerical simulation stage, comparing it with experimental results. This stage of the specific objectives was successfully completed. The different numerical source models of the circular, double ellipse and semi-ellipsoid types presented values close to those of controlled laboratory experiments. However, the one that presented the best results in the heating, peak and cooling intervals was the double ellipsoid source, strengthening its wide use in scientific articles.

The comparison between thermal cycles allowed us to identify that the disagreement between experimental and numerical results for thermocouples far from the molten zone can be greatly influenced by the anisotropy of the material's thermal conductivity coefficient. It

was possible to see that in regions close to the weld bead, the model with isotropic thermal conductivity coefficient agrees with real experiments that take into account the anisotropy of this coefficient.

Future Work

In order to carry out a more detailed study, the following analysis is recommended for future research with the developed simulator:

1 – Perform the autogenous TIG welding process on different metal sheets;

2 – Carry out a thermomechanical analysis of AISI 409 stainless materials based on the thermal data from this work;

3 – Perform numerical simulations with cylindrical geometries and compare with controlled experimental results in the laboratory.

REFERENCES

(1) GARCÍA, V.; ARRIAGA, J. C. C.; REYES-CALDERÓN, F. A. A simplified elliptic paraboloid heat source model for autogenous GTAW process. **International Journal of Heat and Mass Transfer**, [s.l], v. 100, p. 536–549, 2016. Disponível em: https://www.sciencedirect.com/science/article/pii/S0017931015316835. Acesso em: 1 out. 2025.

(2) GERY, D.; LONG, H.; MAROUPOLOS, P. Effects of welding speed, energy input and heat source distribution on temperature variations in butt joint welding. **Journal of Materials Processing Technology**, [s.l], v. 167, p. 393–401, 2005. Disponível em: https://www.sciencedirect.com/science/article/pii/S0924013605005819. Acesso em: 1 out. 2025.

(3) DAS, R.; CLEARY, P. W. Three-dimensional modelling of coupled flow dynamics, heat transfer and residual stress generation in arc welding processes using the mesh-free SPH method. **Journal of Computational Science**, [s.l], v. 16, p. 200–216, 2016. Disponível em: https://www.sciencedirect.com/science/article/pii/S1877750316300266. Acesso em: 1 out. 2025.

(4) DENG, D. FEM prediction of welding residual stress and distortion in carbon steel considering phase transformation effects. **Materials & Design**, [s.l], v. 30, n. 2, p. 359–366, 2009. Disponível em: https://www.sciencedirect.com/science/article/pii/S0261306908001556. Acesso em: 1 out. 2025.

(5) ZENG, Z.; WANG, L.; DU, P.; LI, X. Determination of welding stress and distortion in discontinuous welding by means of numerical simulation and comparison with experimental measurements. **Computational Materials Science**, [s.l], v. 49, n. 3, p. 535–543, 2010. Disponível em: https://www.sciencedirect.com/science/article/pii/S0927025610003186. Acesso em: 1 out. 2025.

(6) MACKERLE, J. Finite element analysis and simulation of welding: a bibliography (1976–1996). **Modelling and Simulation in Materials Science and Engineering**, [s.l], v. 4, p. 501–533, 1996. DOI: https://doi.org/10.1088/0965-0393/4/5/006. Disponível em: https://doi.org/10.1088/0965-0393/4/5/006. Acesso em: 02 out. 2025.

(7) MALISKA, Clovis R. **Transferência de calor e mecânica dos fluidos computacional**. 2. ed. Rio de Janeiro: LTC — Editora S.A., 2004. 453 p.

(8) PATANKAR, Suhas V. **Numerical heat transfer and fluid flow**. New York: McGraw, 1980. 197 p.

(9) SCHNEIDER, G. E.; ZEDAN, M. Control-volume-based finite element formulation of the heat conduction equation. *In*: **SPACECRAFT Thermal Control, Design, and Operation**. AIAA, v. 86, p. 305–327, 1983.

(10) BALIGA, B. R.; PATANKAR, S. V. A control volume finite-element method for two-dimensional fluid flow and heat transfer. **Numerical Heat Transfer**, [s.l], v. 6, p.

245–261, 1983. DOI: https://doi.org/10.1080/01495728308963086. Disponível em: https://doi.org/10.1080/01495728308963086. Acesso em: 1 out. 2025.

(11) CEBULA, A.; TALER, J.; OCŁOŃ, P. Heat flux and temperature determination in a cylindrical element with the use of finite volume finite element method. **International Journal of Thermal Sciences**, [s.l], v. 127, p. 142–157, 2018. Disponível em: https://www.sciencedirect.com/science/article/pii/S1290072917313881. Acesso em: 1 out. 2025.

(12) SINGH, G.; SAXENA, R. K.; PANDEY, S. An examination of mechanical properties of dissimilar AISI 304 stainless steel and copper weldment obtained using GTAW. **Materials Today: Proceedings**, [s.l], v. 26, p. 2783–2789, 2020. Disponível em: https://www.sciencedirect.com/science/article/pii/S2214785320313341. Acesso em: 1 out. 2025.

(13) SATHISHKUMAR, D.; DAS, A. D. Investigations on effect of process parameters on GTAW of aluminium alloy welding using full factorial design technique. **Materials Today**: Proceedings, [s.l], v. 37, n. 2, p. 621-626, 2021. Disponível em: https://www.sciencedirect.com/science/article/pii/S2214785320342279. Acesso em: 1 out. 2025.

(14) MING, H.; WANG, J.; HAN, E. Comparative study of microstructure and properties of low-alloy-steel/ nickel-based-alloy interfaces in dissimilar metal weld joints prepared by different GTAW methods. **Materials Characterization**, [s.l], v. 139, p. 186–196, 2018. Disponível em: https://www.sciencedirect.com/science/article/pii/S1044580317328875. Acesso em: 1 out. 2025.

(15) XU, Y. L. et al. Marangoni convection and weld shape variation in A-TIG welding process. **Theoretical and Applied Fracture Mechanics**, [s.l], v. 48, n. 2, p. 178–186, 2007. Disponível em: https://www.sciencedirect.com/science/article/pii/S0167844207000407. Acesso em: 1 out. 2025.

(16) PATRO, R.; PRADHAN, S. K. Finite element simulation and optimization of orbital welding process parameters. **Materials Today**: Proceedings, [s.l], v. 5, n. 5, p.12886-12900, 2018. Disponível em: https://www.sciencedirect.com/science/article/pii/S2214785318304772. Acesso em: 1 out. 2025.

(17) YEGAIE, Y. S.; KERMANPUR, A.; SHAMANIAN, M. Numerical simulation and experimental investigation of temperature and residual stresses in GTAW with a heat sink process of Monel 400 plates. **Journal of Materials Processing Technology**, [s.l], v. 210, p. 1690–1701, 2010. Disponível em: https://www.sciencedirect.com/science/article/pii/S0924013610001597. Acesso em: 1 out. 2025.

(18) MASUBUCHI, K. **Analysis of welded structures**: residual stresses, distortion and their consequences. Oxford: Pergamon Press, 1980.

(19) DENG, H.; MURAKAWA, H. Prediction of welding distortion and residual stress in a thin plate butt-welded joint. **Computational Materials Science**, [s.l], v. 43, n. 2, p. 353–365,

2008. Disponível em: https://www.sciencedirect.com/science/article/pii/S0927025607003345. Acesso em: 1 out. 2025.

(20) WANG, H. X.; WEI, Y. H.; YANG, C. L. Numerical calculation of variable polarity keyhole plasma arc welding process for aluminum alloys based on finite difference method. **Computational Materials Science**, [s.l], v. 40, p. 213–225, 2007. Disponível em: https://www.sciencedirect.com/science/article/pii/S0927025606003429. Acesso em: 1 out. 2025.

(21) GOKHALE, N. P.; KALA, P. Thermal analysis of TIG-WAAM based metal deposition process using finite element method. **Materials Today: Proceedings**, [s.l], v. 44, p. 453–459, 2021. Disponível em: https://www.sciencedirect.com/science/article/pii/S2214785320375088. Acesso em: 1 out. 2025.

(22) TAYLOR, G. A.; HUGHES, M.; STRUSEVICH, N.; PERICLEOUS, K. Finite volume methods applied to the computational modelling of welding phenomena. **Applied Mathematical Modelling**, [s.l], v. 26, p. 309–320, 2002. Disponível em: https://www.sciencedirect.com/science/article/pii/S0307904X01000634. Acesso em: 1 out. 2025.

(23) PHAM, X.-T.; CHAMPAGNE, O. Numerical simulation of moving heat source in arc welding using the element-free Galerkin method with experimental validation and numerical study. **International Journal of Heat and Mass Transfer**, [s.l], v. 154, 2020. Disponível em: https://www.sciencedirect.com/science/article/pii/S001793101936555X. Acesso em: 1 out. 2025.

(24) ALMEIDA, D. F. F. **Determinação das tensões residuais e deformações resultantes do processo de soldadura TIG através do Método dos Elementos Finitos.** 2012. 128 f. Dissertação (Mestrado em Engenharia Mecânica) – Faculdade de Ciências e Tecnologia, Universidade Nova de Lisboa, Lisboa, 2012.

(25) YAGHI, D. A.; BECKER, A. **State of the art review:** weld simulation using finite element methods. Nottingham: University of Nottingham, 2004.

(26) LACOBAESCU, G. A theoretical model for welding process with Gaussian heat source — part 1. **U.P.B.** Series D, [s.l], v. 68, p. 45–50, 2006.

(27) CARVALHO, M. J. et al. **Orientações práticas de soldagem em aço inox.** Timóteo: Acesita S.A., 1999.

(28) BRACARENSE, A. Q. **Processo de soldagem TIG – GTAW.** Belo Horizonte: Universidade Federal de Minas Gerais, 2000. p. 1–22.

(29) KOU, S. **Welding metallurgy**. 2. ed. New York: Wiley, 2002.

(30) LYTTLE, K. A. **Welding, Brazing, and Soldering**. Materials Park, OH: ASM International, 1993. p. 64.

(31) **WELDING handbook.** v. 1. 7. ed. Miami: American Welding Society, 1976. p. 2–32.

(32) ROSENTHAL, D. The theory of moving source of heat and its application to metal transfer. **ASME Transactions**, [s.l], v. 43, p. 849–866, 1946.

(33) BLONDEAU, R. **Metallurgy and mechanics of welding:** processes and industrial applications. London: ISTE, 2008.

(34) ROSENTHAL, D.; SCHMERBER, R. Thermal study of arc welding: experimental verification of theoretical formulas. **Welding Journal**, [s.l], v. 17, p. 2s–8s, 1938.

(35) ADAMS, C. M. Jr. Cooling Rates and Peak Temperatures in Fusion Welding. **Welding Journal**, [s.l], v. 37, n. 5, p. 210s, 1958.

(36) MACHADO, I. G. **Condução do calor na soldagem**: fundamentos e aplicações. Porto Alegre: Imprensa Livre, 2000.

(37) CUI, M. et al. Numerical solution of phase heat transfer problems by effective heat capacity model and element differential method. **Journal of Computational Science**, [s.l], v. 60, 101593, 2022. DOI:10.1016/j.jocs.2022.101593. Disponível em: https://www.sciencedirect.com/science/article/pii/S187775032200028X. Acesso em: 16 out 2025.

(38) PESSOA, D. B. et al. Element-based finite volume method applied to autogenous bead-on-plate GTAW process using the enthalpy energy equation. **International Journal of Thermal Sciences**, [s.l], v. 204, 2024. DOI: https://doi.org/10.1016/j.ijthermalsci.2024.109245. Disponível em: https://www.sciencedirect.com/science/article/pii/S1290072924003673. Acesso em: 16 out 2025.

(39) PIMENTA, P. V. D. C. L. **Simulation of the thermal-mechanical continuous casting process using unstructured grids.** 2019. Dissertação (Mestrado em Engenharia e Ciência dos Materiais) – Universidade Federal do Ceará, Fortaleza, 2019.

(40) WANG, X.; LUO, Y.; FAN, D. Investigation of heat transfer and fluid flow in high current GTA welding by a unified model. **International Journal of Thermal Sciences**, [s.l], v. 142, p. 20–29, 2019. Disponível em: https://www.sciencedirect.com/science/article/pii/S1290072918315114. Acesso em: 1 out. 2025.

(41) SHANMUGAM, N. S.; BUVANASHEKARAN, G.; SANKARANARAYANASAMY, K.; KUMAR, R. S. A transient finite element simulation of the temperature and bead profiles of T-joint laser welds. **Materials & Design**, [s.l], v. 31, p. 4528–4542, 2010. Disponível em: https://www.sciencedirect.com/science/article/pii/S0261306910002116. Acesso: 1 out 2025.

(42) GOLDAK, J.; CHAKRAVARTI, A.; BIBBY, M. A New Finite-Element Model for Welding Heat-Sources. **Metallurgical Transactions B**, [s.l], v. 15, n. 2, p. 299-305, 1984. Disponível em: https://link.springer.com/article/10.1007/BF02667333. Acesso: 1 de out 2025.

(43) XIAOXIN, et. al. Cover plate welding sequence and shape rationality simulation analysis on wall cracks of stainless steel spent fuel pool. **Progress in Nuclear Energy**, [s.l], v. 154,

2022. DOI: https://doi.org/10.1016/j.pnucene.2022.104481. Disponível em: https://www.sciencedirect.com/science/article/pii/S0149197022003559. Acesso: 1 de out 2025.

(44) BAG, S.; KUMAR, B.; NIRSANAMETLA, Y.; MONDAL, A. K.; BISWAS, P. Development of avocado shape heat source model for finite element based heat transfer analysis of high-velocity arc welding process. **International Journal of Thermal Sciences**, [s.l], v. 166, 2021. DOI: https://doi.org/10.1016/j.ijthermalsci.2021.107005. Disponível em: https://www.sciencedirect.com/science/article/pii/S1290072921001708. Acesso: 1 de out 2025.

(45) HERNÁNDEZ, M.; AMBRIZ, R. R.; CORTÉS, R.; GÓMORA, C. M.; PLASCENCIA, G.; JARAMILLO, D. Assessment of gas tungsten arc welding thermal cycles on Inconel 718 alloy. **Transactions of Nonferrous Metals Society of China**, [s.l], v. 29, p. 579–587, 2019. Disponível em: https://www.sciencedirect.com/science/article/pii/S1003632619649666. Acesso: 1 de out 2025.

(46) GOLDAK, J. A.; AKHLAGHI, M. **Computational welding mechanics**. Springer, 2005.

(47) PIMENTA, P. V. D. C. L.; MARCONDES, F. Two-dimensional rate-independent plasticity using the element-based finite volume method. **Journal of the Brazilian Society of Mechanical Sciences and Engineering**, [s.l], v. 41, n. 3, p. 142, 2019. Disponível em: https://link.springer.com/article/10.1007/s40430-019-1641-y. Acesso: 1 de out 2025.

(48) FERNANDES, B. R. B. **Implicit and semi-implicit techniques for the compositional petroleum reservoir simulation based on volume balance.** 2014. Dissertação (Mestrado em Engenharia de Petróleo) – Universidade Federal do Ceará, Fortaleza, 2014.

(49) BALIGA, B. R.; PATANKAR, S. V. A new finite-element formulation for convection-diffusion problems. **Numerical Heat Transfer**, [s.l], v. 3, n. 4, p. 393–409, 1980. Disponível em: https://doi.org/10.1080/01495728008961767. Acesso: 1 de out 2025.

(50) SCHNEIDER, G. E.; ZEDAN, M. Control-volume-based finite element formulation of the heat conduction equation. *In*: **SPACECRAFT thermal control, design, and operation.** Progress in Astronautics and Aeronautics, v. 86. Washington: AIAA, 1983. p. 305–327.

(51) MARCONDES, F. et al. A 3D hybrid element-based finite-volume method for heterogeneous and anisotropic compositional reservoir simulation. **Journal of Petroleum Science and Engineering**, [s.l], v. 108, p. 342–351, 2013. Disponível em: https://www.sciencedirect.com/science/article/pii/S0920410513001253. Acesso: 1 de out 2025.

(52) LIMA, I.; MOREIRA-NETTO, A.; CAVALCANTE-NETO, J. et al. A high-performance computing applied to composition reservoir simulation using distributed memory and 3D hybrid unstructured grids. **Journal of the Brazilian Society of Mechanical Sciences and Engineering**, [s.l], v. 46, p. 283, 2024. DOI: https://doi.org/10.1016/j.petrol.2013.04.024. Disponível em: https://www.sciencedirect.com/science/article/pii/S0920410513001253. Acesso: 1 de out 2025.

(53) CARMO, D. A.; FARIA, A. R. A 2D finite element with through-the-thickness parabolic temperature distribution for heat transfer simulations including welding. **Finite Elements in Analysis and Design**, [s.l], v. 93, p. 85–95, 2015. Disponível em: https://www.sciencedirect.com/science/article/pii/S0168874X14001851. Acesso: 1 de out 2025.

(54) FARIAS, R. M.; TEIXEIRA, P. R. F.; VILARINHO, L. O. An efficient computational approach for heat source optimization in numerical simulations of arc welding processes. **Journal of Constructional Steel Research**, v. 176, 2021. DOI: https://doi.org/10.1016/j.jcsr.2020.106382. Disponível em: https://www.sciencedirect.com/science/article/pii/S0143974X20309342. Acesso: 1 de out 2025.

(55) ZHOU, J. et al. Numerical study of heat and mass transfer in dissimilar laser welding of Mg/Al lap-joint with Ti interlayer. **International Journal of Thermal Sciences**, v. 199, 2024. DOI: https://doi.org/10.1016/j.ijthermalsci.2024.108932. Disponível em: https://www.sciencedirect.com/science/article/pii/S1290072924000541. Acesso: 1 de out 2025.

(56) SMITH, M.; SMITH, A. Net bead-on-plate round robin: comparison of transient thermal predictions and measurements. **International Journal of Pressure Vessels and Piping**, [s.l], v. 86, n. 1, p. 96–109, 2009. Disponível em: https://www.sciencedirect.com/science/article/pii/S0308016108001671. Acesso: 1 de out 2025.

(57) MOLLICONE, P. et al. Simple thermo-elastic-plastic models for welding distortion simulation. **Journal of Materials Processing Technology**, [s.l], v. 176, n.1, p. 77-86, 2006. Disponível em: https://www.sciencedirect.com/science/article/pii/S0924013606001968. Acesso: 1 de out 2025.

(58) CHAO, Y. J.; QI, X. Three-dimensional modeling of gas metal arc welding process. *In*: **TRANSACTIONS of North America Manufacturing Research Institute of the Society of Manufacturing Engineers**, [s.l], v. 27, 1999. p. 117–122.

(59) CHAO, Y. J.; ZHU, X. K.; QI, X. WELDSIM: a welding simulation code for the determination of transient and residual temperature, stress and distortion**.** *In:* ATLURI, S. N.; BRUST, F. W. (org.). **Advances in computational engineering and science.** v. II. Paledale: Tech Science Press, 2000. p. 1206–1211.

(60) DENG, D.; MURAKAWA, H. Numerical simulation of temperature field and residual stress in multi-pass welds in stainless steel pipe and comparison with experimental measurements. **Computational Materials Science**, [s.l], v. 37, p. 269–277, 2006. Disponível em: https://www.sciencedirect.com/science/article/pii/S0927025605002624. Acesso: 1 de out 2025.

(61) GARCÍA-GARCÍA, V. et al. FE thermo-mechanical simulation of welding residual stresses and distortion in Ti-containing TWIP steel through GTAW process. **Journal of Manufacturing Processes**, [s.l], v. 59, p. 801–815, 2020. Disponível em: https://www.sciencedirect.com/science/article/pii/S1526612520306319. Acesso: 1 de out 2025.

(62) DAS BANIK, S. et al. Distortion and residual stresses in thick plate weld joint of austenitic stainless steel: Experiments and analysis. **Journal of Materials Processing Tech**, [s.l], v. 289, 2021. DOI: 10.1016/j.jcsr.2021.106809. Disponível em: https://www.sciencedirect.com/science/article/pii/S0924013620303617. Acesso: 2 de out 2025.

(63) KOU, S.; WANG, Y. H. Computer simulation of convection in moving arc weld pools. **Metallurgical transactions A**, [s.l], v. 17, n. 12, p. 2271–2277, 1986. Disponível em: https://link.springer.com/article/10.1007/BF02645925. Acesso: 2 de out 2025.

(64) NASIRI, M. B. et al. Investigation on the influence of various welding parameters on the arc thermal efficiency of the GTAW process by calorimetric method. **Journal of Mechanical Science and Technology**, [s.l], v. 28, n. 8, p. 3255–3261, 2014. Disponível em: https://link.springer.com/article/10.1007/s12206-014-0736-8. Acesso: 2 de out 2025.

(65) HURTIG, K. et al. A critical analysis of weld heat input measurement through a water-cooled stationary anode calorimeter**. Sage Journal**, [s.l], v. 1718, n.18, p. 1–19, 2015. Disponível em: https://journals.sagepub.com/doi/full/10.1080/13621718.2015.1112945. Acesso: 2 de out 2025.

(66) MACHADO, I. G. **Soldagem e técnicas conexas**: processos. Porto Alegre: [s.n], 1996. 477 p.